Observing the Truth

Recording Earth's Changing Flow of Energy

by

Hamish Daniel Prince

A dissertation submitted in partial fulfillment
of the requirements for the degree of
Doctor of Philosophy
Atmospheric and Oceanic Sciences

at the
University of Wisconsin-Madison
2025

Date of Final Oral Exam: 29th April 2025
The dissertation is approved by the following members of the PhD Committee at the University of Wisconsin-Madison:
Tristan L'Ecuyer, Professor, Atmospheric and Oceanic Sciences
Elizabeth Maroon, Assistant Professor, Atmospheric and Oceanic Sciences
Jonathan Martin, Professor, Atmospheric and Oceanic Sciences
Steve Vavrus, Scientist, Center for Climatic Research
Daniel Vimont, Professor, Environmental Studies

Observing the Truth

Recording Earth's Changing Flow of Energy

Hamish Daniel Prince

Abstract

The receipt of energy within our atmosphere is the fundamental driver of the climate system. Our ability to accurately measure this exchange of energy and establish a reliable understanding of its trend and variability is fundamental to comprehending the current state of Earth's climate. This dissertation presents three novel assessments of Earth energy budget observations: trends in the polar top-of-atmosphere solar absorption and thermal emission, constraining atmospheric energy transport from observations, and examining the covariability of energy flux components and meridional energy transport.

Satellite observations reveal that decreasing surface albedo in both polar regions is increasing the absorption of solar radiation, but the disposition of this absorbed energy is fundamentally different. In the Arctic, the rates of increasing absorbed solar radiation and thermal emission are remarkably similar (0.98 and 0.94 $\mathrm{Wm^{-2}\ dec^{-1}}$ respectively), with solar absorption variability explaining two thirds of the annual thermal emission variability. Conversely, Antarctic thermal emission is not responding to the increasing (though not yet statistically significant) solar absorption of $0.59 \pm 0.64\ \mathrm{Wm^{-2}\ dec^{-1}}$ with less than a third of the annual thermal emission variability explained by accumulated solar absorption. The Arctic is undergoing rapid adjustment to increasing solar absorption resulting in no change to the net energy deficit, while increasing Antarctic solar absorption represents additional energy input into the Earth system being taken up by the Southern Ocean.

To close the atmospheric energy budget, the meridional transport of energy must be recorded, representing the net energy moved by winds across a latitude circle. Here, a method for calculating energy transport from observed energy fluxes is presented, calculated as the integral (accumulation) of the net energy input into the atmosphere from one pole to the other. Observations tend to underestimate annual mean energy transport compared to reanalysis, attributed to reduced poleward gradients in the observed surface turbulent heat fluxes. There is however, close agreement in the variance with correlations of up to 0.8 and 0.5 in the midlatitudes and tropics respectively between calculations. The observed energetic framework presented here facilitates a novel assessment of the energetic fluxes consistent with energy transport variability.

Variability in the meridional heat transport is associated with net energy gains and losses within approximately $\pm 15°$ either side a latitude band. Anomalous gradients of atmospheric latent heating is the most important term for describing the variability of midlatitude heat transport. Enhanced evaporation within the tropics provides an excess of energy which is then transported poleward and lost through all energy fluxes, radiation, turbulent fluxes, and the atmospheric tendency. The atmospheric tendency (the storage of energy in the atmosphere) is the most important component for heat transport into the polar regions through the convergence of energy transport which is not immediately lost from the atmosphere. These results provide a benchmark for assessing variability in the climate system with the use of observations.

Acknowledgements

I would like to express my deepest gratitude to all those who have supported me throughout my doctoral studies and completion of this thesis. First and foremost my supervisor, Professor Tristan L'Ecuyer, for his expertise, guidance, and advice throughout my studies. I appreciate the trust and motivation Tristan provided as I explored my own personal research interests, along with the expansive curiosity explored in meetings. I am thankful for the many unique opportunities I have had during my PhD, including our adventure down to New Zealand. As I move into a new chapter of my career, I will always be grateful for the guidance I have received and I look forward to ongoing collaborations.

To Dr Aaron Donohoe (University of Washington), for ongoing enthusiastic collaborations, I am deeply thankful. I appreciate our intellectual discussion and your keenness to explore similar research topics together. I am thankful to my entire committee for their individual contributions to my progress in my PhD: Liz, Dan, Jon, and Steve. Not only did I appreciate your breadth of knowledge, but being exposed to your individual approaches to science was enlightening. The entire AOS department, Faculty and Staff, were instrumental in the completion of my PhD, whether in formal classes, casual conversation, or maintaining my visa status. I am deeply thankful to these mentors, teachers, and my wider support network.

To my fellow students and friends here in Madison, thank you for the wonderful community I have had a pleasure to be a part of. You all have created an environment that is supportive and caring while also being a lot of fun - from weekend adventures to board game nights, it has been excellent. I am also thankful to the wider PREFIRE Science team for their encouragement and enlightening discussions.

Lastly, I want to thank my parents and family for their ongoing support as I have been completing my studies far away from home. I value their ongoing trust and encouragement as I pursue adventures further afield.

My studies were supported by funding from Fulbright New Zealand, whose assistance I deeply appreciate.

Contents

List of Figures

List of Tables

Chapter 1

Introduction

The historical record of our atmosphere is an invaluable resource for understanding the climate system. Theory, equations, and models can take us so far, but without observations to reveal, validate, and train our analytics, meteorology and climatology remains an inexact science (Bjerknes, 1914). Transformative shifts in our ability to observe the atmosphere have occurred over the last century, with the most recent paradigm shift entering into the realm of space-based remote sensing (Johnson, 1962). The records available to us today are dependent on the tenacity and vision of not just the scientists and engineers who developed and established recording instruments, but also the continual funding and frameworks that allow for ongoing data collection. However, all data collection comes with uncertainty and we must therefore take great care evaluating our historical records. What we know to be true about our planet not only relies on the collection of observations, but our ability to trust the data.

This dissertation presents three novel assessments of the historical record of Earth's climate system from its most fundamental property - the flow and exchange of energy. All motion in Earth's atmosphere arises through the receipt of solar radiation on our rotating planet, driving energy transport through our diffusive atmosphere from regions of excess energy to regions of energy deficit (Budyko, 1969; Oort, 1971; North et al., 1981). To close Earth's energy budget, following the receipt and redistribution of solar energy, Earth re-emits this energy out to space as outgoing longwave radiation (OLR). On long time scales, absorbed solar radiation (ASR) and OLR balance globally, satisfying the conservation of energy. However, the poleward gradients of these properties are not equal, due to the imperfect diffusivity of Earth's atmosphere, leading to instability (North et al., 1981). All phenomena that occur within our climate system are underpinned by this fundamental energy receipt and poleward gradient of energy.

Directly observing the receipt and emission of Earth's energy requires a spaceborne perspective and indeed, the first meteorological satellites in orbit in the 1950's were measuring the incoming and outgoing radiative energy of the planet (Soumi, 1961; Raschke and Bandeen, 1970). Systematic observations of the global top-of-atmosphere (TOA) radiation budget began in the 1980's through the NASA Earth Radiation Budget Experiment (ERBE; Backstrom 1984). Modern, continuous measurement of Earth radiation budget began in March 2000 with the NASA Clouds and Earth's Radiant Energy System (CERES; Loeb et al. 2018), providing authoritative measurements of Earth's TOA and surface radiative fluxes which are consistent with observations of global ocean heat uptake. While the absolute accuracy of measured TOA radiation from the CERES instrument is within 5 Wm^{-2}, the instruments have very high calibration stability (<0.3 Wm^{-2} dec^{-1}), providing considerable confidence in the temporal evolution of these TOA records (Loeb et al., 2009). This record of TOA radiation may be regarded as the most trustworthy record of the global climate system as a whole, directly measuring almost the entire globes radiative exchange. If changes in our climate system are to be directly observed, than this record of TOA energetic exchange is certainly an appropriate candidate.

Considering that the TOA radiative exchange is one of the most precise measurements of the global climate system, it is worth examining how this record (spanning multiple decades) may be changing in the context of ongoing anthropogenic climate change. The polar regions in particular are undergoing the most dramatic changes, with increases in surface temperature exceeding three times that of the global mean (Eyring et al., 2021). Paired with dramatic changes to the surface cover through reducing sea ice (Stroeve et al., 2012; Parkinson, 2019), these changes to the polar regions are certainly expected to be changing the underlying radiative budget of the Earth system. This hypothesis underpins the first research questions addressed in this dissertation:

1. How are the polar, top-of-atmosphere radiative budgets changing in the observed satellite record?

This TOA perspective however, does not allow for closure of the atmospheric energy budget which also requires measurements of energy flux between the atmosphere and surface. Processes such as the evaporation of water and the thermal emission of the atmosphere towards the surface represent just two of the many exchanges of energy that must be considered if we are to comprehend the exchange of energy between the atmosphere and Earth's surface (the surface energy balance). Historically, the observed record of the surface energy budget has not been trusted by the scientific community (Trenberth, 1997). Without trusted observations of the surface energy exchange we are unable to observe the atmospheric energy budget, and therefore the most fundamental forcing of our atmosphere (the flow of energy) remains unobserved. Over recent decades however, new observing systems have been established that dramatically broaden our observed record. It is worth exploring whether the state-of-the-art observing systems currently operating are in fact able to accurately measure the atmospheric energy budget. This goal forms the basis of the second research question:

2. Can the global atmospheric heat transport be constrained with observations of Earth's energy budget?

Examining the climate system from the atmospheric heat transport offers a unique perspective, allowing for a holistic view of the properties that defines climate variability. Through the second research question, the agreement in the monthly heat transport record is assessed. However, the variability of monthly heat transport from an energetic perspective remains largely unexamined, especially through the use of observations. The third research question of this dissertation will assess how the energetic components, as discussed in the first two research questions, combine to modulate the monthly record of poleward atmospheric heat transport:

3. What is the energetic expression of monthly atmospheric heat transport variability?

Underpinning the analysis in this dissertation is the theme of trustworthiness and questioning what we know to be true. All data has uncertainty and limitations and this is especially true within atmospheric science. Satellite retrieved properties, for example, must go through some form of data transformation to turn retrieved signals into measurements of tangible properties. Biases and errors persist in all satellite observations and must therefore not be considered a record of the true state of the climate. Furthermore, due to the limited number of observing systems, there is extensive overlap in the use of observations across data records, reducing their independence. If an erroneous observation is ingested into the wider suite of global records, then the quality of all records are diminished. Our ability to reveal truths about our planet, to accurately record how we are changing the climate system and understand its resultant impact relies entirely on our ability to make accurate, trustworthy observations.

Chapter 2

Observed Energetic Adjustment of the Arctic and Antarctic in a Warming World

2.1 Introduction

Continual global warming through anthropogenic greenhouse gas emission has increased mean global air temperatures by over 1°C since pre-industrial records. Through a series of geophysical feedbacks the Arctic has warmed by over 3°C (Eyring et al., 2021; Taylor et al., 2022). Observations over the satellite era reveal ongoing fundamental changes in both polar regions in response to warming, including decreasing snow and ice cover, reducing ice mass, rising atmospheric temperatures, and warming oceans (Serreze and Barry, 2011; Stroeve et al., 2012; Armour et al., 2016; Parkinson, 2019). These broad changes modulate the radiative properties of the polar regions, varying how much radiation is absorbed and emitted, through reducing albedo and increasing thermal emission (Wu

This chapter is an edited version of the peer-reviewed publication:
Prince, H. D. and L'Ecuyer, T. S. (2024). Observed Energetic Adjustment of the Arctic and Antarctic in a Warming World. Journal of Climate, 37(8), 2611-2627.

et al., 2020; Duncan et al., 2020). The net radiative deficit in the polar regions is not only important for local phenomena, but serve as an important control on the exchange of energy between the planet and space, driving the energy flows from lower latitudes that govern many aspects of the Earth system (Sévellec et al., 2017; Huguenin et al., 2022; Merlis et al., 2022). Accurately quantifying how the polar radiative fluxes are changing is crucial to developing an understanding of how the earth system adjusts to ongoing warming.

The top of atmosphere (TOA) energy balance is comprised of two fluxes of energy, incoming/outgoing shortwave radiation from the sun and emitted longwave thermal radiation from the surface and atmosphere. In the polar regions the thermal radiation emitted to space is up to 3 times greater than radiation received from the sun with the energy deficit being transported from lower latitudes primarily through large scale atmospheric circulation (L'Ecuyer et al., 2015). A large partition of the incoming solar radiation in the poles is reflected back to space due to both the high albedo of the extensive snow/ice cover along with the ubiquitous cloud cover which accounts for up to 80% of the total Arctic TOA albedo (Sledd and L'Ecuyer, 2019). Variability and trends in snow, ice, and cloud cover will consequently modulate polar solar absorption. Due to the axial tilt of the Earth, the solar input is confined to summertime in the Polar regions, which is characterized by continuous but highly oblique incident solar radiation (Figure 2.1). Conversely, the polar regions emit thermal radiation throughout the entire year, maximizing late in summer as the regions reach their maximum temperature (Figure 2.1). Polar TOA outgoing thermal radiation variability may have multiple sources such as the surface temperature, the temperature of various levels in the atmosphere, cloud type, and the presence of water vapor (L'Ecuyer et al., 2021). It is the covarying effects of changes in surface ice cover, temperature, cloud cover, and water vapor that ultimately define the impacts of warming on the exchange of radiative energy within the polar regions.

The rapid warming in the Arctic, at least twice as fast as the global average, is occuring through a collection of processes known as Arctic Amplification (Taylor et al., 2022). Increasing global temperatures, driven by anthropogenic greenhouse gas emissions, initiates a number of feedbacks that amplify the warming in the Arctic through changing surface characteristics, lapse rates, cloud feedbacks, and heat and moisture transports (Taylor et al., 2022). These effects result in warmer Arctic air temperatures (Lenssen et al., 2019), reduced sea ice concentration (Stroeve and Notz, 2018), reduced sea ice age (Maslanik et al., 2011), longer melt seasons (Markus et al., 2009), and changes in surface-atmosphere interactions (Serreze and Barry, 2011) paired with a wide variety of ecological, societal, and economic impacts (Smith and Stephenson, 2012; Stephen, 2018; Myers-Smith et al., 2020). Perhaps the most fundamental impact of Arctic Amplification on the climate system is the changes to Earth's TOA radiative balance. Indeed, quantifying the cascade of changes to the Arctic, including the changing Arctic energy balance, is a priority research goal identified by the Interagency Arctic Research Policy Committee (IARPC) 2022-2026 Arctic Research Plan (IARPC, 2021).

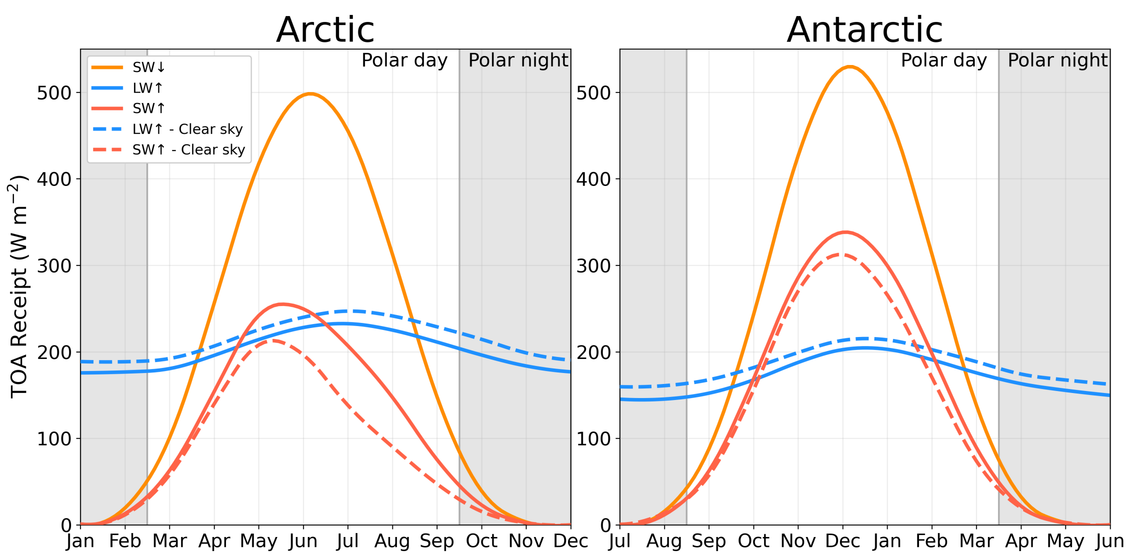

Figure 2.1: Mean TOA radiative fluxes of incoming and outgoing shortwave radiation (SW↓ and SW↑) and outgoing longwave radiation (LW↑) as measured by CERES-EBAF averaged within the Arctic (left) and Antarctic (right) circles (66.58°N/S). All-sky means are shown with solid lines and clear-sky means are shown with dashed lines. Polar night (winter), when the sun is continuously below the horizon is highlighted with the gray shading

The observed Antarctic responses to a warming world are not nearly as explicit as the broad, statistically significant warming trends and sea ice decline observed in the Arctic. The contrasting geography (Salzmann, 2017) accompanied by Southern Ocean heat uptake (Armour et al., 2016) and the radiative effects of South Pole stratospheric ozone depletion (Thompson et al., 2011) have led to a much weaker transient warming in Antarctica in the current observation period. In the satellite record, Antarctic sea ice appeared to be unchanging until 2015 (Meredith et al., 2019), but this has been followed by unprecedented declines in sea ice area in 2016 through to 2019 (and continuing through into 2023; NSIDC 2023), leading to an overall decline in sea ice area over the satellite record (Parkinson, 2019). The recent loss of Antarctic sea ice is expected to have an impact on the Antarctic albedo and subsequently the absorption of solar radiation. If absorbed solar radiation is increasing then similar questions can be asked regarding the disposition of this energy as in the Arctic. Amplification of warming is certainly expected in Antarctica (Smith et al., 2019), especially through increased moisture transport and lapse-rate feedbacks (Hahn et al., 2021). The ice-albedo feedback is shown through modelling experiments to be of secondary importance (Hahn et al., 2021), however, the exact nature of this feedback and impact on the net Antarctica energy balance remains unexamined in the observation record.

The continual, multi-decadal record from the NASA Clouds and Earth's Radiant Energy System (CERES) instruments offers an invaluable and unique documentation of Earth's TOA radiative balance (Loeb et al., 2018). The CERES record is beginning to observe fundamental changes to the Earth system (Stephens et al., 2022). In the Arctic, CERES observations have been used to identify the increasing solar absorption (decreasing reflection) at a rate of 1.3 ± 0.6 Wm^{-2} dec^{-1} (between 2000 and 2017; Duncan et al. 2020) along with the spatial pattern of absorption trends, maximizing over regions of extensive sea ice loss (Sledd and L'Ecuyer, 2021). Using a combination of CERES and satellite microwave products, Pistone et al. (2014) estimate that between 1979 and 2011 the solar flux into the Arctic had increased by 6.4 ± 0.9 Wm^{-2} corresponding to a rate of between

1.7 and 2.3 Wm^{-2} dec^{-1}. Duncan et al. (2020) also briefly note that CERES indicates increasing thermal emission in the Arctic (north of 60°N) at a rate of 1.1$\pm$0.4 Wm^{-2} dec^{-1}, comparable to the recorded trends in solar absorption. Peterson et al. (2019) examine the spectral dimension of these changes through analysis of the Atmospheric Infrared Sounder (AIRS, onboard NASA AQUA) demonstrating that Arctic trends in thermal emission are primarily driven by changes in surface temperature, rather than changes in water vapor or atmospheric properties. If changes in thermal emission are primarily driven by change in surface temperature, then variable solar absorption would be expected to directly influence thermal emission if it warms the surface. The compensation between the TOA solar and thermal fluxes, the net radiative balance, is gradually increasing globally through greenhouse gas concentrations with considerable regional variability due to changes in cloud cover and surface snow/ice (Trenberth and Fasullo, 2012; Loeb et al., 2021). The spatial nature of changes in polar thermal emission and its relation to changing albedo and solar absorption are both important outstanding questions that naturally follow from these prior studies.

Here, satellite observations of the TOA energy balance in both the Arctic and Antarctic are examined from the CERES record (2000-2021), addressing shortwave and longwave fluxes along with the net energy deficit in the context of variable and reducing ice cover. Arctic solar absorption has received considerable attention as a changing aspect of the Earth system but to what extent the thermal emission offsets this trend requires further examination. Furthermore, with recent losses in sea ice cover in Antarctica, the solar absorption is expected to be responding accordingly in the region. Thermal emission in Antarctica has been offered little examination and remains as an important phenomenon to quantify to account for all radiative energy pathways in the polar regions. If the thermal emission does not offset the increasing solar absorption, then the polar energy deficit reduces, which will represent changing pathways of energy within the Earth system. Clouds are also known to considerably modulate Arctic solar absorption trends and their role in both solar absorption and thermal emission at both poles will also be quantified herein. Given the short 21-year record, observed variability may not be representative of long-term trends and reported trends will be influenced by both internal variability (from annual to decadal scales) and anthropogenic forcing (Raghuraman et al., 2021; Loeb et al., 2022). The aim of this research is not to report on the exact nature of these trends but to compare the differing response in the radiative exchange at both poles, the importance of surface ice cover, and the role of clouds in modulating this exchange.

2.2 Methods

Observations of the polar TOA energy balance are retrieved from the Clouds and Earth's Radiant Energy System Energy Balance and Filled (CERES-EBAF) version 4.2 (retrieved January 2024) derived primarily from the CERES instrument onboard the NASA Terra, Aqua, and NOAA20 satellites (Loeb et al., 2018). The CERES record, starting in 2000 and providing monthly averages at $1^{\circ}\times1^{\circ}$ resolution, is the authoritative measurement of Earth's TOA balance. The Energy Balance and Filled (EBAF) product provides estimates of TOA radiative exchange consistent with global ocean heat uptake from *in situ* measurements (Loeb et al., 2018). While the absolute accuracy of the CERES instrument has TOA errors of up to 5 Wm^{-2} (less than 5% of the signal), the relative calibration stability is better than 0.3 Wm^{-2} dec^{-1}, demonstrating that anomalies in the TOA record are robust and serve as a direct observation of changes in Earth's TOA radiative exchange (Loeb et al., 2009). Furthermore, the CERES-EBAF TOA cloud detection is based on the radiative properties of clouds present (Loeb et al., 2018) which would be expected to capture most of the radiatively important clouds and any clouds that escape this detection would only have a small influence on the reported monthly broadband trends.

To quantify emerging changes in polar radiative balance, TOA all-sky and total-region clear-sky shortwave (SW↑) and longwave (LW↑) fluxes from the CERES-EBAF 4.2 product are analyzed. Total-region clear-sky fluxes are used to maintain consistency between observational and model generated clear-sky fluxes (Loeb et al., 2018). The annual accumulated (Jm^{-2}) absorbed solar radiation (ASR) and outgoing longwave radiation (OLR) for both regions are calculated as the spatially averaged and temporally integrated fluxes. Deseasonalized monthly anomalies (Wm^{-2}) of absorbed solar and thermal emission are multiplied by the number of seconds in each month and integrated across the full region for both the Arctic and Antarctica. To examine how changes in these fluxes combine to influence variability in the polar energy deficits the net energy (ASR minus OLR), a value that is dominantly negative over the polar regions, is also computed. Results are presented in time integrated quantities, with spatial and temporal averaged quantities (e.g. Wm^{-2}) presented in Appendix A and text to aid comparison with other previous studies.

The monthly accumulated energy is then summed over half-yearly and annual timescales to determine year-to-year variability in the ASR to OLR relationship due to their differing relative importance over the polar day (summer) and polar night (winter). The annual (12-month) period considered for the polar energy accumulation begins at the start of summer, when the poles enter the period of continuous incident solar illumination (polar day), corresponding to March and September for the Arctic and Antarctic, respectively. The accumulated ASR and OLR is then summed through to February and August in the following year and assigned the year based on the start of the sum for analysis and interpretation. For the Arctic, the total period considered is March 2000 to February 2021 and in Antarctica, September 2000 to August 2021.

The polar regions in this study are defined as time invariant, contiguous regions centered at both poles where the climatological mean annual 2-m air temperature (from the Atmospheric Infrared Sounder 2002–2016; AIRS 2019) is below 0°C (Figure 2.2). This definition of the polar region is particularly important in the Arctic to remove the warm Atlantic water inflow in the Barents Sea which remains ice-free year-round and has a different thermodynamic behavior than the rest of the Arctic (Mayer et al., 2019; Sledd and L'Ecuyer, 2019). The thermal definition is also important to capture changes in the Antarctic TOA energy exchange due to the vast extent of sea ice that extends equatorward of 66.5°S. Figure 2.2 shows the gridded regions at both poles that meet this definition and their close relation with the mean maximum sea ice extent (in February and August for the Northern and Southern Hemispheres respectively). The presented conclusions are relatively insensitive to the polar region definition as long as the broad extent of variable sea ice cover at both poles is contained within the respective boundaries (Supplementary Figure A.1).

Arctic and Antarctic sea ice data area retrieved from the NOAA/NSIDC Climate Data Record of Passive Microwave Sea Ice Concentration product (version 4; Meier et al. 2021) on the Equal-Area Scalable Earth grid (EASE). Sea ice area (SIA) is calculated from the sea ice concentration (a fraction of area) in each grid cell multiplied by the area of the grid cell. Where the sea ice concentration is less than 15%, the sea ice area for that cell is set to zero due to limitations in the microwave sensitivity at low ice concentrations. Ocean and atmospheric reanalysis (ORAS5 and ERA5 respectively; Zuo et al. 2019; Hersbach et al. 2018) are utilized to provide an initial examination of the consequences of the presented observations. Area averaged ocean heat content and mean sea surface temperature from 2000 to 2021 are retrieved from ORAS5 for the ocean area identified in Figure 2.2. Zonal mean, mass-consistent atmospheric heat (energy) transport (AHT; Mayer et al. 2022a) is retrieved from ERA5 for the same period at 55°N and 55°S to provide an estimate of the AHT into both polar regions over the observation period.

Due to the relatively short 21-year record offered by the CERES-EBAF TOA measurements, assessing the statistical significance and interpretation of trends is enigmatic. An alternative approach is to calculate the time to emergence (TTE) to assess the time required for a trend in a given timeseries to emerge as significant given the observed variance and autocorrelation of the data (Weatherhead et al., 1998). The TTE is calculated following Chepfer et al. (2018) and Sledd and L'Ecuyer (2021) to account for the internal variability present within the record of annual radiation anomalies. To estimate the number of years required for an observed trend to emerge, simulated time series are generated based on the observation statistics. Four hundred synthetic ensemble members of 200 year-long timeseries are generated using the observed trend with added random noise based on the variance and autocorrelation of the TOA radiation records. The statistically

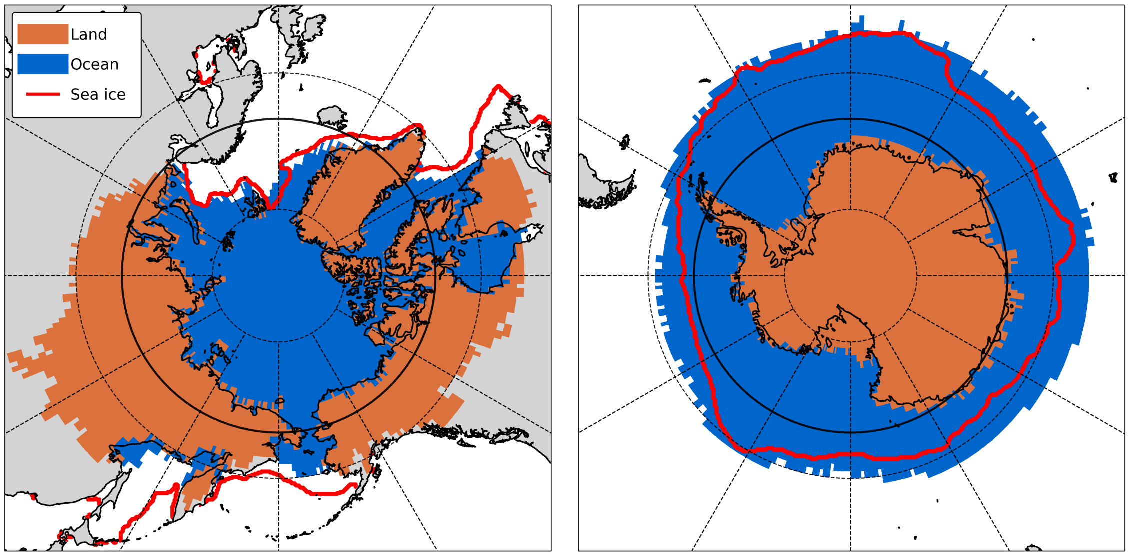

Figure 2.2: Polar regions defined for this study shown as the orange (land) and blue (ocean) gridded mask, where the annual mean 2-m temperature from AIRS (2002-2016) is less than or equal to 0°C (1°×1° grid resolution). The mean sea ice extent during the month of peak extent is shown with the red outline (for August and February for the Northern and Southern Hemispheres respectively). The solid black line of latitude represents the Arctic and Antarctic circles at 66.5°N and 66.5°S respectively.

significant TTE (95% confidence) from each ensemble member is calculated as the amount of time for the magnitude of the trend to be twice that of the scaled standard deviation ($\sigma_{\hat{\omega}}$):

$$\sigma_{\hat{\omega}} = \sigma_N \left[\frac{12dt}{T^3} \frac{(1+\phi)}{(1-\phi)} \right]^{\frac{1}{2}}$$

where σ_N is the standard deviation, T is the length of the time series, dt is the time internal (dt=1 for annual observations) and ϕ is the lag-1 autocorrelation. The TTE reported herein is the mean TTE from the four hundred synthetic timeseries and the standard deviation of the TTE is also reported. Trends with a mean ensemble TTE values less than 21 years are said to have emerged in the observation period. For TTE values greater than 21 years, there has been no trend in the observed record and that the interannual variability is greater than any measured trend. Any trend calculated from 21 years of data is unable to represent the low-frequency variability within the climate system, however, it does represent a snapshot of how the system is currently changing in a warming world. This does not invalidate the observed TTE, however, it may be observed as a lower bound of the true emergence within the forced climate climate system since the signal-to-noise ratio may be overestimated in a truncated timeseries if periodicity exists.

2.3 Results

2.3.1 Arctic energy trends

Annual mean anomalies of ASR, OLR, and net energy relative to the 2000-2020 (full-period) mean in the Arctic and Antarctic are shown in Figure 2.3 for both all-sky and clear-sky conditions (equivalent timeseries at seasonal and monthly intervals are provided in Supplementary Figures A.2 and A.3). All-sky and clear-sky trends in ASR are increasing in the Arctic at rates of $99.6 \pm 70.3 \times 10^3$ PJ yr^{-1} and $205.5 \pm 89.9 \times 10^3$ PJ yr^{-1} respectively, consistent with previously reported trends (Supplementary Table A.1; Sledd and L'Ecuyer 2021). Interestingly, Arctic thermal emission is increasing at a similar rate as solar absorption ($94.7 \pm 56.0 \times 10^3$ PJ yr^{-1}) implying that 95% of the ASR trend is offset by immediate increases in OLR. Since the OLR trend largely offsets the ASR trend, the all-sky net energy deficit of the Arctic has remained approximately constant over the CERES record ($4.8 \pm 48.9 \times 10^3$ PJ yr^{-1}) despite the ongoing rapid ice loss. This invariance in the net Arctic energy imbalance suggests that the energetic impacts of sea ice loss are confined to the Arctic and not transported to lower latitudes. Importantly, these trends are not dependent on the definition of the region, notably remaining consistent for regions bounded by 65°N/S (Supplementary Figure A.1).

The clear-sky trends between ASR and OLR are not comparable, with clear-sky OLR ($127.2 \pm 57.9 \times 10^3$ PJ yr^{-1}) compensating only 62% of the ASR clear-sky trend, driven by disproportionate cloud influences. Clouds reduce the magnitude of the clear-sky ASR trends by 50% and OLR trends by only 25%, demonstrating that the dampening effect of clouds on the decadal trend is more dominant for ASR with only a minor effect on the

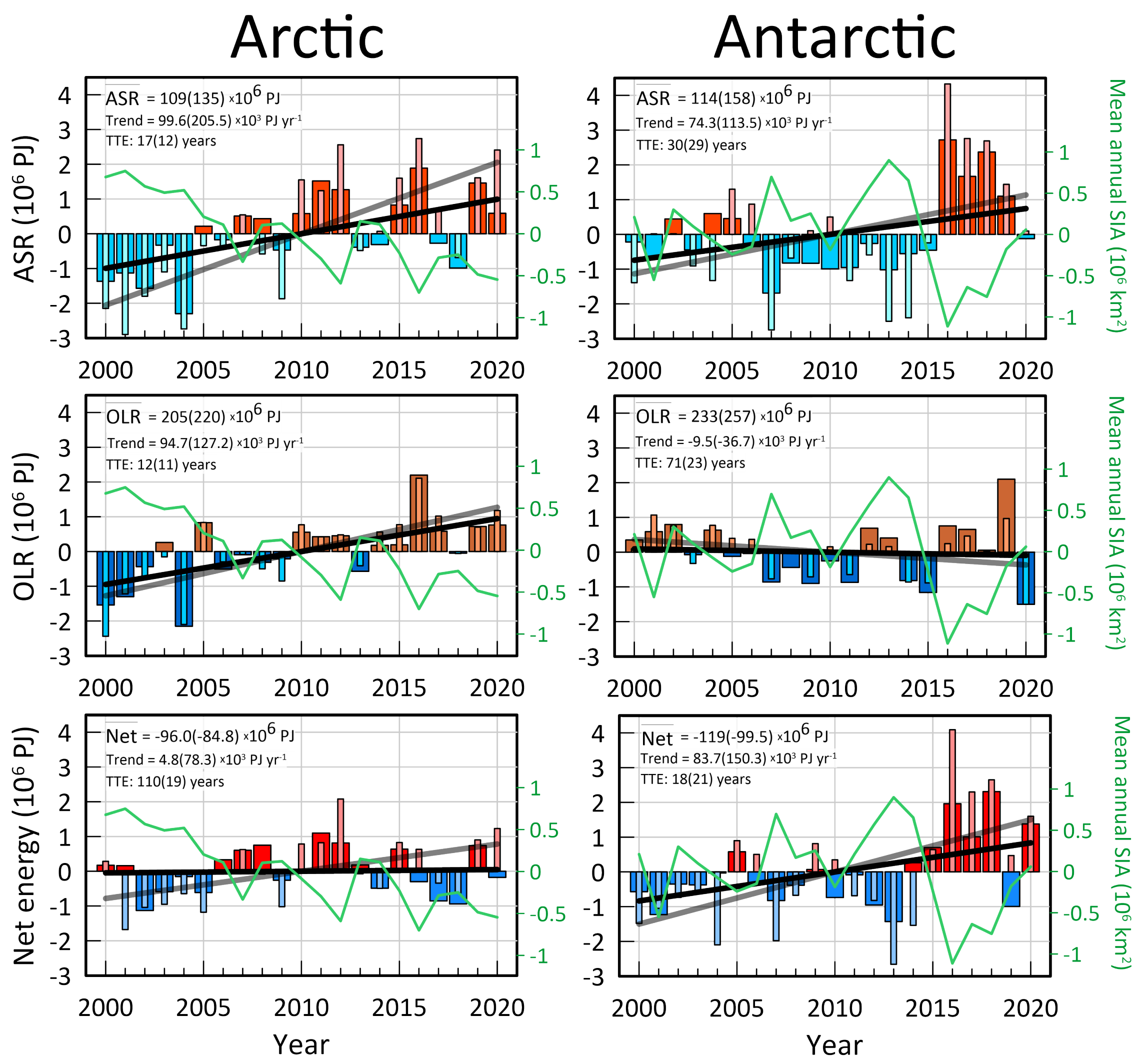

Figure 2.3: Timeseries of the TOA anomalies of absorbed shortwave radiation (ASR), outgoing longwave radiation (OLR) and the net radiative energy (Net) for all-sky (thick bars) and clear-sky (thin bars) conditions. Linear regression shown with the black and gray lines for all- and clear-sky respectively. The annual mean sea-ice area (SIA) is shown with green line on the secondary y-axis. The mean, trend, and time-to-emergence are shown in the upper left (clear-sky in parentheses).

trends of thermal emission. The amplified clear-sky ASR trend (being double the all-sky trend) drives a positive trend in the clear-sky net energy ($78.3 \pm 62.9 \times 10^3$ PJ yr^{-1}) that has emerged within the observation period (TTE of 18±5 years). These results demonstrate that without the influence of clouds, the Arctic energy deficit would have a tendency to become reduced in the absence of more rapid increases in SST, however, the dampening effects of clouds on the ASR trend inhibits Arctic ocean warming.

Our confidence in these findings is reinforced by the fact that Arctic trends in both ASR and OLR have emerged within the 21-year CERES record with TTE of 17±4 and 12±4 years, respectively, demonstrating that changes in the Arctic environment are detectable in observations of the interannual radiative exchange; more solar radiation is being absorbed and more thermal emission is being emitted. It is worth noting that, despite conventional wisdom concerning the effects of sea ice loss on solar reflection, the all-sky ASR trend was by far the last to emerge in the CERES record. Like, all-sky OLR, clear-sky ASR and OLR trends emerged within 12±3 and 11±3 years, respectively. This demonstrates that not only do clouds have a dampening effect on the rate of change in ASR, but clouds also reduce the detectability of the trend of ASR. Since cloud cover and sea ice concentration are not independent (Kay and Gettelman, 2009; Taylor et al., 2015), it is important to note that the slower emergence of all-sky ASR may also be influenced by the interannual variability of sea ice. However, the difference between the clear-sky and all-sky ASR TTE indicates that sea ice variability alone is not increasing the all-sky ASR TTE since it would influence both records.

The statistical relationship between annual ASR and OLR is examined to assess the dependence of emitted thermal radiation to absorbed solar radiation within a given year (Figure 2.4). The interannual variability of all-sky OLR is well explained ($R^2 = 0.67$) by of the variability in all-sky ASR in the Arctic with a slope of 0.69 (being statistically significant at the 95% level). The relationship is stronger for the clear-sky Arctic, with an increased R^2 of 0.76 (slope of 0.55 and statistically significant at 95%), demonstrating that 10% more of the OLR variability is explained by ASR in clear-skies. Since clouds are removed in deriving the clear-sky relationship, it can be suggested that since the slope is not equal to unity, the remaining 35% of the increased ASR received at the surface within a given year is being sequestered into the ocean (or involved in ice-water phase changes) and away from the surface where it will not have an impact on the surface or atmospheric temperatures which contribute to the OLR.

2.3.2 Antarctic energy trends

In Antarctica, neither the ASR or OLR have emerged as detected trends over the CERES-EBAF record (Figure 2.3). Antarctic all-sky ASR does have a positive trend ($74.3 \pm 81.2 \times 10^3$ PJ yr^{-1}) which is comparable to the Arctic ASR trend, however, the TTE is 38±5 years owing to larger interannual variability. Significant anomalies have been observed in recent years and it would be expected that continual rapid sea ice loss in Antarctica may exacerbate these ongoing trends. Antarctic all-sky OLR is relatively invariant ($-9.5 \pm 65.5 \times 10^3$ PJ yr^{-1}), suggesting that thermal emission in this region does not compensate recent increases in ASR. Due to the relatively unchanging OLR over the 21-year period, a reduction in the Antarctic net energy imbalance has emerged (TTE of 18±5 years), clearly driven by recent increases in ASR. The Antarctic energy deficit is decreasing through local radiative exchange at $83.7 \pm 67.4 \times 10^3$ PJ yr^{-1}, a reduction of 0.7% per decade.

As observed in the Arctic, clouds in the Antarctic also mask the underlying surface changes, reducing the magnitude of the ASR and OLR all-sky trends compared to clear-sky trend. The presence of clouds in Antarctic reduces the clear-sky ASR trend by 35%, slightly less than the reduction caused by clouds on Arctic ASR trends (50%). One notable feature of Antarctic fluxes is that clear-sky OLR has a negative (but not statistically significant) trend of appreciable magnitude ($-36.7 \pm 49.8 \times 10^3$ PJ yr^{-1}), which reduces in magnitude by about 75% compared to all-sky trends. This behavior is examined further in the following sections through examining spatial variability in the trends and the spatial impact of cloud cover. It is apparent that the trends in Antarctic radiative fluxes (especially ASR) are influenced substantially by the anomalously low SIA between 2016 and

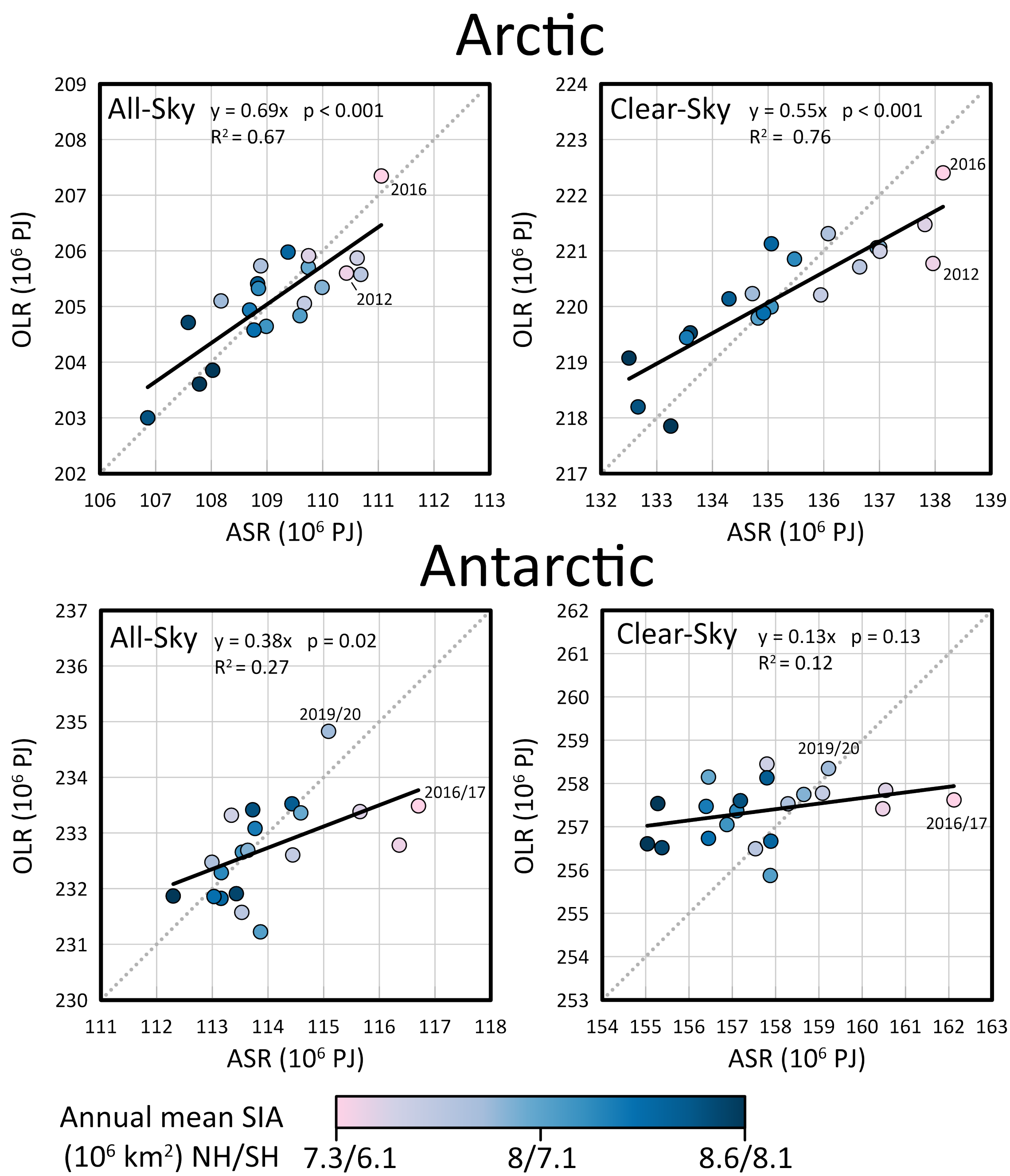

Figure 2.4: Scatterplot of annual accumulated absorbed shortwave radiation (ASR) and outgoing longwave radiation (OLR) for all-sky (left) and clear-sky (right) conditions. Annual mean sea ice area (SIA) is shown with color for both the Arctic and the Antarctic with notable years labeled. Linear regression slope, p-value and R^2 are reported.

2019 (up to 1 million km^2 smaller than the 21-year mean). The unequal variability and unexpected trends of Antarctic SIA over the last four decades has prompted researchers to prescribe caution when interpreting trends (especially linear) in the Antarctic region (Handcock and Raphael, 2020; Eayrs et al., 2021). However, merely examining the time-series themselves highlights the different responses in Antarctic ASR and OLR to changing SIA compared to the Arctic.

The annual ASR-OLR relationship in Antarctica is very weak with an R^2 of 0.27 for all-sky and 0.11 for clear-sky (Figure 2.4). The all-sky trend is statistically significant (at 95%) with a slope of 0.38, however, there are many more outliers in the relationship. The clear-sky trend is not statistically significant with a slope of 0.13, demonstrating that the variability of annual ASR has little impact on the variability of OLR. It is apparent that Antarctic ASR is closely related to the SIA, with the low sea ice years absorbing more solar radiation, but this does not necessarily correspond to increased OLR.

2.3.3 Land/ocean partitioning

While sea ice has been considered as a first order control on the energy anomalies in Figure 2.3, it is important to consider the individual roles of the land and ocean in the polar regions for varying the TOA radiative trends (Tables 2.1 and 2.2; Supplementary Figures A.4 and A.5). In the Arctic (all-sky), 65% of the ASR trend and 55% of the OLR trend comes from ocean regions with the remaining 35% and 45% being driven by changes over land. Surprisingly, the Arctic ocean-land ratios are very similar for the clear-sky ASR trend (65% from ocean) and OLR trend (55%) demonstrating that clouds do not influence the relative importance of the ocean versus land. These results also demonstrate that changes in sea ice account for a two thirds majority of the change in Arctic energy exchange with land flux changes accounting for one third.

In Antarctica, the ocean has a similar dominant role in driving ASR increases, accounting for 69% of the increasing ASR all-sky trend and 83% for the clear-sky trend (Tables 2.1 and 2.2). While the pan-Antarctic and ocean-only trends in ASR are not significant

Table 2.1: Characteristics of all-sky absorbed solar radiation (ASR), outgoing longwave radiation (OLR), and Net energy balance for the Arctic and Antarctic over the entire domain (All) and the ocean-land surface types as defined in Figure 1. Variables shown are trends shown with associated 95% confidence interval using Student's-t distribution, the standard deviation (Std dev), signal-to-noise ratio (SNR), the lag-1 (year) autocorrelation (Autocorr), and time to emergence (TTE) with the TTE standard deviation in parentheses.

		All-sky				
Region		Trend [10^3 PJ/yr]	Std dev [10^4 PJ]	SNR [dec^{-1}]	Autocorr	TTE [yr]
All Arctic	ASR	99.6±70.3	109.8	1.12	0.00	17(4)
	OLR	94.7±65.0	93.3	1.34	-0.34	12(4)
	Net	4.8±48.9	63.3	0.01	0.20	110(24)
Arctic Ocean	ASR	64.9±40.7	67.3	1.23	0.23	17(4)
	OLR	51.9±26.3	46.8	1.57	-0.19	12(4)
	Net	13.0±31.4	41.4	0.33	0.13	41(10)
Arctic Land	ASR	34.7±38.0	53.6	0.72	-0.20	19(6)
	OLR	42.9±33.5	50.8	1.01	-0.39	14(5)
	Net	-8.2±25.6	33.4	-0.25	0.28	53(11)
All Antarctic	ASR	74.3±81.2	114.7	0.72	0.48	30(5)
	OLR	-9.5±65.5	84.9	-0.11	-0.09	71(20)
	Net	83.7±67.4	101.4	0.99	0.04	18(5)
Antarctic Ocean	ASR	51.5±74.4	101.2	0.55	0.55	38(5)
	OLR	-5.4±40.5	52.5	-0.11	0.05	83(21)
	Net	57.0±59.3	84.4	0.76	0.27	25(5)
Antarctic Land	ASR	22.7±17.3	26.5	1.01	-0.13	16(5)
	OLR	-4.0±28.1	36.5	-0.11	-0.26	65(20)
	Net	26.8±22.7	33.7	0.94	-0.21	17(5)

at the 95% level, an increasing ASR trend has emerged over the Antarctic ice sheet within the period. Even though snow and ice cover on the Antarctic continent is generally unchanging, leading to relatively low year-to-year variability in the time-series, decreasing snow albedo has been observed through surface warming, especially in West Antarctica due to summertime heating (Seo et al., 2016). Thus, increasing Antarctic ASR trends over land have emerged within the 21-year record (for both all- and clear-sky). The Antarctic clear-sky OLR trend has a TTE of 23±7 years, representing a moderate reduction in the Antarctic OLR, driven mainly by changes over the ocean (60%). Since the magnitude of

Table 2.2: Same as Table 2.1, but for Clear-sky.

		Clear-sky				
Region		Trend [10^3 PJ/yr]	Std dev [10^4 PJ]	SNR [dec^{-1}]	Autocorr	TTE [yr]
All Arctic	ASR	205.5±89.9	172.5	1.81	0.03	12(3)
	OLR	127.2±57.9	108.8	1.74	-0.19	11(3)
	Net	78.3±62.9	94.6	0.98	0.09	18(5)
Arctic Ocean	ASR	133.1±50.2	105.0	2.10	0.13	11(3)
	OLR	70.2±28.5	57.1	1.95	0.16	12(3)
	Net	62.8±35.3	60.0	1.41	-0.01	14(4)
Arctic Land	ASR	72.4±45.3	73.8	1.27	-0.08	15(4)
	OLR	57.0±36.7	59.1	1.23	-0.39	12(4)
	Net	15.4±34.1	45.1	0.36	0.25	41(9)
All Antarctic	ASR	113.5±128.7	180.6	0.70	0.39	29(5)
	OLR	-36.7±49.8	68.3	-0.58	-0.15	23(7)
	Net	150.3±109.8	169.8	1.08	0.34	21(4)
Antarctic Ocean	ASR	93.9±121.3	167.2	0.61	0.45	33(6)
	OLR	-22.2±27.7	38.4	-0.64	0.25	28(6)
	Net	116.2±100.9	149.0	0.91	0.42	24(4)
Antarctic Land	ASR	19.6±21.6	30.5	0.72	-0.42	17(5)
	OLR	-14.5±30.3	40.1	-0.38	-0.32	29(9)
	Net	34.1±37.7	53.2	0.72	-0.38	17(6)

the OLR trend is small, net energy trends are dominated by the ASR changes in the ocean and the ocean-land ratio is similar to the ASR trend (69% and 83% from ocean all- and clear-sky respectively).

2.3.4 Spatial distribution

The spatial nature of these polar radiative trends is presented in Figures 2.5 and 2.6 to aid in understanding the geophysical drivers of these trends. In the Arctic, ASR is increasing broadly across the entire Arctic basin at rates of about 10-20 MJm^{-2}/yr in all-sky conditions (Figure 2.5a). Clear-sky trends reveal the fundamental role of sea ice reduction in increasing the ASR, with the regions of greatest increase of ASR aligning with the locations of enhanced sea ice loss close to the coastlines (Supplementary Figure A.6) on the order of 20-30 MJm^{-2}/yr, reaching maxima in the Kara Sea, Laptev Sea, Beaufort

Sea, and along the Denmark Strait (Figure 2.5b). Increasing ASR is also observed over northern Siberia and Alaska in clear-sky conditions. There are regions of declining ASR (not significant) in the Labrador Sea along with northeast Russia and eastern Hudson Bay. These regions align with regionally isolated increases in sea ice cover (Supplementary Figure A.6), which, paired with changes in timing of freeze and melt (Gupta et al., 2022) increases the amount of reflected solar radiation. The difference between the all- and clear-sky ASR trends reveals the locations where clouds either enhance or mask the changes to the underlying surface reflectivity (Figure 2.5c). As previously reported by Sledd and L'Ecuyer (2021), clouds reduce the magnitude of ASR trends by about 50%, with the greatest reductions of about 20 MJm^{-2}/yr over the Barents and Kara Seas. Isolated positive differences between all- and clear-sky ASR represents regions of increasing snow and ice cover, where clouds are maintaining a more constant (subdued) albedo than the changing surface beneath (in the Labrador Sea and northeast Russia).

Arctic OLR trends are much more homogenous in magnitude and spatial extent, demonstrating broad increases of 4-16 MJm^{-2}/yr across the Arctic Ocean and northern Siberia for both all- and clear-sky. Increases in OLR in the Arctic Ocean are well confined to the locations of variable sea ice area, providing evidence for the relationship between ASR, surface temperature, and OLR (similar to that observed by Sledd et al. 2023). It is also notable that all- and clear-sky trends are of very similar magnitude. The spatial difference between the isolated maxima in ASR trends and the broadly uniform OLR trends suggests an efficient redistribution of energy within the Arctic Ocean. Furthermore, in the Arctic, clouds primarily act to reduce the OLR trends, particularly in the coastal regions of the Kara Sea, Chukchi Sea, Beaufort Sea, and the Denmark Strait (Figure 2.5f).

While the pan-Arctic net energy is not changing, there are regions where the energy imbalance is changing with statistical significance (increasing and decreasing) through local processes. Positive trends in the net energy represents regions where the ASR trends exceed the OLR trends, such as in the Kara Sea, Southern Greenland, the Canadian Archipelago, and the Beaufort Sea (Figure 2.5g and 2.5h). These regions appear in both

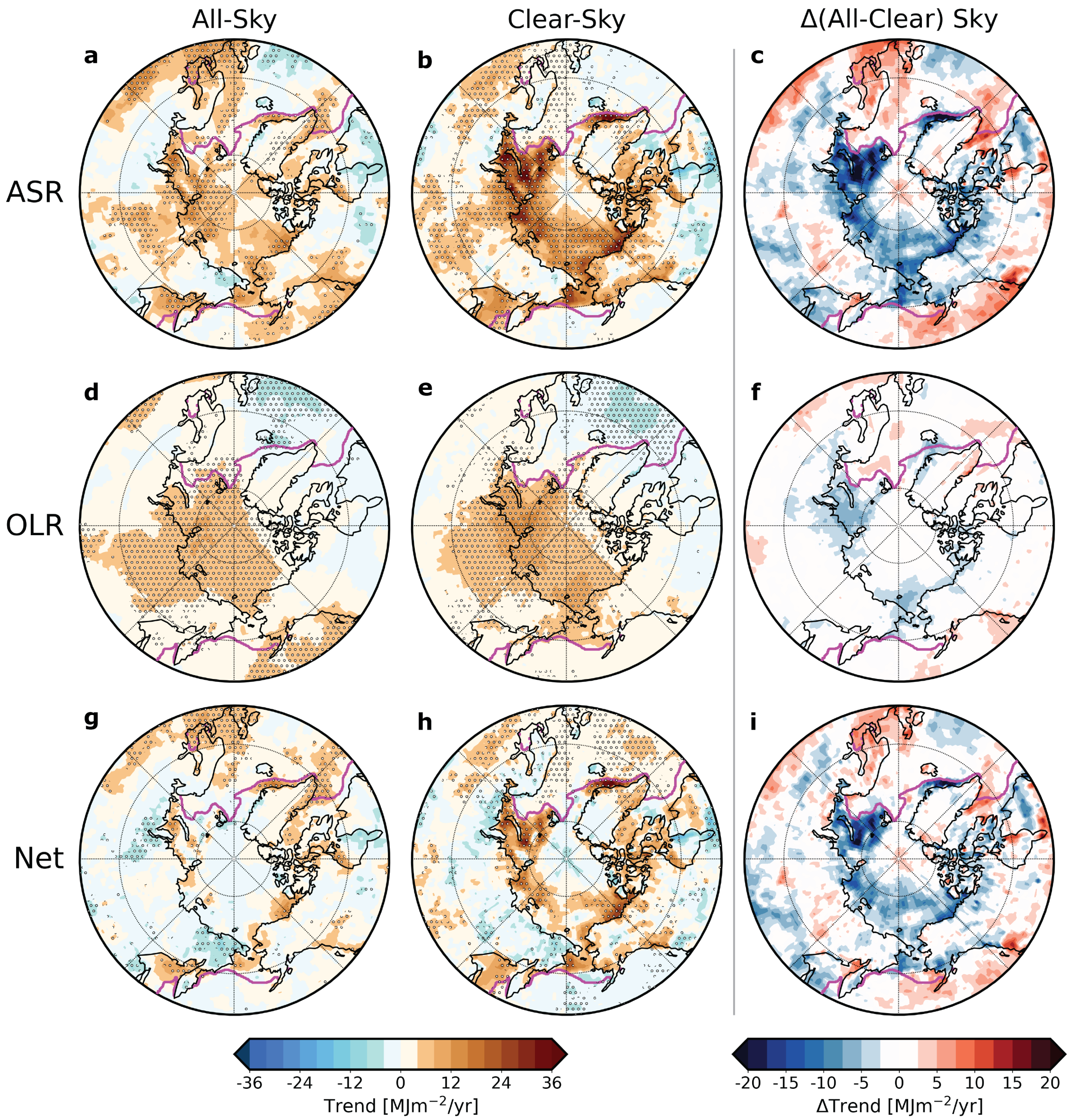

Figure 2.5: Arctic trends in absorbed shortwave radiation (ASR; a and b), outgoing longwave radiation (OLR; b and c) and Net energy (g and h) calculated for all-sky (left column) and clear-sky (center column) conditions over 2000-2020. Stippling demonstrates regions where the trend has emerged in the observational record with 95% confidence. The difference between the trends in all-sky and clear-sky are shown in the right column (c, f, and i). The magenta line indicates the mean extent of August sea ice area (over 15% concentration).

the all-sky (at about 4-8 MJm^{-2}/yr) and clear-sky trends (reaching trends of 24 MJm^{-2}/yr). Regions of negative net energy trends appear in northeast and northwest Russia and eastern Hudson Bay where increasing snow and ice cover may be increasing the albedo (reducing the ASR) while the OLR remains relatively constant. The difference between the all-sky and clear-sky net energy trends highlights the masking effect of clouds over regions of changing surface cover, reducing the magnitude of all trends by up to 50% (Figure 2.5i). These variations in local net radiative balance would be expected to be indicative of variations in local circulations in the Arctic region since energy flows down gradient, from regions of increasing absorption (positive net trends) to regions of increased thermal emission (negative net trends).

Antarctic ASR exhibits large opposing regions of increasing absorption in the Ross and Amundsen Sea along with the eastern Weddell Sea and Southern Indian Ocean (Figure 2.6a). Intriguingly, there are regions of decreasing ASR, most apparent in the clear-sky trends (Figure 2.5b) in the coastal waters of the Antarctic continent, especially adjacent to Wilkes Land. There are also regions of reducing ASR towards the sea ice edge in the Bellingshausen Sea and around the Antarctic Peninsula. A reducing ASR trend suggests that the albedo at the surface is increasing in these regions. These likely reflect regions which remain covered with sea ice for longer periods of time (as demonstrated in Supplementary Figure A.7). In contrast to the Arctic, the clear-sky trends of appreciable magnitude are entirely confined to within the region of variable sea ice, demonstrating the roughly unchanging albedo of the Southern Ocean. There are variations in all-sky ASR trends beyond the marginal sea ice zone which must be associated with changing cloud properties over the Southern Ocean. Indeed, a wavenumber 2 pattern of alternating cloud effects is apparent over the Southern Oceans (Figure 2.6c), with increased solar absorption from clouds in the Southern Atlantic and south of Australia and reducing solar absorption from changing cloud properties in the South Pacific and Indian Oceans.

The OLR trends in Antarctica are of very small magnitude compared to the ASR. The clear-sky OLR is increasing in the Amundsen and Ross Seas with much of the Antarctic

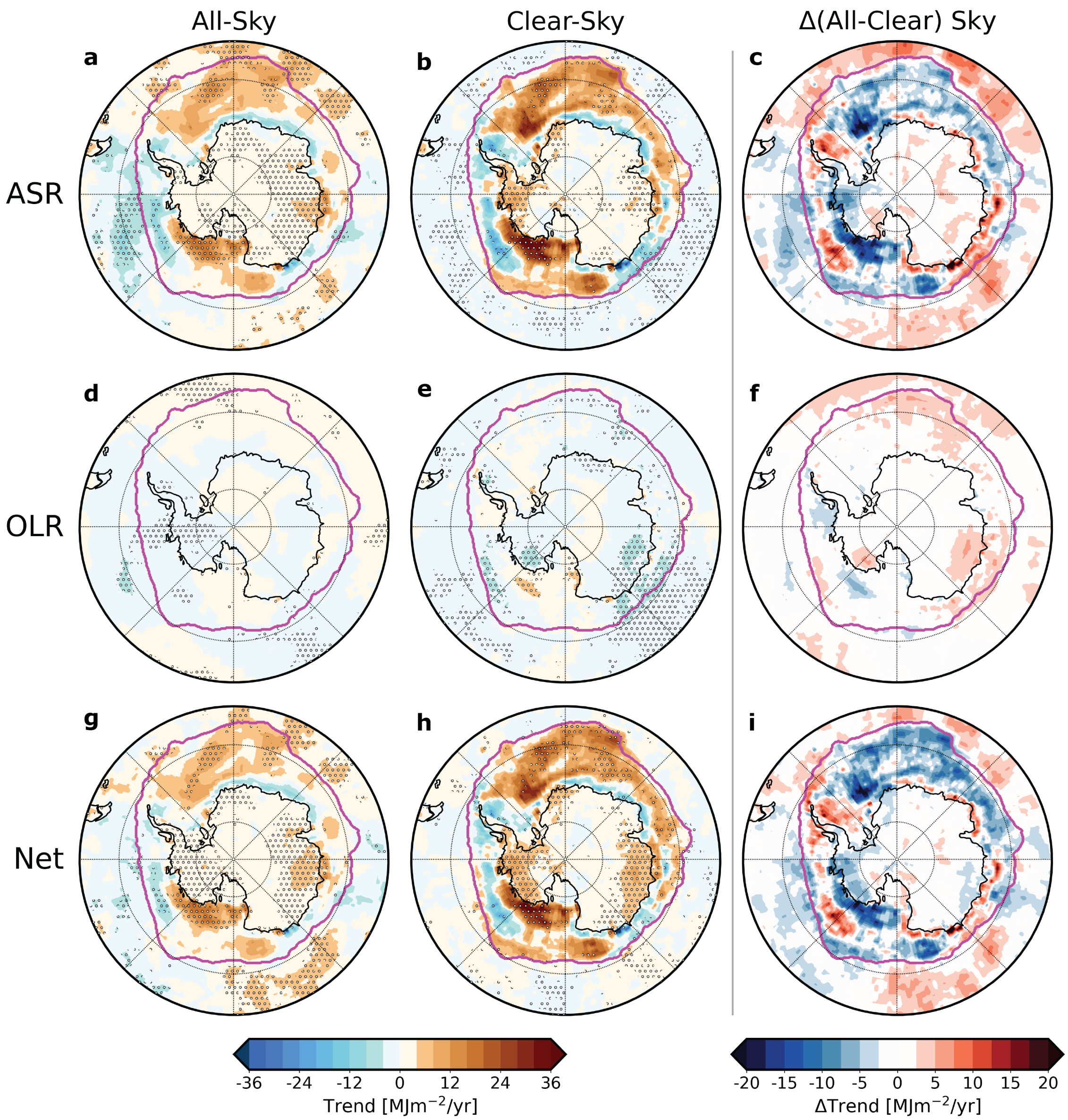

Figure 2.6: Antarctic trends in absorbed shortwave radiation (ASR; a and b), outgoing longwave radiation (OLR; b and c) and Net energy (g and h) calculated for all-sky (left column) and clear-sky (center column) conditions over 2000-2020. Stippling demonstrates regions where the trend has emerged in the observational record with 95% confidence. The difference between the trends in all-sky and clear-sky are shown in the right column (c, f, and i). The magenta line indicates the mean extent of February sea ice area (over 15% concentration).

Continent exhibiting reducing OLR. Notably, Wilkes Land (East Antarctica) and Marie Byrd Land have statistically significant decreasing OLR trends, indicating reducing thermal emission in these regions. While these may be related to local temperature trends (Nicolas and Bromwich, 2014), the melting and refreezing of snow cover would also produce such radiative trends even without a change in temperature (L'Ecuyer et al., 2021). The mid- and far-infrared emissivities of water and ice are considerably lower than the emissivity of snow, so if the snowpack were to melt and refreeze from an anomalous weather event the new ice surface would have a lower net thermal emission even at the same temperature. There is also a region of decreasing clear-sky OLR close to the historical winter ice edge in the Amundsen-Bellingshausen Seas, which may be expected as a result of ice advection from the Amundsen Sea low, which is paired with an ASR dipole in the same region. Since the trends in Antarctic ASR are almost 10-fold greater than the OLR trends, it is clear that changes in the net energy are dominated by the pattern of ASR variability which is demonstrated in the similarity between the Net and ASR Antarctic trends (Figure 2.6g-i).

2.4 Discussion

Satellite observations of the Arctic TOA radiative exchange from 2000 to 2021 reveal that both absorbed solar radiation and emitted thermal radiation are increasing at remarkably similar rates that exceed the interannual variability of 0.98 ± 0.69 Wm^{-2} dec^{-1} and 0.94 ± 0.55 Wm^{-2} dec^{-1} for ASR and OLR respectively (Figure 2.7). Figure 2.4 also demonstrates that this compensation generally occurs within a given year, with 67% of the annual accumulated OLR variability explained by the accumulated ASR. These results reveal the efficient conversion of ASR to heat in the Arctic, and the retention of that heat in a location that is able to emit to space such as the ocean surface or atmosphere. These trends agree with those previously reported by Duncan et al. (2020) from CERES-EBAF (between 2000 and 2017) of 1.3 ± 0.6 Wm^{-2} dec^{-1} and 1.1 ± 0.4 Wm^{-2} dec^{-1} for ASR and OLR, respectively, for the region poleward of 60°N. The rates presented herein are calculated from four more years of data collection, demonstrating stability and confidence in these estimates.

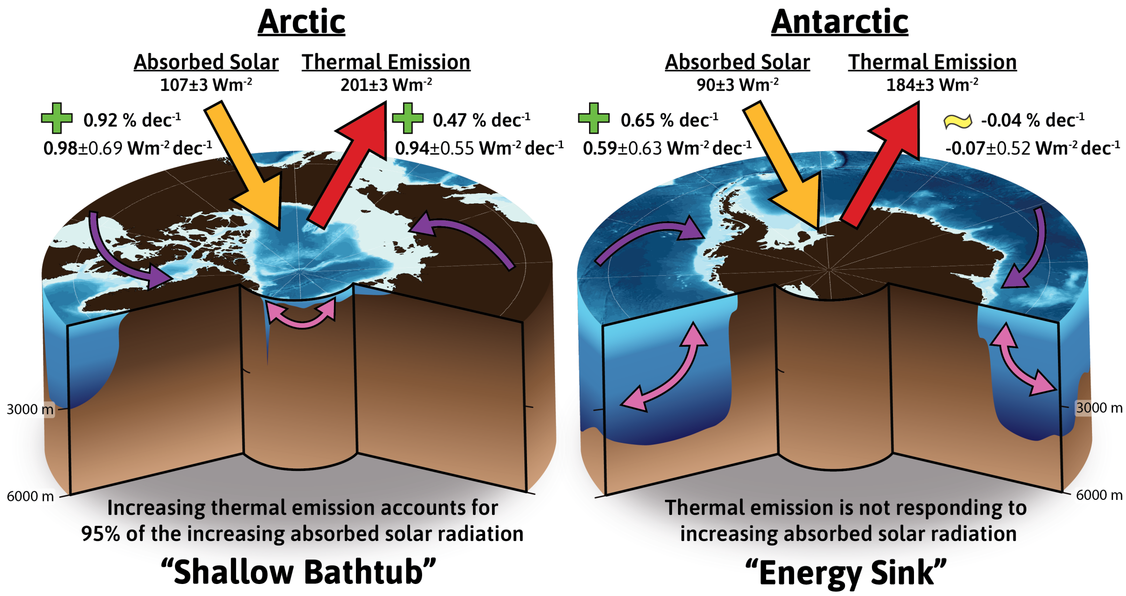

Figure 2.7: Schematic of the changing top-of-atmosphere radiative balance in the polar regions (as defined by Figure 2.1). The yellow and red arrows represent the annual mean flux of absorbed solar radiation and emitted thermal radiation respectively (presented trends have only emerged in the Arctic). The theoretical transports of energy to fulfil the energy deficit are shown with the pink (oceanic transport) and purple (atmospheric transport) arrows. The bathymetry is shown in blue with the vertical scale exaggerated to highlight the fundamental difference between the polar regions.

The locations that are losing ice cover rapidly are the same locations that are absorbing more solar radiation (Figure 2.5). The surface temperature of the Arctic must then be increasing at a rate directly comparable to the rate of increasing absorption. It is known that the ice-albedo feedback currently accounts for up to 60% of observed Arctic warming (Taylor et al., 2022). Change in sea ice area alone is not the only change that is occurring to albedo in the Arctic region, with the albedo of persistent multi-year ice declining through thinning (Riihelä et al., 2013) and snow cover change over Arctic landmasses also varying surface albedo (Duncan et al., 2020). These other surface changes allow for interpretation of the Arctic clear-sky ASR trends especially in Siberia and over regions of constant ice cover in Figure 2.5. Snow cover has not been assessed here, firstly due to the sparse record of year-round satellite retrieved Arctic snow cover and the dominance of the Arctic Ocean in driving the observed trends, accounting for 65% of the ASR trend.

It is notable that the trend in thermal emission is much more spatially uniform across the Arctic region than the regionally concentrated ASR maximums, suggesting a possible redistribution of the heat across the entire Arctic basin either through ocean or atmospheric transport. This effective mixing of heat within the Arctic region has been previously discussed by Timmermans and Marshall (2020) and Guemas et al. (2016), through the Beaufort and Laptev Sea gyres, affirming these results with geophysical explanations. The thermal inertia of the Arctic Ocean is well known, with ocean heating occurring in the summer being a sink of energy that is then emitted from the ocean in the fall and winter (Screen and Simmonds, 2010; Steele and Dickinson, 2016; Boeke and Taylor, 2018). From modeling experiments, Boeke and Taylor (2018) further highlight the importance of the relatively shallow Arctic Ocean mixed layer for trapping solar heating at the surface in the Arctic. Enhanced ocean surface heating increases the upper ocean stability, disallowing mixing of heat downwards and encouraging the development of sea surface temperature maximums which increases the outgoing thermal radiation following absorption of solar radiation (Boeke and Taylor, 2018). Indeed, Blanchard-Wrigglesworth et al. (2011) and Landy et al. (2022) both demonstrate predictability of growth season (winter) sea ice area and volume from melt season (summer) characteristics primarily through ocean temperature anomalies, providing further evidence for the dependence of year-round thermal emission on variable ASR through heat storage in the Arctic Ocean. The fact that the Arctic net radiation is not changing demonstrates that changes to the radiative balance through ASR increases are being balanced effectively by OLR, suggesting that radiatively, the Arctic is acting as a self-contained system (in agreement with Stuecker et al. 2018). Through this understanding, we describe the Arctic Ocean as a 'Shallow Bathtub'; an enclosed basin with low connectivity to mix with lower latitudes and a small amount of water available for warming, primarily due to a shallow, stable mixed layer that re-emits the vast majority of absorbed energy within a given year (Figure 2.7).

The lack of significant trends in Antarctic ASR and OLR is unsurprising given the complex relationship between global warming, regional surface temperature and sea ice loss in this region (Parkinson, 2019). The presented TOA radiative record shows very little alignment between trends in absorbed solar radiation and the amount of thermal emission in the region, with no statistically relationship in the clear-sky record and very low R^2 for the all-sky record. Antarctic ASR is increasing at 0.59 ± 0.63 Wm^{-2} dec^{-1} and the OLR trend is effectively zero at -0.07 ± 0.50 Wm^{-2} dec^{-1} (however both these trends are not statistically significant). These results align well with results from modeling experiments demonstrating that Antarctic Amplification will be driven by other feedbacks apart from the ice-albedo feedback, such as changes in moisture transport (Goosse et al., 2018; Smith et al., 2019; Hahn et al., 2021). This appears to be consistent with the presented observational results, demonstrating that varying solar absorption due to variable sea ice cover does not currently contribute to surface warming. The spatial structure of Antarctic ASR and OLR trends requires additional examination. While the region wide clear-sky ASR and OLR trends do not appear to align, the region of maximum solar absorption in the Ross Sea is colocated with a region of increased thermal emission which aligns with an isolated region of surface warming (Armour et al., 2016). In contrast, the increasing absorption between the Weddell Sea and Southern Indian Ocean is not associated with increasing OLR and is associated as a location of substantial ocean heat uptake and transport (Huguenin et al., 2022).

The presented conclusions are supported by trends in region wide ocean heat content (OHC), SST, and atmospheric heat transport (AHT) into the region (Figure 2.8; from ORAS5 and ERA5 reanalysis). The Antarctic region OHC has increased at significant rates in the last 20 years, much greater than the OHC increases in the Arctic. Importantly, while Arctic OHC is increasing at a much lower rate than the Antarctic, the Arctic summertime SST is increasing at a greater rate. This easily demonstrates that the warming that is occurring in the Arctic Ocean (through increasing ASR) is doing so primarily at the ocean surface (or mixed-layer) which will contribute to TOA OLR. Comparatively, the lack of increasing SST in Antarctica, given the rapid increase in OHC (equivalent to an increase of 1.3 Wm^{-2} in the region over 20 years), indicates that the heating is occurring

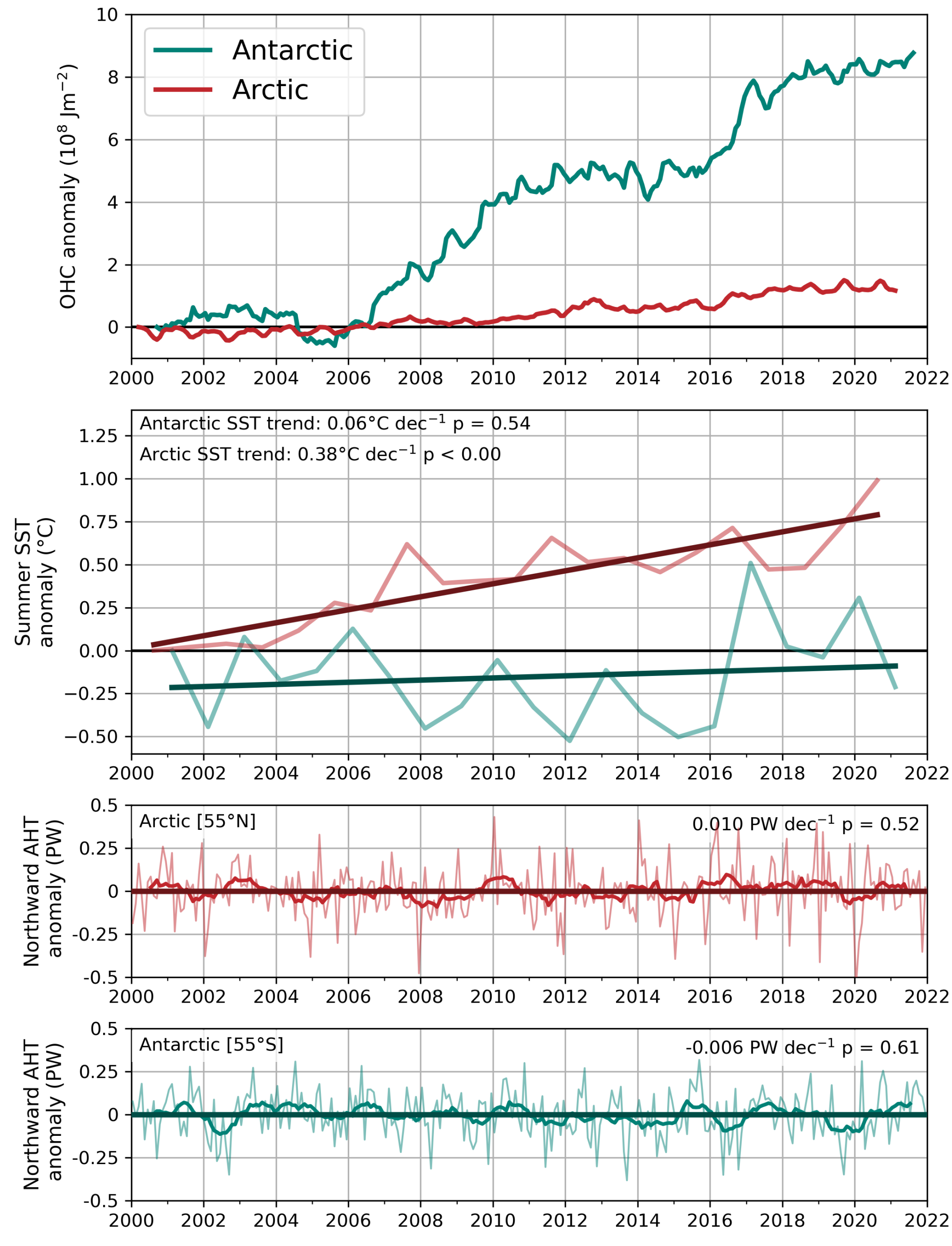

Figure 2.8: Time series of monthly deseasonalized ocean heat content (OHC) anomaly, summertime sea surface temperature (SST; September and February for the Arctic and Antarctica respectively) and monthly deseasonalized zonal mean atmospheric heat transport (AHT) for the Arctic and Antarctic (from ORAS5 and ERA5). OHC and SST are calculated as area means (as defined in Figure 2) and AHT is calculated from a zonal band at 55°N and 55°S for the Arctic and Antarctic respectively. Linear trends of SST and AHT are plotted and reported and the AHT 12 month running mean is also shown.

at some depth below the surface and therefore not contributing to the emitting radiation from the ocean surface. Antarctic ocean ASR is increasing at 0.6 Wm^{-2} (Supplemental Table A.1), demonstrating that OHC increases in the Southern Ocean are consistent with ASR trends. Secondly, since the OHC trend exceeds local ASR trends by about half (1.3 Wm^{-2} compared to 0.6 Wm^{-2}), the deficit must be accounted for by meridional energy transport from lower latitudes. The more southerly (although not significant) trend in Antarctic AHT of -0.006 PW dec^{-1} corresponds to roughly 0.5 Wm^{-2} increase over the same period in the maritime region around Antarctica (indicated in Figure 2.2), which as a rough estimate appears to close the energy balance for this region. These findings firmly corroborate the importance of ocean heat uptake in Antarctica from both radiative and turbulent sources, identifying a significant sink of energy, that is increasing in magnitude over time, especially as sea ice area reduces. Morrison et al. (2016) and Armour et al. (2016) describe this effective ocean heat uptake around Antarctica and the equatorward advection and downwelling of this energy, facilitating warming at lower latitudes and in the subsurface Southern Ocean driven by the Antarctic Circumpolar Current. With this understanding, we describe the ocean surrounding Antarctic as an 'Energy Sink' due to its effective ability to absorb solar radiation (of increasing amounts) and sequestering the energy deep into the Southern Ocean (Figure 2.7). The consequence of this absorption and accumulation of energy into the Earth system remains a fundamental question in our understanding of ongoing anthropogenic climate change.

The lack of appreciable change in the Arctic net energy implies that either the poleward heat transport is unchanging or that any change is being effectively compensated by other processes (other than emission to space). This conclusion would demonstrate that there is low connectivity to energetic variability outside of the region which would be expected to modulate the ASR-OLR relationship (as examined by Steele et al. 2010, Steele and Dickinson 2016, and Stuecker et al. 2018). Reanalysis suggests that poleward AHT may have increased slightly by 0.01 PW dec^{-1} (although not significant) or 0.6 Wm^{-2} into the Arctic region over the last two decades (Figure 2.8), which could be expected to have an influence on TOA OLR. It may be true that some sequestered ASR into the Arctic Ocean is being compensated by this increasing AHT, allowing for OLR to match the ASR. However, it would indeed be surprising if the increasing rate the AHT is increasing the OLR to so closely match the observed increasing rate of ASR. Importantly, the lack of significant trend in AHT into both the Arctic and Antarctic emphasize the importance of local radiative exchange in driving changes observed in the TOA energy balance.

2.5 Conclusion

Analysis of the CERES-EBAF TOA satellite record in both polar regions has quantified the variable rates of solar absorption and thermal emission in both the Arctic and Antarctica over the last 21 years. Arctic all-sky ASR is increasing at 0.98 ± 0.69 Wm^{-2} dec^{-1}, corroborating previous studies. All-sky OLR trends are remarkably similar at 0.94 ± 0.55 Wm^{-2} dec^{-1}. These compensating trends result in no significant trend in Arctic energy uptake despite rapid ice loss and increasing solar absorption demonstrating rapid adjustment of the regions temperature to solar absorption. The effective re-emission of ASR in the Arctic is attributed to heat uptake in the Arctic ocean mixed layer with little mixing downward or equatorward, keeping absorbed energy within the Arctic basin and emitting as OLR within a given year. The observations further indicate that clouds mask Arctic solar absorption trends (50%) far more effectively than thermal emission trends (10%). In the absence of clouds, Arctic sea ice loss results in considerably larger trends in ASR (2.01 ± 0.88 Wm^{-2} dec^{-1}) than thermal emission (1.24 ± 0.56 Wm^{-2} dec^{-1}). Clouds substantially mask trends in Arctic solar absorption relative to clear-sky while having only a modest impact on thermal emission trends. As a result, the Arctic net radiation imbalance has not changed over the period due to the unequal impact of clouds on solar and thermal radiation. The presented conclusions regarding the importance of cloud cover are drawn from the observed role of clouds and therefore act as a thought experiment. The true response of the cloud-free Arctic to changes in sea ice are complicated by numerous other factors, including heat transport from lower latitudes and exposure of new moisture sources; further modeling experiments are required to fully untangle the complexities of changing sea ice on cloud cover.

These conclusions do not hold true for Antarctica where all-sky ASR trends far exceed OLR trends, decreasing the energy deficit through local radiative exchange at a rate of 0.7% per decade. The Antarctic thermal emission remains relatively unchanged even with recent reductions in sea ice area causing increased solar absorption. While some regions in the Ross Sea exhibit increased thermal emission, a large region between the Weddell Sea and the Southern Indian Ocean is absorbing more solar radiation without a compensating thermal emission. The resultant increasing TOA net energy budget (reducing polar deficit) demonstrates an implied pathway of energy into the Southern Ocean that is increasing in magnitude over the satellite record. The all-sky time to emergence of the Arctic for ASR and OLR is within the 21-year record demonstrating emergence of these trends, while neither ASR or OLR has emerged in Antarctica.

Importantly, there is substantial interannual variability in the net energy at both poles of comparable magnitude and following energy conservation, this must be accompanied by a compensating pathway of energy, either through oceanic or atmospheric meridional energy transport. Discerning between the oceanic and atmospheric components of this variability remains an important, ongoing focus of study, connecting polar energy deficits to the general circulation of the atmosphere. We presented an initial examination of reanalysis heat transport and storage to support the discussion but a robust comparison between observations, reanalysis, and model output is required to understand how well these conclusions are represented from different data sources. The presented research also highlights the importance of continuity in the measurement of Earth's energy budget to quantify the changing disposition of energy within the Earth system, providing timely justification for NASA's first Earth Venture Continuity mission, Libera (Pilewskie and Hakuba, 2020). The quantified trends in polar energy balance over the last two decades provides a benchmark for both climate model validation and to track the observed, changing geophysical processes in these sensitive regions.

Chapter 3

Constraining Atmospheric Heat Transport from Earth Energy Budget Observations

3.1 Introduction

The most fundamental role of Earth's atmospheric circulation is to redistribute heat on the planet. Atmospheric heat transport (AHT) accompanies the oceanic heat transport (OHT) to determine the total global meridional heat transport (MHT), which continuously acts to moderate the equator-to-pole energy gradient forced by the Earth-sun geometry (Oort and Vonder Haar, 1976; Fasullo and Trenberth, 2008; Armour et al., 2019). The magnitude of MHT is defined by the polarward gradient in the top-of-atmosphere (TOA) energy flux (balancing absorbed solar and emitted thermal radiation), with the surplus at the equator being balanced by equivalent deficits in the extratropics and poles (Figure 3.1a,b,c). AHT is therefore set by spatial gradients in energy input to the atmosphere

This chapter is an edited version of the peer-reviewed publication:
Prince, H. D., Donohoe, A. and L'Ecuyer, T. S. (2025). Constraining Atmospheric Heat Transport from Earth Energy Budget Observations. Journal of Climate, [in review].

(Oort, 1971; Trenberth, 1997). Globally, the atmosphere absorbs energy from solar radiation and turbulent (latent plus sensible) heat fluxes from the surface, which is balanced by the thermal emission of longwave radiation (Figure 3.1d). While Earth's AHT closes the atmospheric *energetic* budget, it must also be consistent with the net result of *dynamic* mixing of moist static energy (MSE) through atmospheric motions (Armour et al., 2019). These perspectives (*energetic* and *dynamic*) must be equal and complimentary, providing differing theoretical perspectives of the same physical process. Importantly, this concept introduces two distinct methods to calculate AHT, as demonstrated by Armour et al. (2019).

Earth's AHT is innately connected to the climate system, permitting closure between energetic processes while being congruent with numerous aspects of the observed weather and climate, including Earth's average temperature (North et al., 1981), polar amplification (Hwang et al., 2011; Merlis and Henry, 2018; Hahn et al., 2021), the frequency of deep convection (Riehl and Malkus, 1958; Stephens et al., 2024), the efficiency of midlatitude cyclones (Armour et al., 2019), and the distribution of precipitation (Held and Soden, 2006; Donohoe et al., 2014). But despite its importance, few studies have examined the consistency between AHT calculated from the *dynamic* approach with observational estimates of the atmospheric energy budget. Bollmeyer and Hense (2014) for example, demonstrates inconsistency between energy transport and the atmospheric flux divergence in the long term annual mean using reanalysis and limited observational datasets. Improved observations of the atmospheric and surface energy budget at monthly timescales, as described by L'Ecuyer et al. (2015) and Mayer et al. (2024) provide a new opportunity to compare these perspectives at the sub-annual timescale. Furthermore, recent assessments of historical AHT trends between *dynamic* calculations from different atmospheric reanalyses show inconsistent trends, which are beyond climate model projections (Cox et al., 2024a), driving the need to develop observation-based, independent records of AHT. Continual and advancing satellite observations, paired with data processing efforts, now provides the opportunity to explore the plausibility of such an analysis.

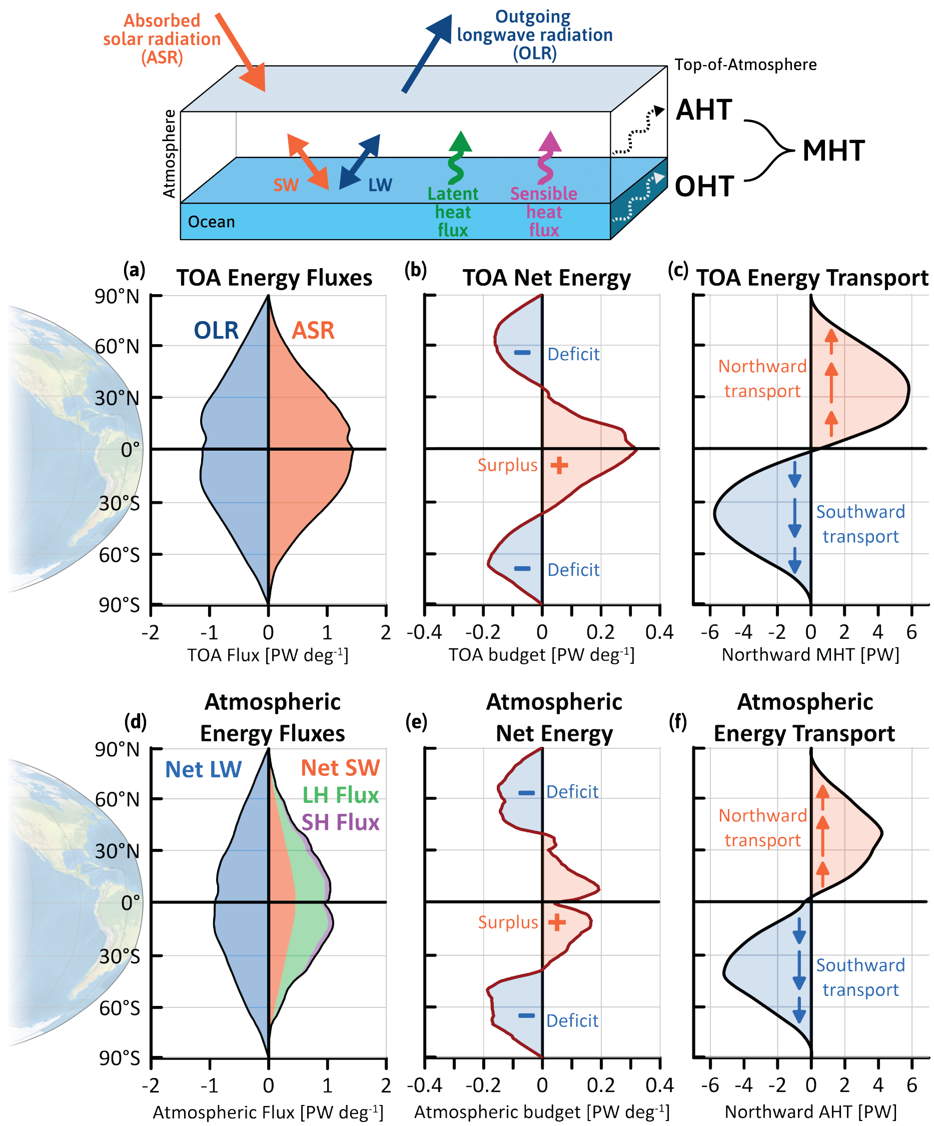

Figure 3.1: (upper) Schematic of energetic fluxes at the top-of-atmosphere (TOA) and at Earth's surface demonstrating the relevant fluxes for meridional heat transport. (a, d) Annual-zonal mean energetic fluxes from the TOA and atmosphere of net longwave radiation (blue), net shortwave radiation (orange), latent heat fluxes (green), and sensible heat fluxes (purple). Positive fluxes represent net energy receipts into the atmosphere from the TOA (in a) and from both TOA and surface (in d). (b, e) The net energy budget calculated at TOA and for the atmosphere is shown along with the zonal mean MHT and AHT (c, f), calculated as the integral of the net energy budget, from one pole to other. Schematic is based on fluxes from ERA5.

The *dynamic* perspective considers the result of large scale overturning and mesoscale (eddy) circulations, redistributing heat absorbed by the atmosphere. It is by far the most common method used to calculate AHT (Trenberth, 1997; Fasullo and Trenberth, 2008; Armour et al., 2019; Donohoe et al., 2020; Cox et al., 2024a). Through this understanding, AHT is calculated as the zonally integrated meridional transport of moist static energy (MSE) $= c_pT + L_vq + gZ$, where T is atmospheric temperature, c_p is specific heat of air at constant pressure, L_v is the latent heat of vaporization, q is specific humidity, g is gravity, and Z is geopotential height (gZ = potential energy at height Z). The vertically and zonally integrated AHT in this framework is therefore

$$\mathrm{AHT}(\phi) = \frac{2\pi a\cos(\phi)}{g}\int_0^{\overline{P_s}} \left(\underbrace{[\bar{v}]^{\dagger}[\mathrm{MSE}]^{\dagger}}_{\mathrm{MOC}} + \underbrace{[v^{*}\mathrm{MSE}^{*}]}_{\mathrm{SE}} + \underbrace{\overline{[v^{*\prime}\mathrm{MSE}^{*\prime}]} + \overline{[v]^{\prime}[\mathrm{MSE}]^{\prime}}}_{\text{Transient eddies}}\right) dp \quad (3.1)$$

where v is the meridional wind, p is pressure ($\overline{P_s}$ is the climatological surface pressure), a is the radius of earth, square brackets [] denote zonal averages, overbars ($\overline{X}$) denote time means, asterisks (*) denote departures from the zonal average, and primes ($'$) denote departures from the time average. Daggers (†) represent departures from the vertical average in order to maintain mass conservation in the MOC (Cox et al., 2024a). AHT in this perspective may be characterized into contributions from meridional overturning circulation (MOC), stationary eddies (SE), and transient eddies (TE). This formulation is commonly calculated from models and reanalysis instantaneous data at high temporal (e.g. 6 hourly), spatial (<1°), and vertical (>40 levels) resolutions (Donohoe et al., 2020). *Dynamic* AHT requires knowledge of MSE and winds throughout the atmosphere, which are not directly observed but can be estimated using atmospheric reanalysis.

The *energetic* perspective diagnoses AHT from the spatial structure of the atmospheric energy budget (as represented in Figure 3.1)

$$\mathrm{AHT} = 2\pi a^2 \int_{-90}^{\phi} \cos(\phi)\left(Q_{RAD} + \mathrm{SH} + \mathrm{LH} - \mathrm{AET}\right) d\phi \quad (3.2)$$

where SH and LH are the sensible and latent heat fluxes respectively and Q_{RAD} is the net radiation absorbed by and emitted from the atmosphere, which is equal to the net radiative flux into the atmosphere from TOA and at the surface:

$$Q_{RAD} = \underbrace{\mathrm{ASR} - \mathrm{OLR}}_{\text{TOA radiation}} + \underbrace{\mathrm{SW}\uparrow - \mathrm{SW}\downarrow + \mathrm{LW}\uparrow - \mathrm{LW}\downarrow}_{\text{Surface radiation}} \tag{3.3}$$

where ASR is the TOA absorbed solar radiation and OLR is the TOA outgoing longwave radiation. SW and LW represent shortwave and longwave fluxes at Earth's surface where upward arrows represent a flux into the atmosphere and downward arrows represent a flux towards the surface. The final term in Eq. 3.2 is the monthly atmospheric energy tendency (AET), which is calculated following Mayer et al. (2017)

$$\mathrm{AET} = \frac{1}{g}\int_0^{p_s} \frac{d}{dt}\left[(1-q)\,c_v T + L_v q + \Phi + k\right] dp \tag{3.4}$$

where p_s is the surface pressure, c_v is the specific heat of dry air at constant pressure, Φ is the potential energy, and k is the kinetic energy. Observing these properties throughout the atmosphere is unattainable and reanalysis data must be utilized to calculated the AET. The AET does average to zero (at least close to zero relative to the seasonal cycle) in the annual mean and so is only important when considering sub-annual AHT variations. While these tendency terms cannot be directly observed through the atmosphere, there is consistency in the long-term variance between reanalysis and other observed datasets (Trenberth et al., 2001; Mayer et al., 2019; von Schuckmann et al., 2023). This tendency definition assumes that the contribution of enthalpy from water vapor is negligible through explicitly only calculating the enthalpy of dry air (through the assumption that the enthalpy flux associated with lateral moisture flux convergence is balanced by that of the moisture removal from the column by precipitation; Mayer et al. 2017). This is in slight contrast to the MSE definition utilized by the Cox et al. 2024a AHT (Eq. 3.1) which assumes that the enthalpy of the column can be approximated by assuming the column is dry air ($q = o$), which additionally allows the vertically integrated geopotential to be expressed as a function of temperature only since $\frac{1}{g}\int_0^{P_S}[C_vT+\Phi]dP = \frac{1}{g}\int_0^{P_S}[C_pT]dP$ (since $C_p = C_v + R$). This approximation also assumes an ideal gas in a hydrostatic atmosphere where a change in the center of gravity is only the result of thermal expansion, accounted for by the heat capacity at constant pressure (Lorenz, 1955).

The other components of Eq. 3.2 can largely be constrained by observations. Modern, continuous measurement of Earth radiation budget began in March 2000 with the NASA Clouds and Earth's Radiant Energy System (CERES; Loeb et al. 2018), providing authoritative measurements of Earth's TOA and surface radiative fluxes, which are consistent with observations of global ocean heat uptake through the CERES Energy Balance and Filled (EBAF) product (Loeb et al., 2018). The CERES-EBAF TOA and surface net radiation measurements have uncertainties of up to 5 and 8 Wm^{-2} respectively, at 1°×1° monthly resolution (Loeb et al., 2009; Kato et al., 2018). The remaining components required for Eq. 3.2 are the surface turbulent heat fluxes. The calculation of global-scale surface turbulent fluxes has long been a leading constraint on observational records of Earth's climate system (Trenberth and Solomon, 1994; Liu et al., 2015; Yu, 2019; Loeb et al., 2022). Surface turbulent heat fluxes are highly variable in both space and time and ongoing, direct observation of these fluxes (such as through eddy covariance techniques) are very sparse (Pastorello et al., 2020; Tang et al., 2024). However, various approximations have been developed to calculate surface turbulent heat fluxes from readily available observed meteorology (Yu, 2019). Through these parameterizations, observational-based records of turbulent heat fluxes can be developed from satellite observations of near surface temperature, humidity, and wind speed (Curry et al., 2004).

Historically, the accuracy of these global calculations has not been sufficient for climate science with concerns due to data accuracy and coverage along with uncertainties in parameterizations and empirical coefficients (Trenberth and Solomon, 1994). Specifically, the global surface energy budget is not closed (residuals are on the order of 20 Wm^{-2}; L'Ecuyer et al. 2015) and, thus, the observed surface energy budget has been excluded from analysis of Earth's energy accumulation and from calculations of the atmospheric energy budget. Instead, when surface flux estimates have been required in global energy studies, the common solution has been to calculate them as the residual between TOA radiation (commonly from CERES-EBAF) and atmospheric energy transports (vertically integrated MSE transport; Eq. 3.1) as derived from reanalysis (Trenberth and Solomon, 1994; Trenberth, 1997; Trenberth and Fasullo, 2018; Liu et al., 2015, 2017, 2020; Loeb et al., 2022; Mayer et al., 2022b; Pan et al., 2023). However, continual effort has been made to improve observations of the surface energy budget (L'Ecuyer et al., 2015; Tang et al., 2024). Modern satellite retrieved surface turbulent heat flux products show closer agreement with buoy observations than reanalysis (Tang et al., 2024). Although, these satellite retrievals are tuned to the buoy-based fluxes and both of which utilize similar parameterizations (based on vertical gradients in temperature, moisture, and wind speed) so the level of agreement is unsurprising and these data cannot be considered independent. It is possible that these observations are both biased with respect to the true nature of Earth's surface energy budget (further discussed by Mayer et al. 2022b). The calculation of *energetic* AHT (as represented in Eq. 3.2) considers the meridional gradient in the zonal mean atmospheric energy budget, so while the absolute fluxes may be biased, the derived AHT may be realistic. Furthermore, in this manuscript, we will also examine the temporal variability (on monthly time scales) of the observed *energetic* AHT, which theoretically could be in agreement with reanalysis despite mean state differences.

Through energy conservation, AHT must, on long enough time scales, close to zero with no transport through the poles (Oort, 1971; Trenberth et al., 2019; Armour et al., 2019; Donohoe et al., 2020). In practice however, all attempts to calculate *energetic* AHT (and more generally Earth's total meridional heat transport) from reanalysis, models, and observations do not meet closure requirements. The lack of closure is attributed to errors in the observational data (e.g. TOA radiation), lack of internal closure within models/reanalysis, or long-term energy uptake within the Earth system, such as through deep ocean heat uptake, global ice volume changes, changes in land surface evaporation minus precipitation, and land heat storage (Trenberth et al., 2016, 2019; Donohoe et al., 2020; Johnson et al., 2023). This departure from energy conservation is commonly assumed to be uniform across all latitudes, and the standard solution is to subtract the non-zero global mean net energy from the integrand (in Eq. 3.2), effectively taking the integral of the zonal energetic anomaly, which mathematically must have closure while also effectively bias correcting the input datasets (Trenberth et al., 2019; Armour et al., 2019; Donohoe et al., 2020). This approach will also be utilized here; however, its requirement raises fundamental questions about the validity of our accounting of Earth's energy balance.

3.2 Datasets and Methodology

Here, we present a methodology to calculate and validate an observed AHT product through the *energetic* AHT perspective (Eq. 3.2). CERES-EBAF (Loeb et al., 2018) provides monthly radiative fluxes at TOA and at the surface and will be used as the radiative observations throughout this work (Table 1). With the radiative balance accounted for, a key component of this research is examining the validity of observations of global surface turbulent flux data. Surface sensible and latent turbulent heat flux observations are calculated through bulk flux models which require knowledge of surface temperature, air temperature, wind speed, and humidity, all of which are readily available from numerous satellite products (Curry et al., 2004). The five observational products used herein are (Table 1): the NASA SeaFlux version 3 dataset (Roberts et al., 2020), the Woods Hole Oceanographic Institution (WHOI) Objectively Analyzed Air Sea Fluxes for the Global Oceans (OAFlux) version 3 dataset (Yu et al., 2008), the Japanese Ocean Flux Data Set with Use of Remote Sensing Observations (J-OFURO) version 3 dataset (Tomita et al., 2019), the Hamburg Ocean Atmosphere Parameters and Fluxes from Satellite Data (HOAPS) version 4 dataset (Andersson et al., 2010), and the French Research Institute for Exploitation of the Sea (IFREMER) version 4 dataset (Bentamy et al., 2013).

Notably, all five of these data products rely on various versions of the Coupled Ocean–Atmosphere Response Experiment (COARE) bulk algorithm to calculate their surface turbulent heat fluxes (Tang et al., 2024). The COARE algorithm has been refined for decades (improving atmospheric stability, surface roughness, and wave parameterizations to name a few; Fairall et al. 1996, 2003; Edson et al. 2013). The COARE algorithm does account for various complexities such a temperature variable latent heat of vaporization (for pure and sea water) and the sensible heat flux of rain falling on the ocean surface (on average 2.3 Wm^{-2} globally), however, there are a number of physical characteristics that are unable to be accurately captured including the role of sea spray, snowfall, and the enthalpy of moisture transport, effects which are either lacking in observations or have effects well below the accuracy of the bulk flux approach (Fairall et al., 1996). While these different datasets use a wide variety of data sources, they all heavily rely on passive (radiometers) and active (scatterometers) microwave sensors for surface wind speed, temperature, and near surface humidity along with available ship and buoy records. There are only a limited number of historical satellites retrieving the required variables and so these products share similar data sources and cannot be considered independent records. Many of the turbulent flux datasets also ingest reanalysis in a hybrid manner, such as through optimal synthesis (e.g., Yu et al. 2008). Robertson et al. (2020) provides a thorough description of the uncertainty in these satellite-based estimates of the latent heat flux, noting that limited coverage of Earth observing satellites along with instrument specific biases that introduce errors in these records.

Table 3.1: Observation data products used throughout this study.

Variable	Source	Citation
Radiation (TOA and Surface)	CERES-EBAF v4.2	Loeb et al. (2018)
Turbulent Heat Fluxes (Ocean)	SeaFlux v3	Curry et al. (2004); Roberts et al. (2020)
	OAFlux v3	Yu et al. (2008)
	J-OFURO v3	Tomita et al. (2019)
	IFRAMER v4	Bentamy et al. (2013)
	HOAPS v4	Andersson et al. (2010)
Turbulent Heat Fluxes (Land)	GLDAS v2.2	Rodell et al. (2004)
Net Atmospheric Energy	DEEP-C v5	Liu and Allan (2022)

These five independent products provide surface turbulent flux data over the oceans.

Additional data sources must be utilized to characterize land-air turbulent heat fluxes. Here, we utilize the NASA Global Land Data Assimilation System version 2.2 for the land surface turbulent heat fluxes (GLDAS; Rodell et al. 2004; Beaudoing and Rodell 2020). GLDAS utilizes satellite- and ground-observations, paired with meteorological forcing from reanalysis, to provide high quality global land surface fluxes and is utilized in numerous weather and climate models. GLDAS calculations are not direct observations, but may be considered closer to reality than surface fluxes directly from reanalysis due to the improved treatment of the land surface (as an observation-integrating model; Rodell et al. 2004, 2015). Due to uncertainties in global surface properties and the innate heterogeneity of Earth's surface, numerous other versions of GLDAS have been published using different land surface models, considering different depths below surface, along with varying vegetation parameters: Noah, Catchment LSM (CLSM), and Variable Infiltration Capacity (VIC). We utilize the most recent GLDAS release, Version 2.2, with these other (Version 2) models being used for sensitivity testing in Appendix B. All surface flux data products (for both land and ocean) were collated by the NASA Energy and Water cycle study (NEWS), which regridded all products to $1°\times1°$ resolution and averaged to monthly timescales (L'Ecuyer et al., 2015; Rodell et al., 2015). Gaps and poorly constrained regions in the observational record, such as in the poles and over small islands, are filled using time-varying MERRA-2 ocean and land fluxes, consistent across all surface turbulent flux data (Rodell et al., 2015). The temporal range of these different data vary considerably, and so the longest common time span between all products is used, comprising a decade between 2004 and 2014.

Dynamically calculated AHT (Eq. 3.1) from reanalysis form the baseline to assess the level of agreement with the observation derived AHT. Dynamic AHT is calculated (following Cox et al. 2024a) from ERA5 (Hersbach et al., 2018), MERRA2 (Gelaro et al., 2017), and JRA-55 (Kobayashi et al., 2015). Additionally, an independent calculation of mass-consistent AHT as calculated by Mayer et al. (2017, 2022a) from ERA5 is also used for further validation ($\mathrm{ERA5_{Mayer}}$). The Mayer et al. (2017) AHT explicitly closes the atmospheric mass and energy budget at every timestep with a number of additional details such as considering kinetic energy and variable surface pressure. The Cox et al. (2024a) AHT makes a number of simplifying assumptions, specifically that kinetic energy is negligible, the sensible heat of the column can be approximated by assuming the column is dry air, and assuming a fixed mass of the atmosphere by considering a time-invariant but spatially variable mass/surface pressure. The same AET (Eq. 3.4) is used throughout this study, calculated from ERA5 by Mayer et al. (2022a) as the exact difference between the first time steps of each month. This tendency term is used for all calculations of energetic AHT, both from reanalysis and observations. From $\text{ERA5}_{\text{Mayer}}$, Liu and Allan (2022) derived the atmospheric energy budget as the residual, which provides an independent measure of the atmospheric energy budget (at both the surface and TOA) that is consistent with the $\text{ERA5}_{\text{Mayer}}$ AHT, named the Diagnosing Earth's Energy Pathways in the Climate system (DEEP-C; version 5; Liu and Allan 2022). Finally, ERA5 radiation and turbulent fluxes will also be used to calculate energetic AHT ($\text{ERA5}_{\text{Energetic}}$) to test the consistency between dynamic and energetic calculated AHT from a reanalysis. Figure 3.2 presents a schematic of all datasets used herein along with the various ways to derive AHT.

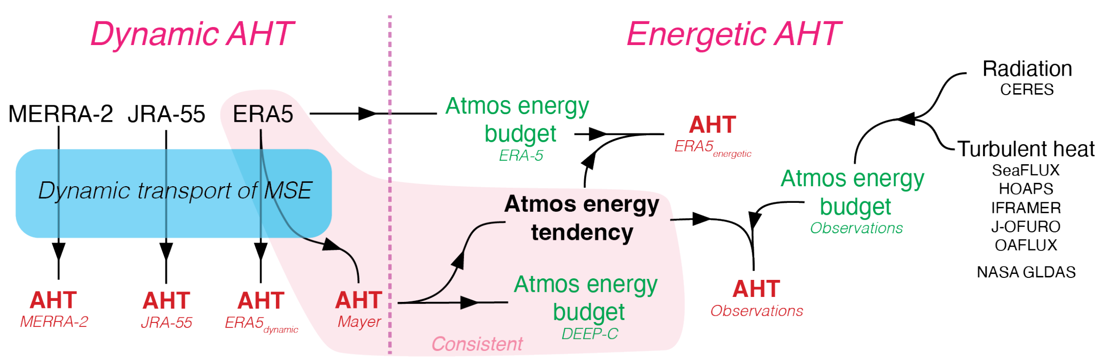

Figure 3.2: Schematic of all datasets and techniques to derive AHT. On the left side is a representation of the dynamic AHT calculation utilizing Eq. 3.1 and the right side represents the energetic AHT calculation using Eq. 3.2. The final AHT products are shown in red and the atmospheric energy budgets are shown in green. All data grouped in the pink region are consistent by construction.

3.3 Results

3.3.1 Observed Atmospheric Energy Budget

The zonal mean sensible and latent heat fluxes (along with the combined turbulent heat flux and Bowen ratio, defined as the ratio of sensible to latent heat flux) are presented in Figure 3.3 for the five observational products and ERA5 (for the annual mean and peak summer and winter months). Positive values are fluxes of energy into the atmosphere. The greatest disagreement between observation products is in the Southern Hemisphere midlatitudes (between 30°S and 65°S) where zonal means disagree by over 20 Wm^{-2}. There is closer agreement between the observational estimates of sensible heat flux in the tropics and Northern Hemisphere (northward of 30°S), being within 10 Wm^{-2} in the annual mean. The observation products share land surface flux calculations (from GLDAS) so latitudes with a greater proportion of land area (such as in the Northern Hemisphere) would be expected to have similar values by construction. ERA5 sensible heat flux is reasonably close to the observation estimates throughout the tropics but is considerably smaller in magnitude in the Northern Hemisphere midlatitude and polar regions (poleward of 40°N), being almost half that of the observational flux estimate. In the Southern Hemisphere midlatitudes (between 30°S and 65°S) ERA5 is within the range of the observation products. The monthly plots demonstrate that these differences are consistent throughout the year.

The zonal mean latent heat flux is positive across all latitudes and much larger in magnitude than the sensible heat flux, being up to 5 times greater in the tropics (Figure 3.3). Observational products of latent heating vary by up to 20 Wm^{-2}, a similar spread to the sensible heat flux. Importantly, observational latent heating estimates tend to be less than ERA5, especially in the tropics (<30°N/S) and this bias is consistent year-round. Equatorward of 30°N/S the Bowen ratio is low and comparable between the observations and ERA5. Poleward of 40°N the observational products have a Bowen ratio that is greater than that in ERA5. Observed Bowen ratios exceed unity poleward of 60°N indicating that the sensible heat flux becomes greater than the latent heat flux while the ERA5 Bowen

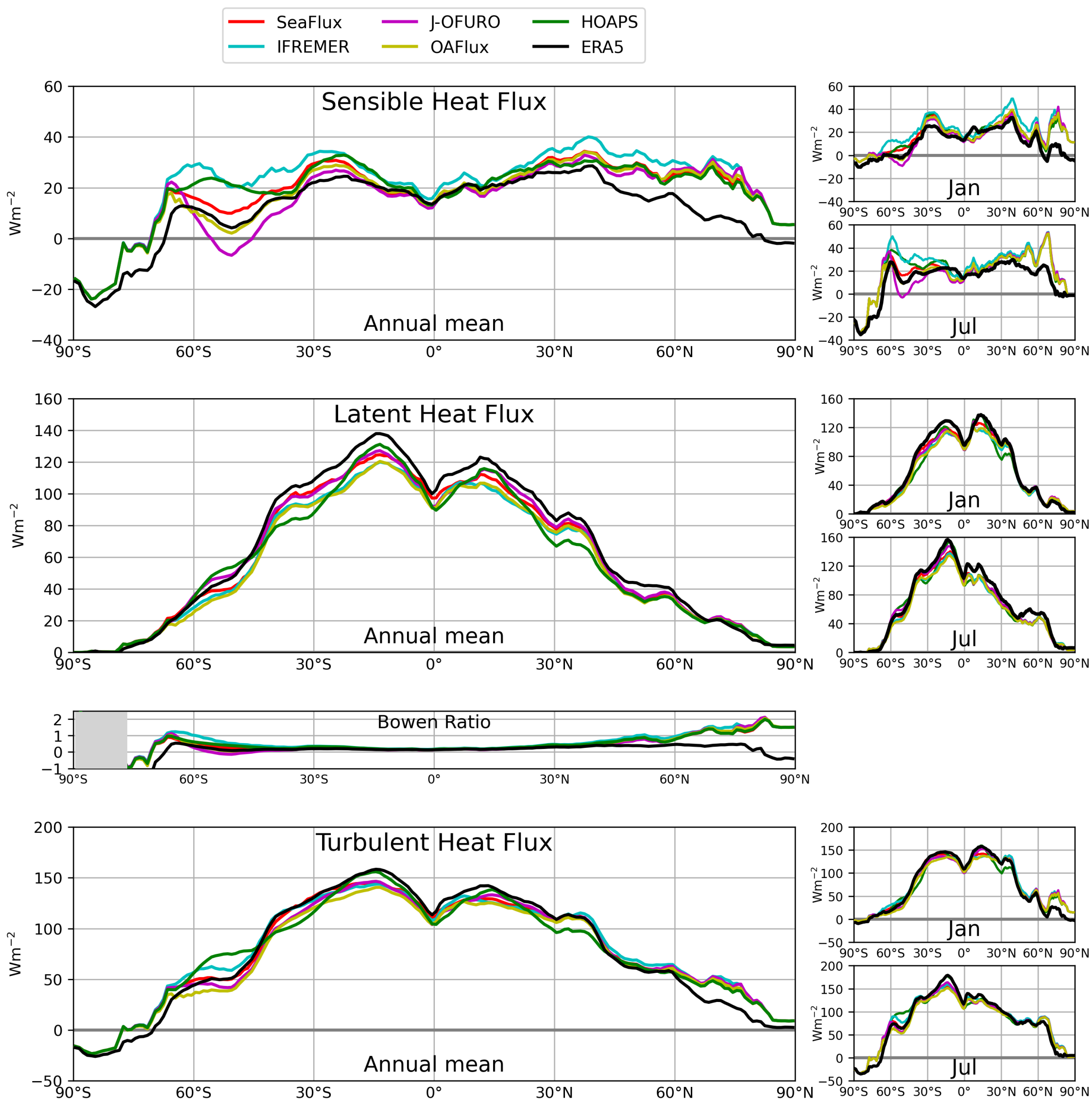

Figure 3.3: Annual mean sensible and latent heat fluxes, Bowen ratio, and the combined turbulent heat flux from observations and ERA5 (shown also for January and July monthly means), averaged between 2004 and 2014.

ratio remains within ±0.5 in the high latitudes.

Combining the sensible and latent heat fluxes together provides the full turbulent heat flux into the atmosphere (Figure 3.3). In the tropics, the observed turbulent fluxes tend to be lower than the ERA5 estimates (by up to 20 Wm^{-2}), attributable to the bias in the latent heating. In the midlatitude and polar regions the observed turbulent heat fluxes exceed ERA5 by up to 20 Wm^{-2} primarily from differences in the sensible heat flux. Thus, the observational products suggest a weaker equator-to-pole gradient of energy input to the atmosphere than that in ERA5. We explore the ramifications of this result for AHT later in this section.

The total atmospheric energy budget is the combination of the atmospheric radiative balance and the surface turbulent heat fluxes (Figure 3.4). Since the radiative budgets between CERES and ERA5 have close agreement (within ± 5 Wm^{-2} in the bias-corrected zonal mean; Supplementary Figure B.1), energy budget difference between the products largely represent differences in the turbulent flux products. The observations suggest less energy input to the tropical atmosphere and more energy input to the extratropical atmosphere compared to ERA5 (especially in the Northern Hemisphere). The DEEP-C data product is also plotted here as an estimate of the atmospheric energy balance that is consistent with reanalysis dynamic AHT. DEEP-C and ERA5 are in close agreement while the observations deviate from both by up over 20 Wm^{-2}. To calculate AHT, the atmospheric energy budget must be area weighted and have the mean removed to ensure closure of the energy transport, which is also shown in Figure 3.4. Removing the mean has a minimal impact on DEEP-C and ERA5 (demonstrating that they are close to closure), however, the observations have a considerable positive shift. This reduces the differences in the tropics; however, it introduces a larger bias in Northern Hemisphere polar region (poleward of 60°N). This bias persists through the year, demonstrating that the bias-corrected observed atmosphere energy budget is too positive relative to DEEP-C and ERA5 in the Northern Hemisphere polar regions.

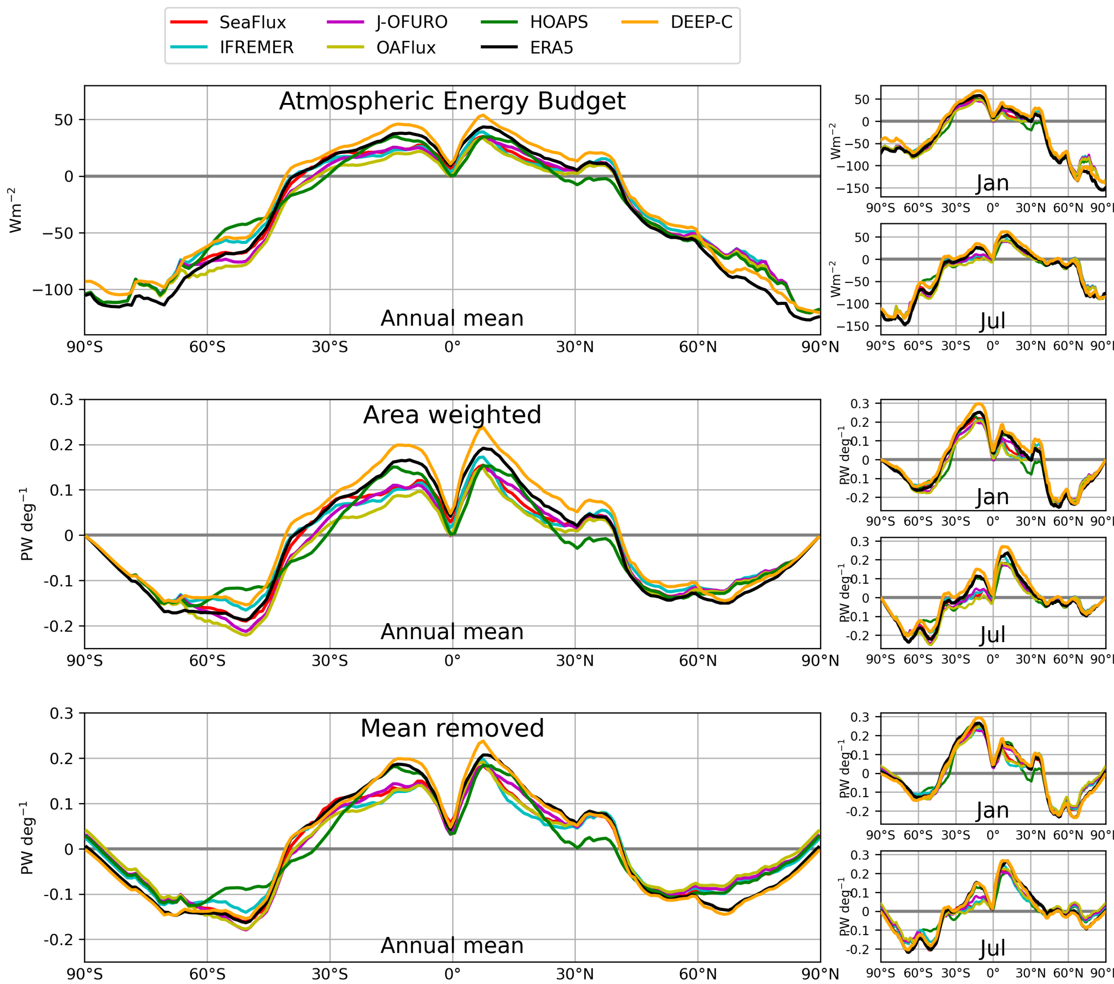

Figure 3.4: Annual zonal mean atmospheric energy budget from observations and ERA5 (shown also for January and July monthly means). The area weight atmosphere energy budget is shown along with the anomaly (mean removed) of the area weighted atmospheric energy budget.

3.3.2 AHT Climatology

The annual mean AHT derived from both the energetic and dynamic perspectives are shown in Figure 3.5 as calculated following Figure 3.2. The four dynamically calculated AHT from reanalysis are consistent with maximum poleward AHT at the same latitude and similar cross equatorial AHTs. The energetically derived AHT from ERA5 also resembles the dynamically calculated AHT (within 0.4 PW), demonstrating reasonable consistency between the dynamic and energetic components within ERA5, in the annual mean (consistent with Mayer et al. 2021). In the Southern Hemisphere most energetic calculations of AHT is within 1 PW of $\mathrm{ERA5}_{\mathrm{dynamic}}$, with the exception of HOAPS, which underestimates the magnitude of the poleward AHT by over 1 PW in the midlatitudes. In the Northern Hemisphere, all observational products significantly underestimate the reanalysis poleward AHT by over 1 PW (approximately 30% lower). There are also notable differences within the tropics, with OAFlux and J-OFURO having excessive southward energy flow across the equator, and HOAPS having no cross-equatorial energy flow. These differences are directly related to the difference in the bias-corrected atmospheric energy budget presented in Figure 3.4. The lower poleward AHT in the Northern Hemisphere is attributable to the reduced poleward gradient in atmospheric heating, through reduced energy gain in the tropics and a smaller deficit in the high latitudes in the observation-based budget.

These conclusions are insensitive to the choice of GLDAS version, that the zonal mean fluxes differences from varying GLDAS versions (varying the land surface turbulent heat fluxes) are far smaller than the difference between the observed and reanalysis energy budgets (Supplementary Figures B.1-B.5). Furthermore, even using the ERA5 land surface turbulent heat flux with the other observations does not improve the comparison, demonstrating the overwhelming bias the observed ocean fluxes have on the zonal mean compared to the reanalysis. While the use of ERA5 land turbulent heat flux improves the Northern Hemisphere midlatitudes, the underestimation of tropical latent heat flux (from over the ocean) remains the largest bias, which results in reduced annual mean AHT (as seen in Figure 3.5).

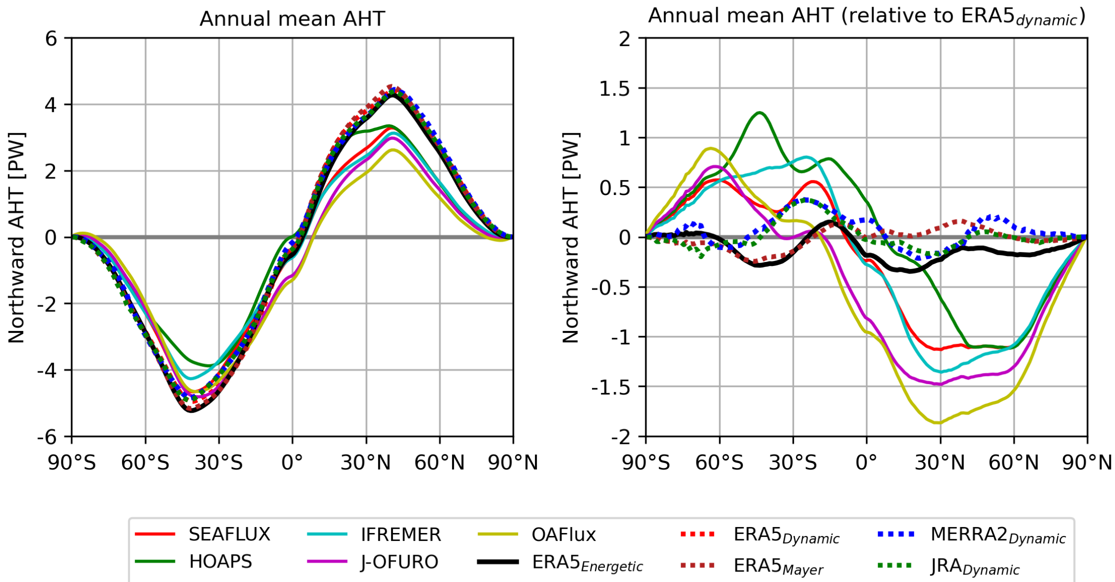

Figure 3.5: Annual zonal mean atmospheric energy budget from observations and ERA5 ((left) Annual mean northward AHT as calculated from reanalysis and the observation products through the dynamic (dotted lines) and energetic (solid lines) formulations. (right) The annual mean northward AHT relative to ERA5$_{\text{dynamic}}$

AHT has a distinct annual cycle and the representation of this cycle may be considered as important as the annual mean AHT as it represents the seasonally varying inputs of energy into the atmosphere. The full AHT seasonal cycle is shown for ERA5$_{\text{dynamic}}$, ERA5$_{\text{energetic}}$, SeaFlux, and OAFlux in Figure 3.6 along with the difference relative to ERA5$_{\text{dynamic}}$ (this plot is recreated for all AHT datasets in Supplementary Figures B.6, B.7, and B.8, however the main differences between reanalysis and observations hold true). The seasonal cycle is represented in both reanlaysis and observations however with differences in magnitude. The *energetic* AHT tend to underestimate the magnitude of *dynamic* AHT, especially in the Northern Hemisphere summer, with the observed AHT being >2 PW lower than ERA5$_{\text{dynamic}}$ in June and July, reducing to zero. The greatest difference between ERA5$_{\text{energetic}}$ and ERA5$_{\text{dynamic}}$ AHT (both of which are calculate entirely with data from the ERA5 reanalysis) also occurs in the Northern Hemisphere summer suggesting that either the energetic closure within the reanalysis is less constrained during these months. Alternatively, this difference may demonstrate that the assumptions made in the equations presented here are introducing errors, particularly in the summer (possibly through the treatment of enthalpy transport from moisture).

3.3.3 AHT Interannual Variance

Since AHT is a description of the general circulation of the atmosphere, interannual AHT variance must be consistent with variability in both the atmospheric energy budget and the dynamical movement of heat and moisture by weather systems (Armour et al., 2019). The monthly AHT anomaly time series is shown for 45°N, the equator, and 45°S for the observations and reanalysis with the mean and spread between derivations shown (Figure 3.7). There does appear to be very close agreement between the reanalysis and observations over this decade-long record, especially in the midlatitudes, where anomalous AHT is clearly captured by both records (varying by up to ±1 PW). At the equator there is less agreement in the anomalous AHT, especially early in the record (prior to 2008), where the observations anomaly can be of the opposite sign to the reanalysis.

The agreement between these time series can be further examined for each latitudinal band by plotting the correlation of each AHT product compared back to $\text{ERA5}_{\text{dynamic}}$ and SeaFlux (Figure 3.7). All AHT products have the same meridional structure in the correlation to $\text{ERA5}_{\text{dynamic}}$, maximizing in the midlatitudes with a minimum in the tropics (<10°N/S) and with very low correlations in the poles. The dynamic AHT products all have very high correlations to $\text{ERA5}_{\text{dynamic}}$, maximizing at 0.95 in the midlatitudes and reducing to between 0.6 and 0.8 in the equator. It is notable that $\text{ERA5}_{\text{Mayer}}$ has correlations as low as 0.8 to $\text{ERA5}_{\text{dynamic}}$, demonstrating the sensitivity of AHT to the manner of calculation even when using the same reanalysis. $\text{ERA5}_{\text{energetic}}$ correlates with $\text{ERA5}_{\text{dynamic}}$ to 0.8 in the midlatitudes and but these correlations drop to 0.5 in the tropics. The tropical minimum in AHT correlation, even between reanalysis dynamic AHT, may be attributed to the exclusion of the enthalpy flux associated with moisture transport in the AHT formulation (as described by Mayer et al. 2017), which likely has sizable

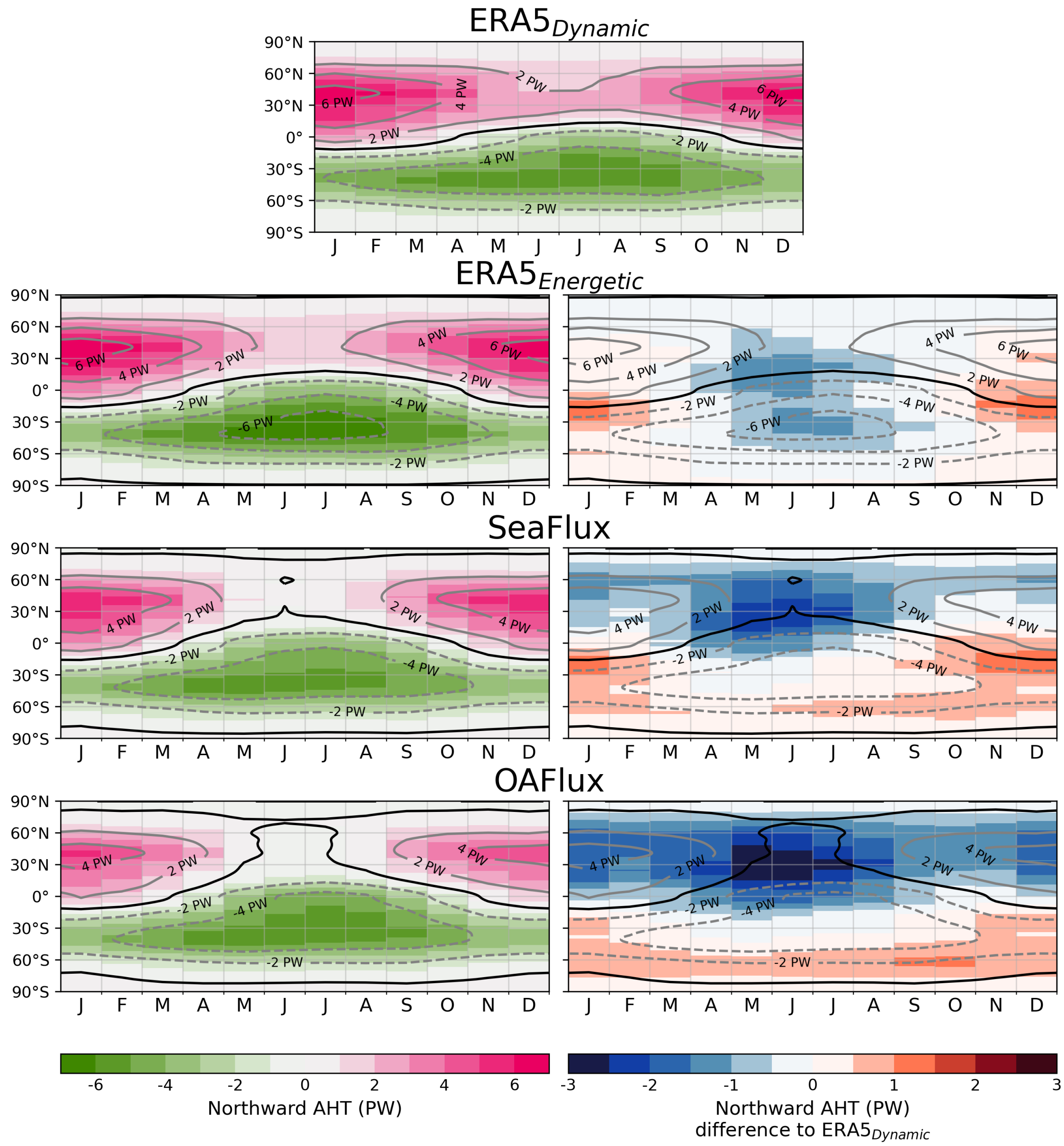

Figure 3.6: Seasonality of northward AHT in $\mathrm{ERA5_{dynamic}}$, $\mathrm{ERA5_{energetic}}$, SeaFlux, and OAFlux. The thick black contour represents zero AHT with gray contours at 2 PW intervals (dashed for negative). The difference relative to $\mathrm{ERA5_{dynamic}}$ is shown on the right in the shading.

variability in the tropics. Secondly, differences between reanalyses have also been noted with quantities such as near surface wind and moisture correlating poorly in the tropics on the monthly scale (Rienecker et al., 2011). Thermodynamic variables in particular (such as precipitation and OLR) have particularly low correlations, due in part to precipitation being an emergent property in reanalysis, not constrained to observations. These properties are crucial for defining tropical MSE and consequently heat transport, potentially contributing to the low AHT correlation in the tropics (tropical AHT is primarily accomplished through time-mean meridional Hadley Cell overturning; Armour et al. 2019). In the midlatitudes, reanalyses accurately capture the variables that define the large scale circulation and thermodynamics (such as geopotential height and temperature gradients) which would contribute to the high correlation between reanalysis AHT. The high temporal correlation in midlatitude AHT between reanalysis suggest that either the monthly mean circulation and MSE anomalies are similar between reanalysis or that the sub-monthly (synoptic timescale) covariances of v and MSE must be similar. Numerous studies (e.g. Rienecker et al. 2011 and Mayer et al. 2024) also demonstrates that reanalysis tend to be more similar to each other than to observational estimates (a result reproduced here), attributed to their shared construction.

Observed AHT products (SeaFlux, OAFlux, J-OFURO) have similar correlations to $\text{ERA5}_{\text{dynamic}}$, up to 0.8 in the midlatitudes, reducing to 0.3 in the tropics. When the correlation is taken with respect to SeaFlux the observation products have correlations of between 0.6 and 0.8 across most latitudes (<60°N/S). These observation products all utilize similar satellite retrievals to derive their surface fluxes. It is therefore expected that they will correlate with each other, even through their own biases and uncertainties. The reanalysis AHT correlations to SeaFlux also range between 0.6 and 0.8 in the midlatitudes but reduce to between 0 and 0.3 at the equator.

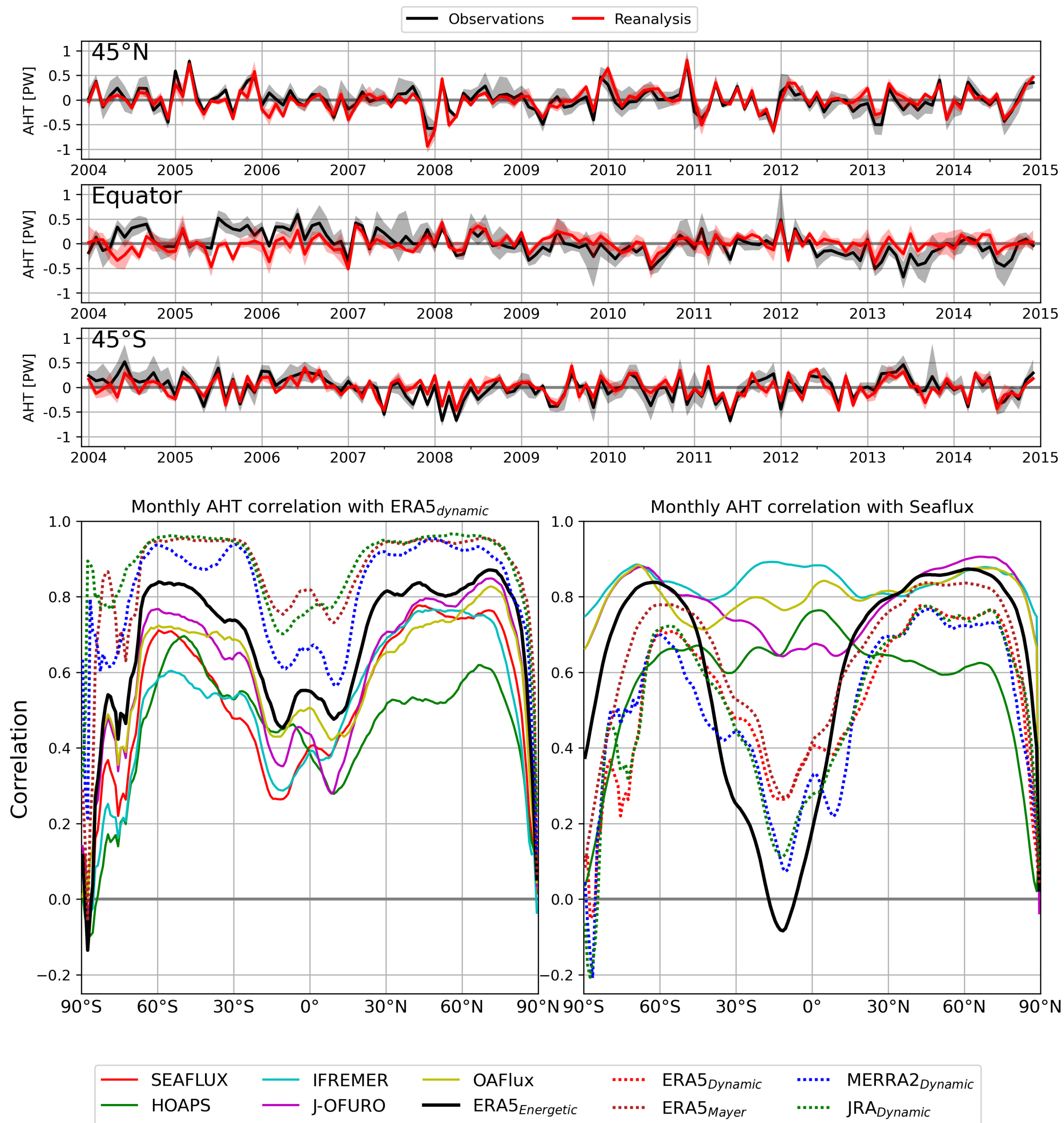

Figure 3.7: (upper) Time series of the mean and spread of the monthly AHT anomaly at 45°N, Equator, and 45°S from the observations (black; including the five ocean flux products, combined with GLDAS and CERES) and reanalysis (red; including the five reanalysis products). (lower) Correlation of monthly AHT anomaly for each latitude band with respect to (left) ERA5$_{\mathrm{dynamic}}$ and (right) SeaFlux.

3.4 Summary and Discussion

The presented results represent an effort to develop an observational record of monthly AHT from the *energetic* perspective utilizing state-of-the-art datasets. We set out to challenge the opinion that observations of Earth's atmospheric energy balance are inadequate to calculate Earth's AHT. Ongoing advancements in observations of Earth's surface energy balance over recent decades (from both surface and spaceborne platforms) have facilitated the development of global surface flux products from numerous international institutes. Here, these products are paired with other energy balance observations (such as TOA and surface radiative fluxes) in an attempt to derive an observational-based record of monthly AHT. This study essentially examines the level of agreement between the poleward flow of moist static energy (MSE) within reanalysis and the observation of Earth's energetic fluxes.

The majority of the observation-based AHT have close agreement with reanalysis products in the Southern Hemisphere in the annual mean (within 0.5 PW, comparable to the difference between reanalysis products) while substantially underestimating the Northern Hemisphere annual mean reanalysis AHT (by over 1.5 PW). Since we are comparing to reanalyses it is not correct to consider them as resolving the true AHT, however, there are some physical constraints of the climate system that may aid in judging the true accuracy of these results. The location of the intertropical convergence zone (ITCZ), associated with the ascending branch of the Hadley cell, represents the location of diverging energy transport toward the opposing poles (Kang et al., 2008, 2009; Frierson and Hwang, 2012). The annual mean ITCZ is located north of the equator due to a hemispheric asymmetry in the atmospheric energy budget (increased energy input into the Northern Hemisphere) that must be balanced by energy being transported across the equator into the hemisphere with less atmospheric energy input (the Southern Hemisphere; Seo et al. 2014; Donohoe et al. 2013). Donohoe et al. (2014) also demonstrate that the variance in the location of the ITCZ is very closely connected to the magnitude of AHT across the equator. All but one of the AHT products presented have an annual mean southward AHT across the equator. HOAPS however, has a cross equatorial AHT of roughly zero, which would imply that the annual mean ITCZ location is situated on the equator, which we know to be untrue. Two other products, OAFLUX and J-OFURO have greater cross-equatorial flow than the reanalysis products (over twice as large), which would imply that either the ITCZ is much further north than as represented by the reanalysis (which do correctly represent the ITCZ location; Donohoe et al. 2014) or that the tropical atmospheric overturning is of a greater magnitude. SeaFlux and IFREMER have comparable cross equatorial AHT to the reanalysis implying that derived *energetic* AHT from these products do correctly capture the ITCZ location and atmospheric overturning. Constraining modeled and observed AHT by the ability to correctly locate the ITCZ may be one independent way of assessing their accuracy.

The underestimation of observed Northern Hemisphere annual mean AHT compared to reanalysis is a feature consist in all observation products presented here. This bias can be directly attributed to differences in the representation of the zonal mean turbulent heat fluxes, specifically the reduced poleward gradient of the turbulent heat fluxes. In the tropics, the observed turbulent heat fluxes are less than reanalysis (due to smaller latent heat fluxes) while in the Northern Hemisphere high latitudes, the observed turbulent heat fluxes exceed reanalysis (due to bias in both sensible and latent heat flux). The net result is a shallower gradient in atmospheric heating, than compared to reanalyses, which would result in a lower AHT. It is clear that these observation products have far less evaporation in the tropics than reanalysis suggests. The greater proportion of land in the Northern Hemisphere appears to contribute to the lower atmospheric heating gradient, with GLDAS tending to exceed ERA5 atmospheric heating over land in the mid- to high latitudes (Supplementary Figure B.5). There is also a temporal variability in this AHT difference (Figure 3.6) demonstrating that the Northern Hemisphere summer is when the difference between reanalysis and observation atmospheric energy budget are greatest. It would be worthwhile for future energy balance studies to examine the seasonal accuracy of surface turbulent heat fluxes, especially during the Northern Hemisphere summer.

A central motivation for this research is the disagreement in historical AHT trends between reanalysis and models (see Cox et al. 2024a). We have presented an additional measure of AHT based on the energetic closure of the atmosphere with varying levels of agreement in the annual mean, climatology, and interannual variance. These supplementary datasets will allow for additional research questions on the trends, drivers, and consequences of AHT variability in the observed period. Figure 3.8 provides an exploratory look at AHT anomalies (as shown in Figure 3.7) for each latitudinal band. It is apparent that both SeaFlux and OAFLUX have anomalous northward AHT early in the period inconsistent with reanalysis, which would be associated with increased atmospheric heating gradients towards the Southern Hemisphere. In contrast, the $\text{ERA5}_{\text{dynamic}}$ variance appears to have stationarity, being the most temporally homogeneous estimate of AHT anomalies in this decade-long period. There are periods of agreement in the anomalies in Figure 3.8, the end of 2014 for example has anomalous northward AHT and the beginning of 2009 has anomalous southward AHT in the Northern Hemisphere consistent across all products. Identifying the source of these atmospheric heating anomalies would allow for a description of the sources of discrepancy, identifying when the flux anomalies (from both the surface and TOA) align or are contrary to the dynamic movement of MSE within reanalysis.

The presented observed AHT only spans a decade, a short period even for observed climate records. The ever-growing network of Earth observing satellites and the integration of emerging technologies may provide increased accuracy in recording Earth's surface fluxes. The quality of the observation-based products is highly dependent on the quality of the observing sensors (along with assimilation techniques and parameterization; Robertson et al. 2020). The increasing agreement between estimates in Figure 3.8 may be associated with the deployment of newer satellites with sensors of increased accuracy through time. It would be worth examining the role individual satellite products have on increasing the level of agreement between observation products and with reanalysis.

It is important to emphasize that the presented observed AHT is not entirely indepen-

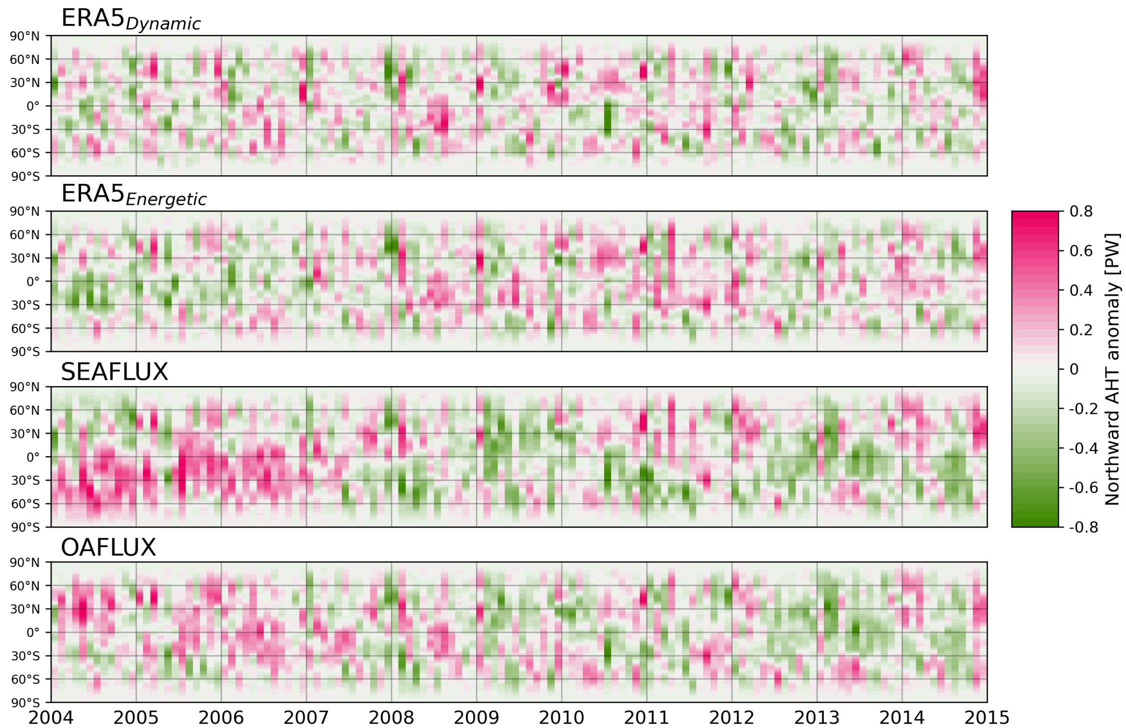

Figure 3.8: Latitude-time series of zonal mean AHT anomalies (seasonality removed) for ERA5$_{\text{dynamic}}$, ERA5$_{\text{Energetic}}$, SeaFlux, and OAFLUX.

dent from the reanalysis. Firstly, because many of the observed data products are based on the same satellite retrievals that are also assimilated into reanalysis (Hersbach et al., 2018; Tomita et al., 2019). Secondly, and more explicitly, because the atmospheric tendency used to derive the observed AHT throughout is derived from ERA5. The atmospheric energy tendency along with the MSE is unable to be observed. Even when we consider the suite of vertical sounders and atmospheric profilers onboard Earth observing satellites, these only provide a small fraction of global, vertically resolved quantities through the atmosphere. Cloud covered regions are unable to be sampled by many sounders (certainly infrared-based sounders) resulting in substantial undersampling. Here, we have utilized the Mayer et al. (2017) ERA5 mass-consistent tendency in all energetic AHT calculations (Eq. 3.4). To test the sensitivity of energetic AHT calculations to the tendency, we used an independent calculation following Donohoe et al. (2020), also using ERA5 data

(Supplementary Figure B.9). The difference between these tendency calculations is that Mayer et al. (2017) utilizes a time variant surface pressure in the integral bounds while also considering a term for kinetic energy and assuming that the sensible heat from vapor is negligible. Both tendencies provide AHT calculations in close agreement with similar correlations between the energetic AHT and $\mathrm{ERA5}_{\mathrm{dynamic}}$ (r within 0.12; Supplementary Figure B.10). Future research should further examine the role the atmospheric tendency has on controlling AHT and explore independent measures of the tendency, including from observations.

The method presented here builds on a number of other contemporary studies examining Earth's flow of energy. Liu et al. (2017) and Mayer et al. (2024) both provide evaluations of observed surface budgets, demonstrating the spread between observations and difference to reanalysis with conclusions in agreement with the results presented herein. One important advancement we demonstrate is to consider the global effect of zonal mean biases in the observed surface flux products by considering the derived AHT. By calculating the AHT from these surface products, it allows for a direct comparison to numerous other characteristics of the climate system (such as the dynamic motion of MSE). Considering the two simultaneous roles of AHT (*dynamic* and *energetic*) allows for a unique perspective, as anomalous AHT must be consistent with anomalies in both the flow of MSE and the energetic fluxes of the atmosphere. This conceptualization facilitates a holistic view of interannual variances in the atmospheric general circulation.

We set out to challenge the assumption that global surface flux observations are not suitable to calculation AHT. The results demonstrate that there are indeed large differences between reanalysis and observation-based AHT estimates in both the annual mean and seasonal cycle, with the greatest differences in the Northern Hemisphere. The temporal variability demonstrates good agreement between estimates in the midlatitudes (with correlations reaching 0.8), however, nonstationarity in the observation-based time series appears to disagree with the reanalysis AHT time series. These conclusions support the perspective that the surface energy budget remains the most uncertain component of the atmospheric energy budget (in agreement with Robertson et al. 2020). Improving our ability to observe the surface energy budget should remain a priority for the Earth observation community.

Chapter 4

The Energetic Expression of Monthly Atmospheric Heat Transport Variability

4.1 Introduction

The previous chapter presented an effort to develop an observational-based record of Earth's AHT. While there were distinct mean state differences between atmospheric heat transport (AHT) estimates, the monthly variability has close agreement, with correlations between 0.5 and 0.8 in the midlatitudes between satellite- and reanalysis-based calculations. Such agreement demonstrates that the monthly variability of meridional gradients of the atmospheric energy budget (in the midlatitudes) is consistent with the monthly variability of MSE transport through atmospheric dynamics. This statement identifies the atmospheric processes that lead to agreement between dynamic and energetic AHT variance. A number of questions remain to fully characterize this relationship and develop an understanding of the energetic exchanges consistent with AHT variance.

- What is the monthly variability of historical AHT?
- What are energetic properties consistent with monthly AHT variability?
- How do the atmospheric energy balance components contribute to monthly AHT variability?

These research questions underpin the analysis presented in this chapter. It is important to state that this research will not be identifying the causality or directionality of AHT variance between dynamic and energetic perspectives and will hence be describing the consistency between the variances. To attribute causality of AHT variance requires a different research framework than is presented herein, and certainly remains as an important, underexamined research topic.

The flow of energy through the atmosphere has long been used to describe the mean-state properties and long-term trends associated with Earth's climate. Stone (1978) demonstrates that the magnitude of the total, annual-mean meridional heat transport (MHT) is defined solely by the Earth-sun geometry. The amount of energy that flows poleward on a spherical planet is described by the variable incident solar flux at the top of Earth's atmosphere. Bjerknes (1964) provides additional context, reasoning that if the top-of-atmosphere (TOA) energy receipt remains constant, the total amount of heat flowing poleward, the sum of the atmospheric and oceanic components, must also be constant. Should the energy transport of either component vary significantly, the other must compensate, a processes that has become known as Bjerknes compensation (Shaffrey and Sutton, 2006). Clearly, the amount of energy exchanged between the atmosphere and ocean, and the meridional gradient in this exchange, is crucial for enforcing AHT variability.

The long term variability of AHT has been linked to numerous expressions of the climate system including the location of the ITCZ (Kang et al., 2008; Donohoe et al., 2014), polar amplification (Hwang et al., 2011; Merlis and Henry, 2018; Hahn et al., 2021), the frequency of deep convection (Riehl and Malkus, 1958; Stephens et al., 2024), the efficiency and location of midlatitude cyclones (Shaw et al., 2018; Armour et al., 2019), and the distribution of precipitation (Held and Soden, 2006). Short term AHT variability has also been examined as a driver of impactful synoptic scale weather, describing heatwaves and moisture transport (through MSE transport and convergence) in midlatitude (Messori and Czaja, 2011; Cox et al., 2024b) and polar regions (Messori and Czaja, 2015; Woods and Caballero, 2016; Blanchard-Wrigglesworth et al., 2023).

While anomalous synoptic-scale weather can be described through AHT variability (specifically through the convergence of MSE), these extremes from baroclinic systems (on the scale of 2-6 days) are not associated with the integrated hemispheric-scale AHT variability. Through frequency analysis, Messori and Czaja (2014) demonstrates that it is rather the large scale phase alignment between meridional velocity and MSE anomalies along a zonal band, which occur on the order of 30 days that contributes to integrated AHT variability. It is the variability of planetary scale motions (wavenumber <4), which manifest as stationary eddies in the monthly mean state, that contribute most to AHT variability (Messori and Czaja, 2014). This finding is recreated here by regressing the dynamic AHT components onto the standardized AHT anomaly, using three individual reanalysis spanning 40 years (Figure 4.1). Within the tropics the vast majority of AHT variability is accounted for by the mean-meridional circulation (from Hadley Cell overturning). In the Northern Hemisphere extratropics, the stationary eddies are by far the leading component responsible for the total AHT variance. Transient eddies (such as those associated with baroclinic development) have very little contribution to Northern Hemisphere AHT variability beyond 40°N. In the Southern Hemisphere midlatitudes (30-50°S) however, transient eddies do account for the majority of a monthly AHT anomaly suggesting a hemispheric asymmetry in the the dynamic forcing behind monthly AHT variability. This asymmetry is likely related to the dominate stationary eddies present in the Northern Hemisphere in contrast to the high-frequency synoptic waves dominant in the Southern Hemisphere (Lorenz and Hartmann, 2003; Trenberth and Stepaniak, 2003; Cox et al., 2022).

The contrast between local-scale impacts versus the integrated net result, as demonstrated through the dynamic AHT, provides a suitable parallel to begin assessing the

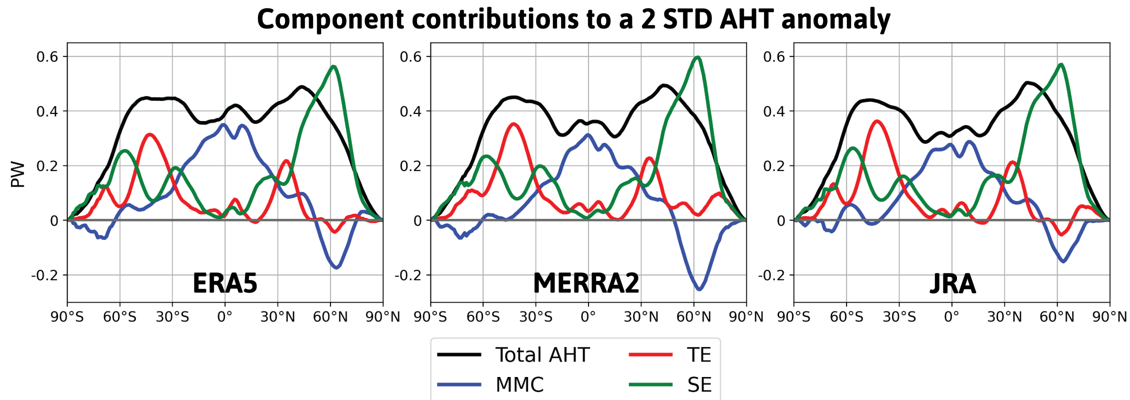

Figure 4.1: The regression coefficients of the dynamic AHT components; the mean meridional circulation (MMC), transient eddies (TE) and stationary eddies (SE) regressed onto the standardized monthly AHT for ERA5, MERRA2, and JRA. Coefficients are multiplied by 2 to be representative of an extreme (2 standard deviation) AHT anomaly at each latitude.

variance of energetic AHT. The mean state energetic AHT is defined as the divergence of the atmospheric energy budget (AEB).

$$\text{AHT} = 2\pi a^2 \int_{-90}^{\phi} \cos(\phi)\,(Q_{RAD} + \text{SH} + \text{LH} - \text{AET})\,d\phi \tag{4.1}$$

Numerous studies have utilized this energetic perspective, accounting for the energy exchange to calculate the meridional flow of energy in the atmosphere (Trenberth and Solomon, 1994; Mayer et al., 2017; Armour et al., 2019). Fajber et al. (2023) provides a novel insight by demonstrating that the total energetic AHT, can be decomposed into the *implied* AHT from each individual component,

$$\text{AHT}_{\text{Implied}} = 2\pi a^2 \int_{-90}^{\phi} \cos(\phi)\,(X)\,d\phi \tag{4.2}$$

where X can be equal to Q_{RAD}, SH, LH, or $-$AET. By construction, the sum of all the implied transports will equal the total AHT. Through this component breakdown, Fajber et al. (2023) is able to demonstrate that the total AHT is primarily governed by the poleward gradient of evaporation. The release of latent heat through evaporation is the greatest addition of energy into the atmosphere, reducing substantially towards the poles, enforcing a large meridional gradient in atmospheric heating (Figure 4.2). The evaporation and subsequent condensation increases the energy budget through both the increase of water vapor and the subsequent release of energy warming the dry air (Fajber et al., 2023). This physical mechanism describes a transfer of energy, gaining energy through condensation, but once released, that energy can now be lost through a variety of energetic processes (such as radiative cooling or the sensible heat flux).

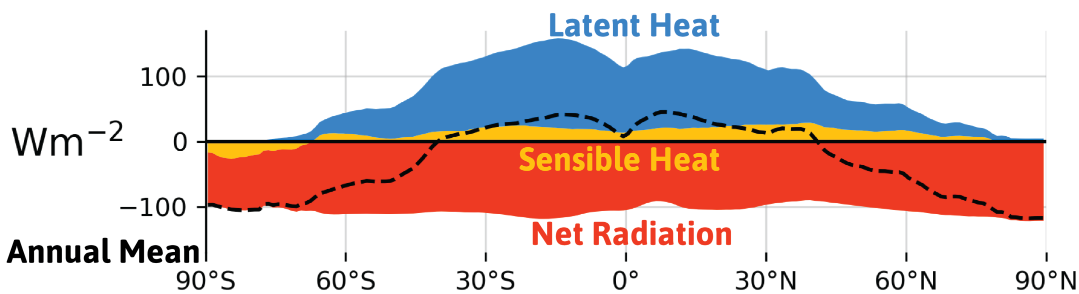

Figure 4.2: The annual mean atmospheric energy budget decomposed into latent (blue) and sensible (yellow) heat fluxes and the net radiation (red) as calculated from 40 years of monthly ERA5 data. The net energy budget is shown in the dashed blacked line. The AET reduces to zero in the annual mean.

Fajber et al. (2023) tested the sensitivity of this importance on latent heating for AHT through a number of perturbation experiments by changing the distributions of land and oceans, enforcing lower evaporation (such as through an ice covered ocean) and increasing global CO_2 concentrations. Through all experiments, changes in the meridional gradient in evaporation was the leading cause of AHT variability. While these experiments are considered to be “Earth-like”, they are not representative of the current or historical variability in the atmospheric energy budget. These experiments imposed outside forcing on the climate system, dramatically changing the Earth system. It is appropriate to question whether this dependence on latent heating applies to less dramatic forcing on the AEB, such as the variability of energy receipt on monthly timescales. Addressing this question is the primary objective of this study. The following section describes the data utilized in this study, drawing on both reanalysis and observations to facilitate robust conclusions. An assessment of the monthly variability will be presented, examining the zonal extent of anomalous transport within a given month. The covariance of the energy budget components with monthly AHT forms the bulk of this analysis in order to answer the research objective.

4.2 Methodology

The historical record of monthly AHT forms the basis of this analysis. Dynamic AHT is calculated from 3 reanalysis: ERA5 (Hersbach et al., 2018), MERRA2 (Gelaro et al., 2017), and JRA-55 (Kobayashi et al., 2015) over a 42-year period (1980-2021) following Cox et al. (2024a):

$$\mathrm{AHT}(\phi) = \frac{2\pi a\cos(\phi)}{g}\int_0^{\overline{P_s}} \left(\underbrace{[\bar{v}]^{\dagger}[\mathrm{MSE}]^{\dagger}}_{\text{MOC}} + \underbrace{[v^{*}\mathrm{MSE}^{*}]}_{\text{SE}} + \underbrace{\overline{[v^{*\prime}\mathrm{MSE}^{*\prime}]} + \overline{[v]^{\prime}[\mathrm{MSE}]^{\prime}}}_{\text{Transient eddies}} \right) dp \quad (4.3)$$

where v is the meridional wind, p is pressure ($\overline{P_s}$ is the climatological surface pressure), a is the radius of earth, square brackets [] denote zonal averages, overbars ($\overline{X}$) denote time means, asterisks (*) denote departures from the zonal average, and primes ($'$) denote departures from the time average. Daggers (†) represent departures from the vertical average in order to maintain mass conservation in the MOC (Cox et al., 2024a). AHT in this perspective may be characterized into contributions from meridional overturning circulation (MOC), stationary eddies (SE), and transient eddies (TE). This formulation is commonly calculated from models and reanalysis instantaneous data at high temporal (e.g. 6 hourly), spatial (<1°), and vertical (>40 levels) resolutions (Donohoe et al., 2020). Additionally, an independent calculation of mass-consistent AHT as calculated by Mayer et al. (2017, 2022a) from ERA5 is also used for further validation ($\mathrm{ERA5}_{\mathrm{Mayer}}$). The Mayer et al. (2017) AHT explicitly closes the atmospheric mass and energy budget at every timestep with a number of additional details such as considering kinetic energy and variable surface pressure.

Energetic AHT will be calculated following Eq. 4.1 from ERA5 and from a range of observation-based datasets, following Prince et al. (2025). The observational datasets utilize surface and TOA radiative fluxes from the NASA Clouds and Earth's radiant Energy System (CERES-EBAF Loeb et al. 2018). Four observation-based ocean surface turbulent heat flux products are utilized: the NASA SeaFlux version 3 dataset (Roberts et al., 2020), the Woods Hole Oceanographic Institution (WHOI) Objectively Analyzed Air Sea Fluxes for the Global Oceans (OAFlux) version 3 dataset (Yu et al., 2008), the Japanese Ocean Flux Data Set with Use of Remote Sensing Observations (J-OFURO) version 3 dataset (Tomita et al., 2019),and the French Research Institute for Exploitation of the Sea (IFREMER) version 4 dataset (Bentamy et al., 2013). The NASA Global Land Data Assimilation System version 2.2 is used for the land surface turbulent heat fluxes (GLDAS; Rodell et al. 2004; Beaudoing and Rodell 2020). To complete the energy budget, the same AET is utilized for all energetic AHT calculation throughout this analysis, calculated from ERA5 by Mayer et al. (2022a).

Examining long-term energy budget records from reanalysis data is a perilous endeavor. The lack of energy and mass closure requirements of reanalysis paired with the variable (generally increased) availability of observing systems recording the climate both contribute to uncertainty in long-term records. Indeed, Mayer et al. (2021) demonstrates that the surface flux of ERA5, and consequently the atmospheric energy budget, experiences a gradual positive drift between 1996 and 2004. This drift is attributed to erroneously increasing latent heat fluxes over land. Further analysis from Robertson et al. (2020) found these positive trends in the latent heat flux to be misleading. Through a reduced observation reanalysis test, the uncertainties in reanalysis are attributed to direct errors in satellite wind speed retrievals (from the Special Sensor Microwave Imager/Sounder; SSMI/S), sea surface temperature (from the Advanced Very High Resolution Radiometer; AVHRR), and near surface humidity errors, paired with reduced coverage prior to the year 2000 (Robertson et al., 2020).

Example time series of reanalysis derived AHT as calculated from energetic (Eq. 4.1) and dynamic (Eq. 4.3) methods is presented in Figure 4.3. Indeed, substantial drift between 1994 and 2004, especially in the $ERA5_{energetic}$ (which is largely absent from other reanalyses). Notably, the difference between ERA5 dynamic and energetic AHT calculations reduces by about half following 2004 demonstrating increasing closure within the reanalysis. Not only does the mean drift over time, but the tropical AHT seasonality exhibits nonstationarity, especially in MERRA2 (Figure 4.4). In the first decade (1980-1989) MERRA2 has reduced seasonality in cross-equatorial AHT and between 2000-2010, has an enhanced seasonal cycle. The seasonality of the other reanalysis derived AHT tend to be more stationary with any differences between decades being similar across products.

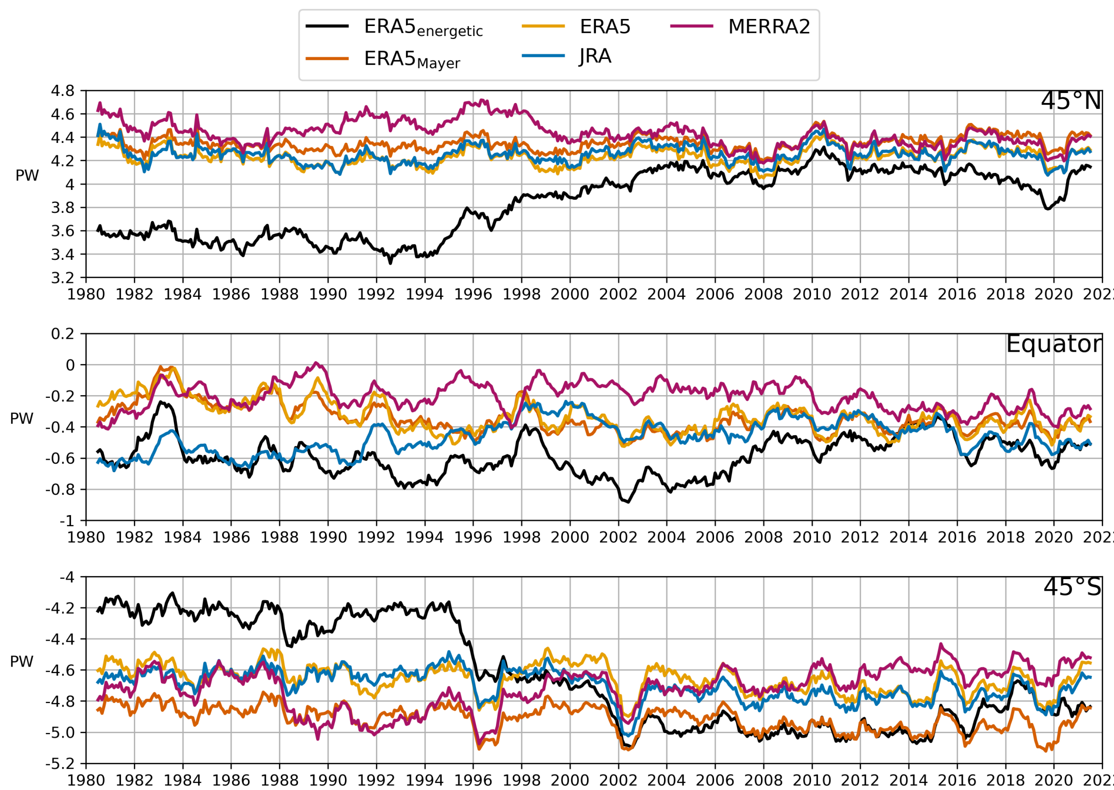

Figure 4.3: Time series of reanalysis calculated AHT at 45°N, the equator and 45°S as calculated from the dynamic (from ERA5, MERRA2, and JRA) and energetic (from ERA5) methods with a 12-month running mean.

The anomalous drift and non-stationarity of this data would impede identification of the drivers of monthly variability. If a simple anomaly was taken and the full seasonal

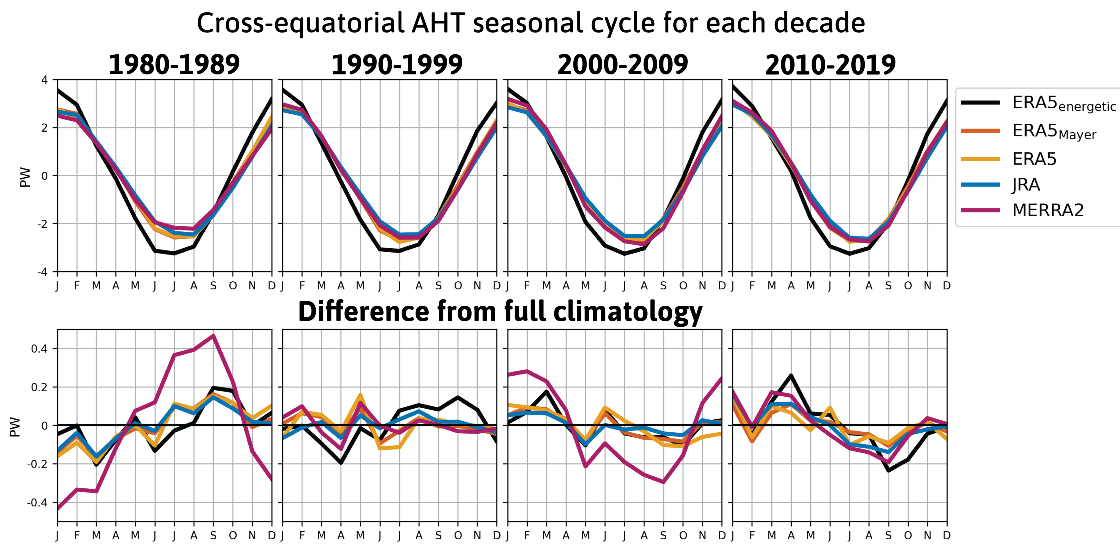

Figure 4.4: (upper) The seasonal cycle of cross-equatorial AHT for each decade between 1980 and 2020 for dynamic and energetic AHT calculated from reanalysis. (lower) The difference between seasonal cycles as calculated from each decade and full climatology.

cycle removed, these features would appear to be large differences in the monthly AHT between products. Furthermore, Prince et al. (2025) demonstrates that observation-derived energetic AHT has non-stationarities, which disagree with dynamic AHT (shown in the previous chapter). Here, a Seasonal-Trend decomposition using LOESS (locally estimated scatterplot smooth; STL) is used to extract the monthly anomalies from these complex nonstationary data (Cleveland et al., 1990). STL is a filtering process that decomposes a time series into the seasonal cycle, the long term trend, and residual. The STL trend identification is effectively a low-pass filter that is subtracted from the original data to produce stationary anomalies. If there are no trends (or drift) in the data, then this trend identification essentially subtracts the mean of the dataset, producing an anomaly dataset. The STL seasonal decomposition removes the time varying seasonal cycle from the data. A parameter is specified to adjust how quickly the seasonal cycle can change and care must be taken not to overfit the seasonal cycle to interannual AHT variability. Figure 4.4 demonstrates that the anomalous seasonal cycle appears to vary on the order of decades. Once these two features have been decomposed, the remaining data represents the monthly anomalies. To reiterate, if the data has no trend or low frequency variability, and the seasonal cycle is stationary, then the residual from STL decomposition is identical to a simple climatological anomaly (subtracting the seasonal cycle).

There are three main parameters to adjust for STL decomposition: (n_p) the number of observations within each cycle, (n_t) the smoothing parameter of the trend, and (n_s) the seasonal smoothing parameter. Here the seasonal cycle (n_p) is well defined as the 12 months within a year and the trend smoothing (n_t) is set to smooth at decadal scales. The seasonal smoothing parameter (n_s; the number of seasonal cycles within the smoothing window) is less intuitive and thus a sensitivity test is undertaken to decide an appropriate value. Figure 4.5 demonstrates the sensitivity of the cross-equatorial AHT STL residual with four different smoothing parameters. The residuals are minimized for the smaller smoothing parameter ($n_s = 3$) demonstrating that the seasonal cycle is being overfitted, so that interannual variances are being captured as a rapidly changing seasonal cycle. The decomposition is essentially calculating a new seasonal cycle for each year and removing this from the data. The largest smoothing parameter ($n_s = 25$) maximizes the variance of the residuals but contains some non-stationarity identified in the original data, a sign that the seasonal cycle is becoming less variable (and more similar to the full mean climatology). A smoothing parameter of $n_s = 13$ was chosen as a value that maximizes the interannual variance while reducing the non-stationarity in the residuals.

An example of the full STL decomposition is presented in Figure 4.6 for 45°N, demonstrating the low-pass filter, the gradually varying seasonality and the residual - the monthly AHT anomalies. This decomposition is applied to all datasets used herein, both reanalysis and observational. Figure 4.7 recreates the monthly correlation presented in the previous chapter (based on the decade long AHT record), however, with STL decomposition. The correlations with $\text{ERA5}_{\text{dynamic}}$ are largely the same as presented in Prince et al. (2025), with a small increase in the correlation with the observation-based AHT. The correlation of all AHT products with SeaFlux has increased following STL decomposition, demonstrating that there were indeed nonstationarities that were modulating the observation

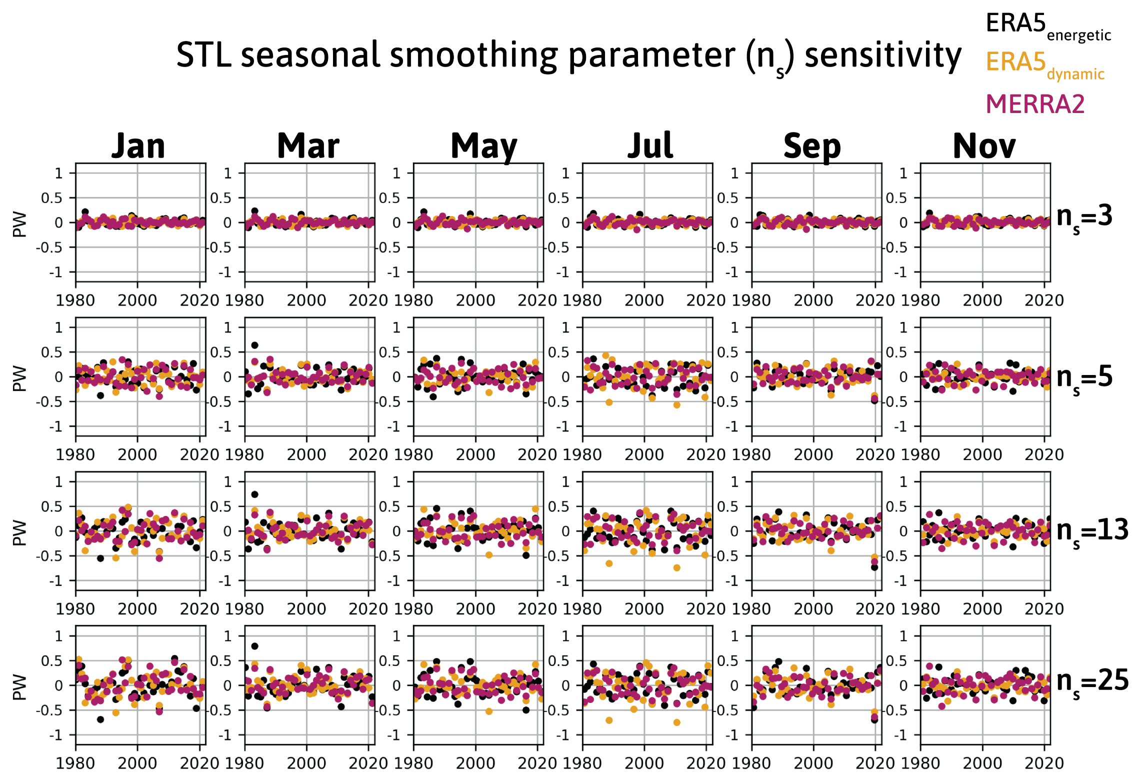

Figure 4.5: Sensitivity test of the STL seasonal smoothing parameter, shown for three reanalysis AHT products ($\mathrm{ERA5}_{\mathrm{energetic}}$,$\mathrm{ERA5}_{\mathrm{dynamic}}$, and MERRA2). Time series of residuals from individual months are shown for 4 different seasonal smoothing parameters.

AHT that differed from the dynamic AHT. The final monthly anomaly dataset is now suitable to examine the relationship between the atmospheric energy budget and AHT variance.

4.3 Results

4.3.1 AHT monthly variability

The standard deviation of monthly AHT is presented in Figure 4.8 to provide context before examining the AHT covariance. Over the 42-year record all reanalysis AHT have similar monthly AHT standard deviations, maximizing in the winter hemisphere with minimums in the summer. Northern Hemisphere AHT has a greater wintertime standard

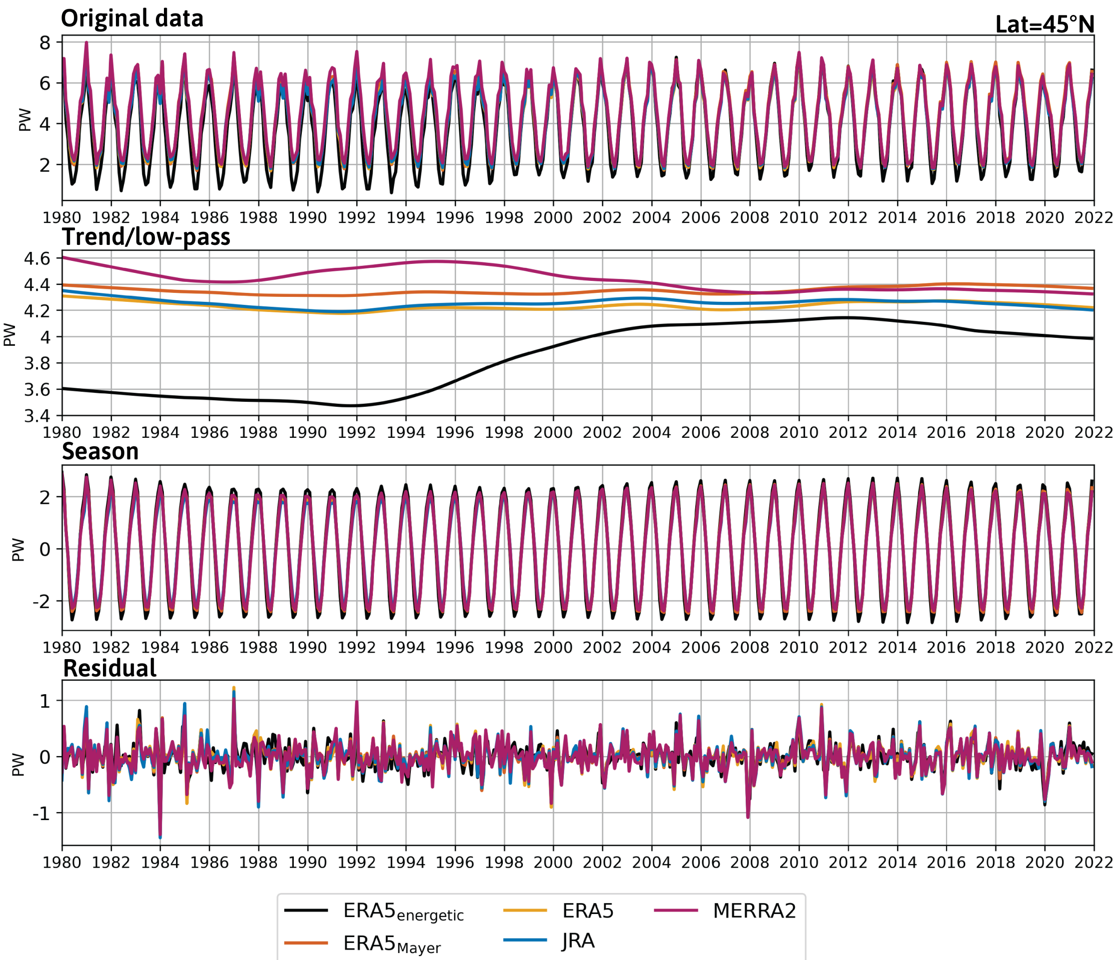

Figure 4.6: Example of the full STL decomposition for reanalysis derived AHT at 45°N.

deviation with a maximum in January exceeding 0.4 PW. Notable the minimum standard deviation in the midlatitudes is the same as the tropical AHT standard deviation - the variance of midlatitude summertime AHT is the same as the variance experienced in the tropics (approximately 0.1 PW). The 10-year calculated standard deviation is similar to the 42-year record, however, the Northern Hemisphere maximum occurs in December rather than January. The energetic AHT calculations have very similar standard deviations to the dynamic AHT, with OAFLUX and J-OFURO having remakably similar seasonal cycles and magnitude. Both SeaFlux and IFREMER tend to have greater standard deviations over the full year at all latitudes. Importantly, the differences between AHT variance

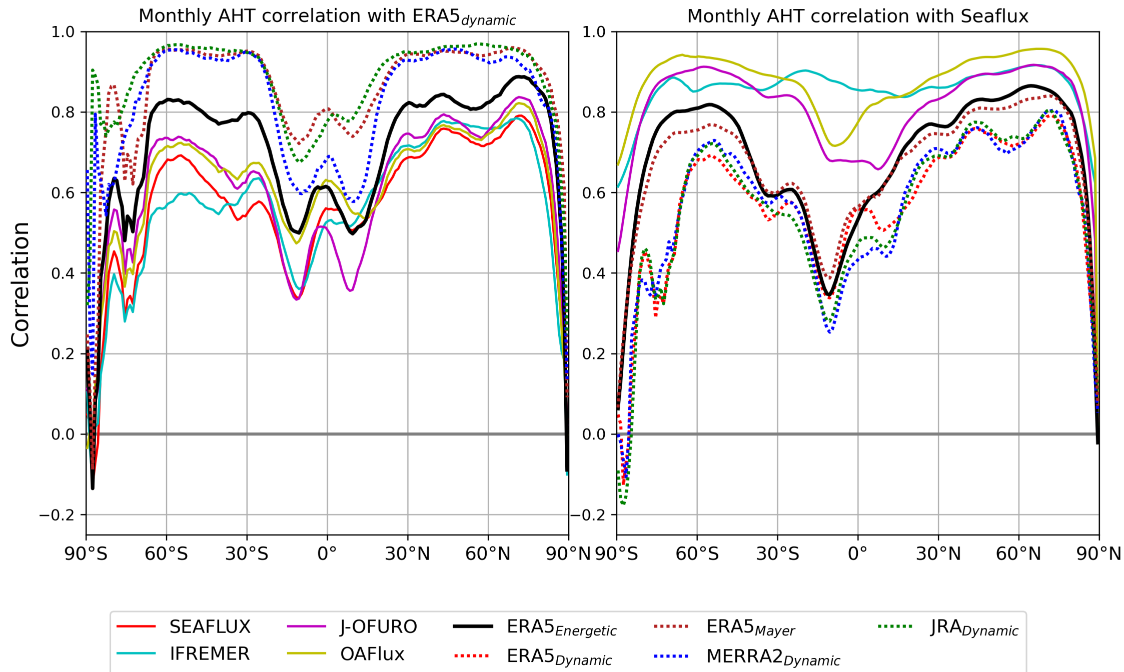

Figure 4.7: Correlation of monthly AHT anomaly (2004-2014) for each latitude band with respect to (left) ERA5$_{\text{dynamic}}$ and (right) SeaFlux. Recreated from Prince et al. (2025), with STL decomposition rather than simple climatological subtraction.

between AHT derivations are low, providing confidence that they are correctly representing the true variance of AHT.

It is also worth exploring the autocorrelation of AHT prior to examining the energetic covariance. Figure 4.9 plots the autocorrelation of the reanalysis AHT for the 42-year record (the decade-long observation record is too short to calculate a meaningful autocorrelation). Midlatitude monthly AHT has almost no autocorrelation across all reanalysis (<0.05), even at a 1-month lag. A lack of autocorrelation demonstrates that monthly anomalies in midlatitude AHT do not tend to last for more than a month, that there is no memory from an AHT anomaly from one month to the following month. JRA does have autocorrelation (about 0.2) in the Southern Hemisphere polar region (70-80°S) up to 6 months in lag, however, this is expected to be an artifact within the reanalysis and its representation of Antarctica. Tropical AHT has autocorrelation of >0.2 out to 4-7 months. In ERA5, the tropical autocorrelation reduces to zero at 5 months, while in MERRA2

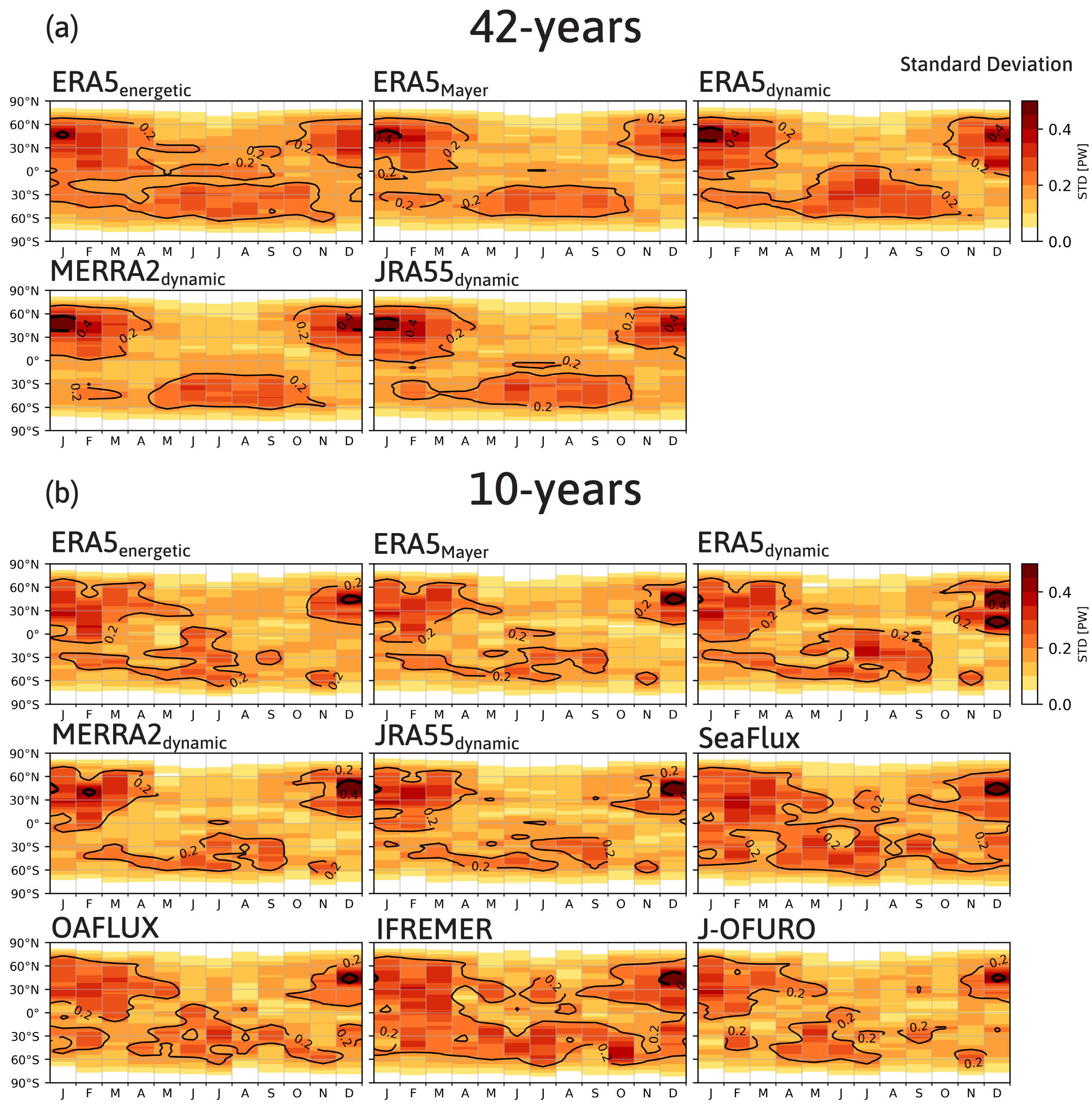

Figure 4.8: (a) AHT standard deviation of each month as calculated from 42 years of reanalysis data. (b) Same as (a) but for the reanalysis and observation AHT over the shared 10-year record.

and JRA the tropical autocorrelation south of the equator extends out to 8 months. All reanalysis demonstrate that tropical AHT is more slowly evolving than midlatitudes, with AHT anomalies tending to remain for over 3 months at a time.

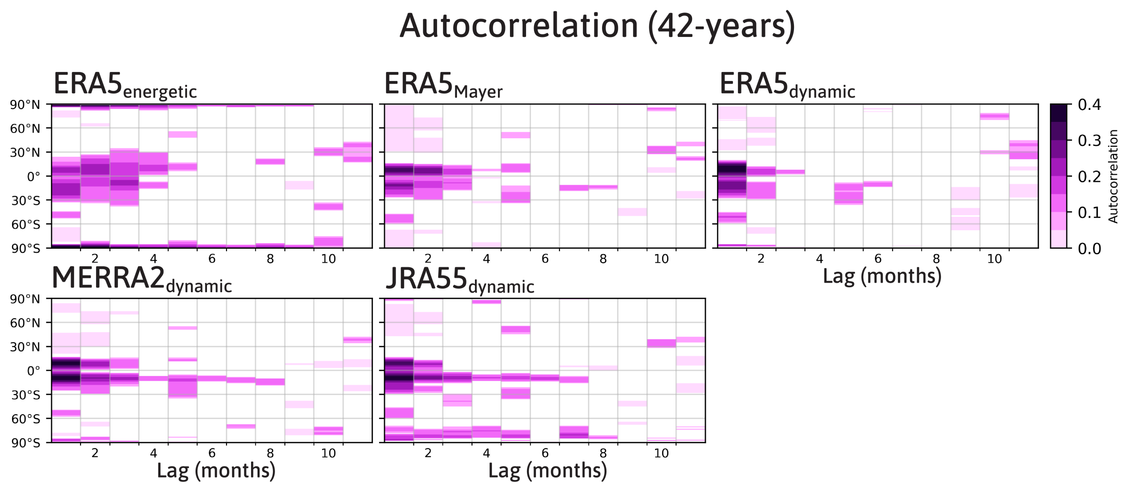

Figure 4.9: The autocorrelation of monthly reanalysis AHT for the 42-year record. Data only shown where the relationship is significant (at the 0.05 level).

Figures 4.8 and 4.9 both represent AHT variance at a given latitude, however, the spatial (meridional) extend of a zonal mean AHT anomaly is also crucial to understand the energetic contributes to AHT variance. Figure 4.10 shows the cross correlation of AHT across latitudes, examining how related the monthly AHT time series at one latitude is to monthly AHT at all other latitudes. Across all latitudes the AHT cross correlation remains above 0.5 out to 15° north and south of a given latitude. Within the Northern Hemisphere tropics (0-30°N), cross correlations remain above 0.25 across most of the hemisphere (being statistically significant at the 5% level). The timeseries of AHT through 15°N has a positive, significant correlation (exceeding 0.25) with AHT through the rest of the Northern Hemisphere (up to 80°N). This conclusion holds true across reanalysis and observations (energetic and dynamic AHT). AHT anomalies do not correlate across the equator, with only tropical AHT correlations remaining significant to within about 15° latitude into the opposite hemisphere.

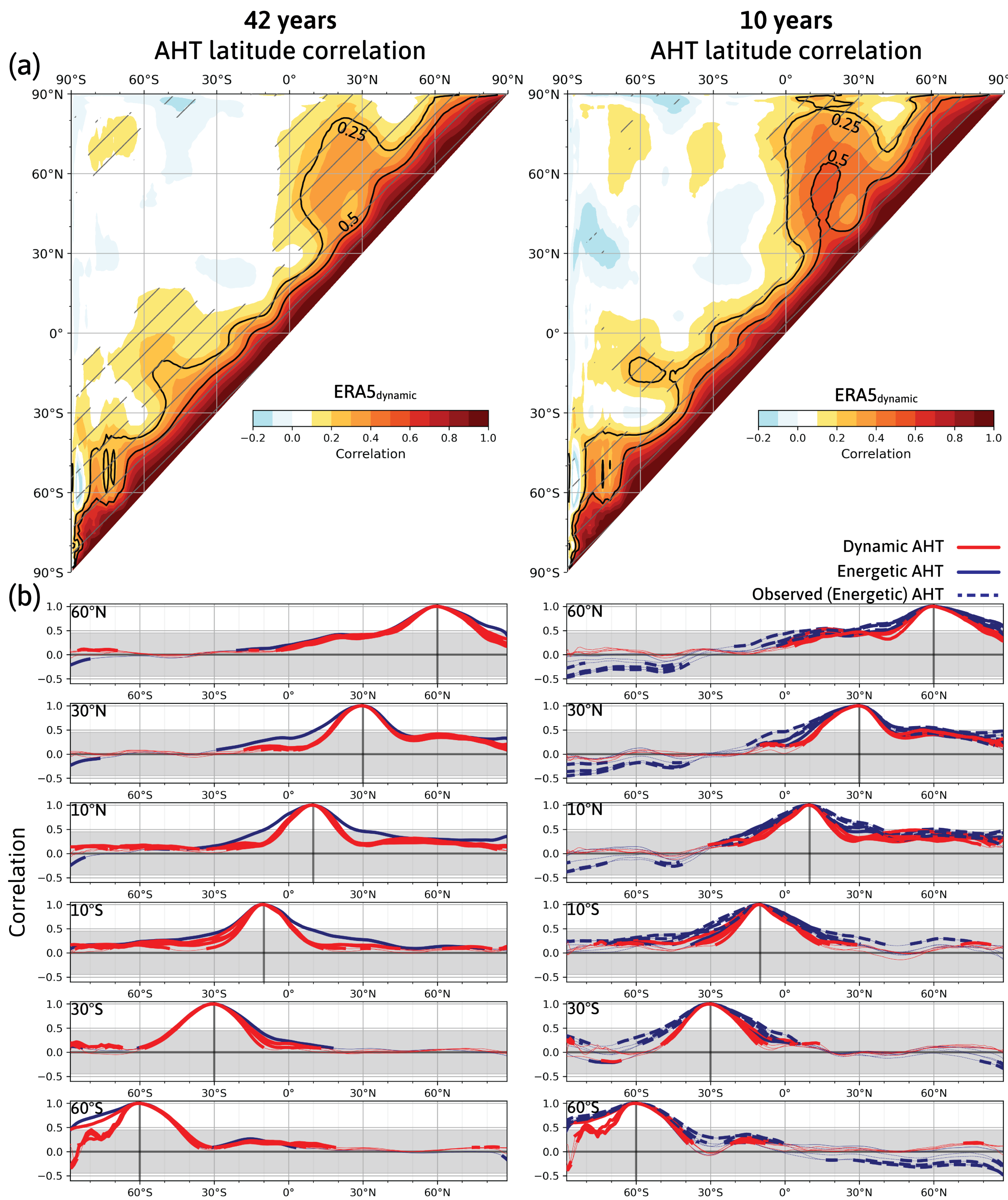

Figure 4.10: (a) Cross correlation matrix of monthly AHT for the (left) 42-year and (right) 10-year records. Stripping demonstrates statistical significance at the 5% level and bold contours are plotted for 0.25 and 0.5 correlations. (b) Cross correlation for select latitudes in the dynamic and energy AHT calculations, again shown for the (left) 42-year and (right) 10-year records. Significance at the 5% level is shown with thick lines.

4.3.2 AHT energetic contributions

The contribution and variance of the atmospheric energy budget components are shown in Figure 4.11, averaged between latitudinal bands (of 30°). Latent heating is the largest contribution of energy to the atmosphere in the tropics (equatorward of 30°) while also having the greatest standard deviation. Radiative cooling is the greatest loss of energy from the atmospheric budget, however, its interannual variance is less than half that of the tropical latent heat flux variance. Towards the polar regions, the radiative cooling becomes more dominant, accounting for over 75% of the energy budget. The relative importance of the radiative interannual variance however, does not increase relative to the other contributions. The relative magnitude of the latent heat flux standard deviation reduces towards the poles while the tendency variance becomes more important. The tendency accounts for less than 25% of the atmospheric energy budget (less than 5% in the tropics), but its standard deviation is comparable to the other components, being over twice the standard deviation of the other components in the polar regions. So while the tendency has a very low contribution to the monthly net atmospheric energy budget, it varies on the same order of magnitude, if not larger, than the other components.

Anomalous AHT across a given latitude must be associated with an addition and removal of energy to the atmospheric energy budget either side of that latitude, closing the energy budget. Figure 4.12 presents the regression coefficients of the ERA5 zonal mean AEB components when regressed against AHT as calculated from $\mathrm{ERA5}_{\mathrm{energetic}}$. At all latitudes the energetic dipole either side of a AHT anomaly is distinct, maximizing within 15° either side of a latitude, consistent with Figure 4.10. Energy transport into the midlatitudes (at 30°N/S) is associated almost exclusively with energetic gains from latent heating on the equatorial side. Poleward of the transport anomaly, the energy loss occurs from all components, radiative, sensible, latent, and tendency, almost evenly divided. This suggests that the anomalous poleward flow of energy through 30°N/S is exclusively associated with enhanced evaporation in the tropics. Following condensation, and poleward transport, this heat then contributes towards warming the atmosphere,

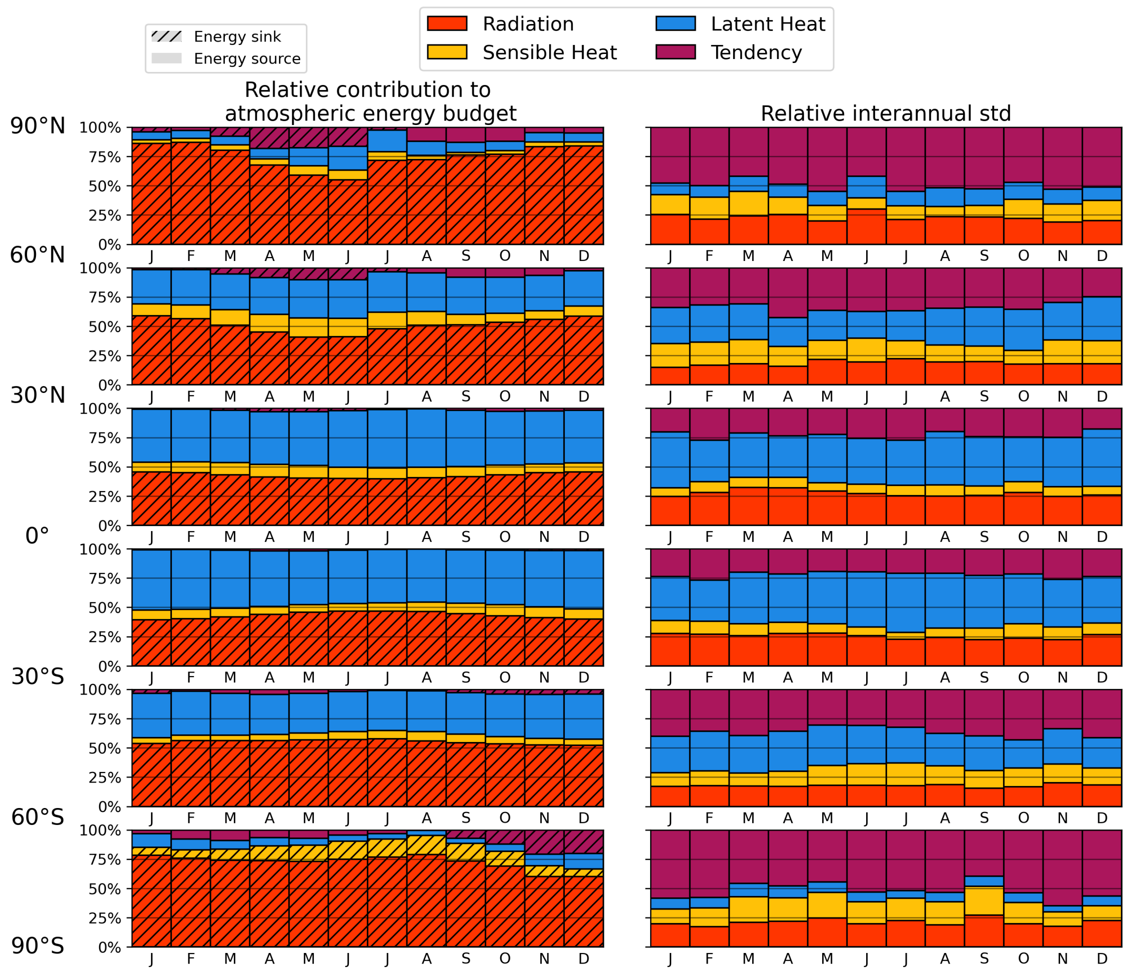

Figure 4.11: (left) The relative contribution to the monthly atmospheric energy budget as calculated by ERA5. (right) The interannual variance of each component of the energetic atmospheric heat transport shown as the relative magnitude of the monthly standard deviation.

radiative cooling, warming the surface, or reduced evaporation on the poleward side of the AHT anomaly.

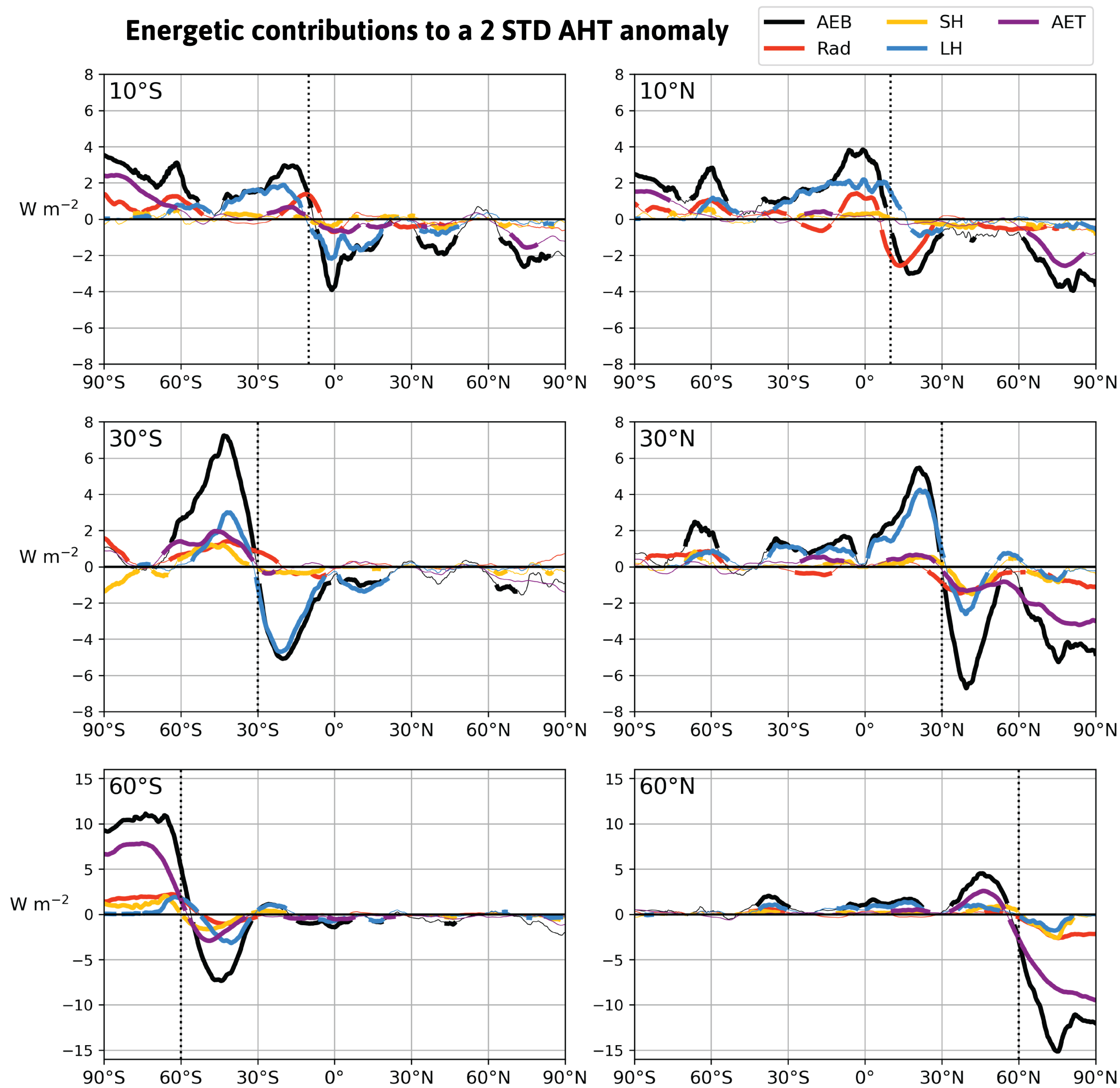

Figure 4.12: Regression coefficients of the ERA5 zonal mean AEB components when regressed against AHT as calculated from ERA5$_{\text{energetic}}$. Bold lines represents significance at the 5% confidence level.

Within the tropics, other energetic components also contribute to the energetic budget associated with AHT variance. At 10°N, energy contributions tend to come from both latent heating and radiation, while the loss of energy poleward is almost exclusively through radiative cooling. At 10°S, energy gain is mostly through latent heating, with all other components contributing small amounts with loss being through radiative and latent cooling. AHT into the polar regions (through 60°N/S) is associated with energy gains from all components equally equatorward of 60°N/S, however, almost all the energy goes into the polar energy tendency (increasing the MSE of within the polar region). All other energetic components are relatively small in comparison.

This midlatitude importance of latent heating is further explored with comparison to observations. Figure 4.13 presents the regression coefficients associated with the atmospheric energy budget as shown in 4.12 but for the decade-long (2004-2014) record shared between observation products, at 30°N/S and 40°N/S. The relative importance of the equatorward latent heat flux for a midlatitude AHT anomaly (across 30°N/S) tends to be lower in the observations than in ERA5. The radiative component in particular has increased importance in modulating the observed AEB consistent with an AHT anomaly, especially in the in the Southern Hemisphere (across 30°S and 40°S). However, the latent heat flux remains the most importance contribution of energy to the atmosphere consistent with anomalous midlatitude poleward heat transport, with an increase of up to 3 W m^{-2} in the zonal mean for a 2 standard deviation AHT anomaly. On the poleward side of an AHT anomaly, the equal share of energy loss is consistent across all observation products. For AHT across 30°N/S, the loss of heat through sensible, latent, radiative, and tendency is shared approximately equally. At 40°N/S, the tendency starts to become more sensitive to AHT anomalies, consistent with the results presented in Figure 4.12. Broadly, the observations corroborate the importance of the atmospheric warming from the latent heat flux during midlatitude AHT anomalies.

The full relationship between the AEB and the standardized AHT (standardized anomaly) across each latitude pair is presented in Figure 4.14 from ERA5 data, demonstrating both the level of correlation and the regression coefficient, paired with the statistical significance. The AEB forms a dipole of energy gain and loss either side of an AHT anomaly within a given month. At 30°S for example, a northward AHT anomaly is associated with gains and losses to the AEB with correlations exceeding 0.5 within ±15° either

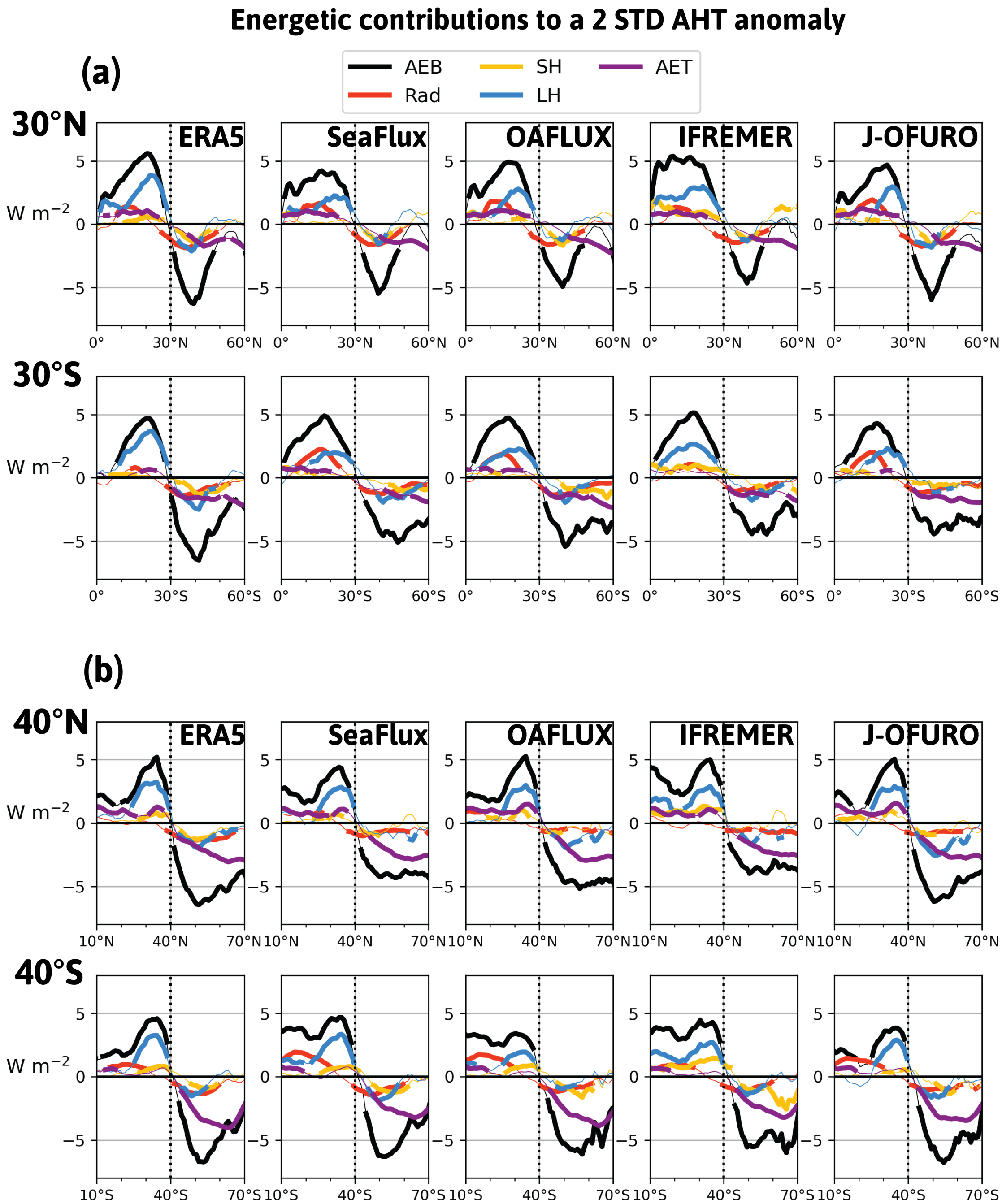

Figure 4.13: Regression coefficients of the ERA5 and observations zonal mean AEB components for (a) 30°N/S and (b) 40°N/S when regressed against the standardized energetic AHT derived from each AEB. Bold lines represents significance at the 5% confidence level. The x-axis has been rotated to represent the tropics on the left and the poles on the right, with positive values representing energy fluxes into the atmosphere consistent with poleward AHT.

side an AHT anomaly. This result is consistent with Figure 4.10, which demonstrates the limited meridional extent of a monthly AHT anomaly. Within the polar regions, the correlation becomes stronger, exceeding 0.8. This is a function of the non-transport requirement at the pole, where an AHT anomaly flowing into a small polar cap will have a concentrated effect on the AEB (within a limited meridional extent). While an AHT anomaly across the equator may provide energetic closure through energy gains and loss across the entire hemisphere.

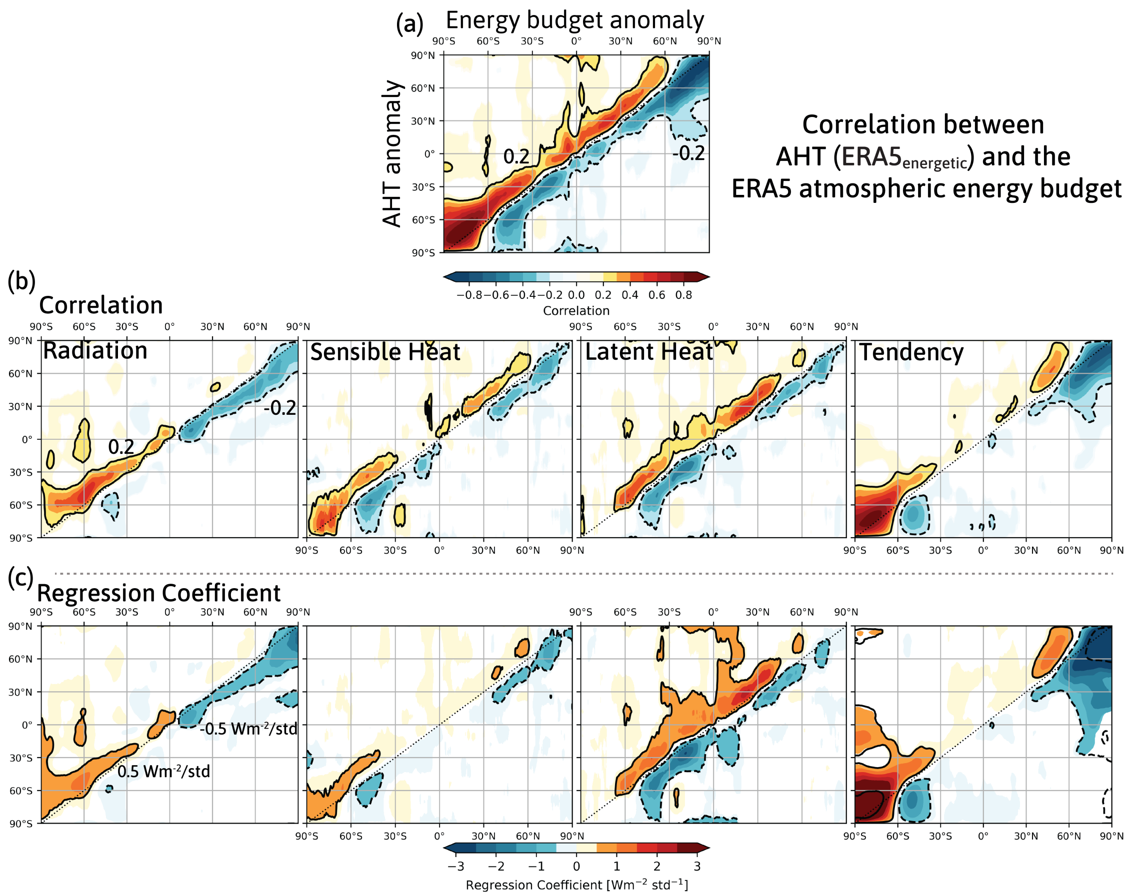

Figure 4.14: (a) Correlation matrix between the standardized AHT anomaly and atmospheric energy budget (AEB), contours represent -0.2 and 0.2 correlations. (b) Correlation matrix between AHT and each of the energy budget components. (c) Regression coefficients for the relationship between AHT and each of the energy budget components, contours represent 0.5 W m^{-2}/standard deviation (std). For all plots data only shown for statistically significant relationships at the 5% level.

The full breakdown of an AHT anomaly to each component in Figure 4.14 completes the understanding suggested through Figure 4.12. Within the tropics, especially close to the ITCZ, radiative exchange and latent heating account for much of the AEB variance through AHT. Radiative heating and cooling anomalies either side of 10°N have a ±0.3 correlation with AHT at that latitude, resulting in variations in the zonal mean radiative receipt of up to ±1 W m^{-2}/std. Outside the tropics, the zonal mean radiation response to AHT is solely on the poleward side of the AHT anomaly. This demonstrates that anomalous AHT is not associated with increased radiative absorption on the equatorward side, but rather through negative radiative anomalies on the poleward side (such as through increased thermal emission or reduced solar absorption).

In the subtropics to midlatitudes, the latent heating has the greatest regression coefficient, exceeding 2 W m^{-2}/std with zonal mean correlations of up to 0.5. The latent heat flux coefficient maximizes on the equatorward side of an AHT anomaly, demonstrating the role of energy gains through latent heating associated with increased poleward flow, in agreement with Figure 4.13. While the sensible heat flux has midlatitude correlations of up to 0.4, the magnitude of relationship is low (less than 1 W m^{-2}/std). The sensible heat flux does remain correlated with AHT further towards the polar regions than the latent heat flux, suggesting a shift in the relative importance of the two turbulent heat fluxes further poleward. Within the polar regions (poleward of 60°N) the tendency has a very close relationship with AHT anomalies, especially on the poleward side of an anomaly. This represents a convergence of energy transport increasing the MSE within the region, exceeding 3 W m^{-2}/std with a correlation of over 0.8. The tendency dipole across 60°N/S is indicative of a divergence of MSE on the equatorward side and convergence of MSE transport on the poleward side of an AHT anomaly. Within the tropics and midlatitudes, AHT anomalies do not have meaningful impacts on the zonal mean tendency (changes in the zonal mean MSE).

Figure 4.14 demonstrates that there tends to be a negative radiative anomaly on the poleward side of a poleward AHT anomaly. Figure 4.15 examines the radiative components (shortwave and longwave at both TOA and the surface) associated with anomalous AHT in the high midlatitudes (across 60°) where radiation has a particularly close relationship with AHT. The longwave component is the dominant radiative response to an AHT anomaly, especially on the poleward side of the anomaly. There is an increased longwave deficit within the polar regions when AHT into the region is enhanced, with both increases in the emission to space (OLR) and increase longwave receipt at the surface. This is consistent with a Planck feedback, balancing increased energy into the region. The polar radiative deficit is also enhanced by a shortwave deficit, with reduced shortwave absorption by the atmosphere, suggesting increased shortwave reflection potentially from cloud cover.

4.3.3 Implied AHT and covariance

AHT anomalies are clearly associated with anomalous gradients in the atmospheric energy budget, forming a dipole of anomalous energy addition and loss either side an AHT anomaly. The anomalous forcing these energetic dipoles have on the total AHT can be examined by calculating the implied transport with Eq. 4.2. Figure 4.16 shows the coefficient of determination (r^2) of the implied AHT forcing from each component to the total AHT. While net radiation accounts for approximately 50% of the energy budget for a given latitude band (as a loss of energy), its variance describes only a small amount (less than 30%) of the monthly AHT variance. The implied forcing from radiation maximizes at 5°N, at the ITCZ, where the dipole of radiative exchange is closely related to the total AHT variance at this latitude (Figure 4.14). The implied radiative AHT has a secondary peak in the Southern Hemisphere midlatitudes centered at 55°S, also aliging with the close correlation of the zonal mean radiative cooling on the poleward side of a poleward AHT anomaly.

Latent heating is the largest contribution of energy to the atmosphere (Figure 4.2) and its variance describes about 30% of the AHT variability throughout the tropics. The sensible heat flux accounts for less than a quarter of the total energy budget at a given latitude band (Figure 4.2), but the variance in its poleward gradient describes up to

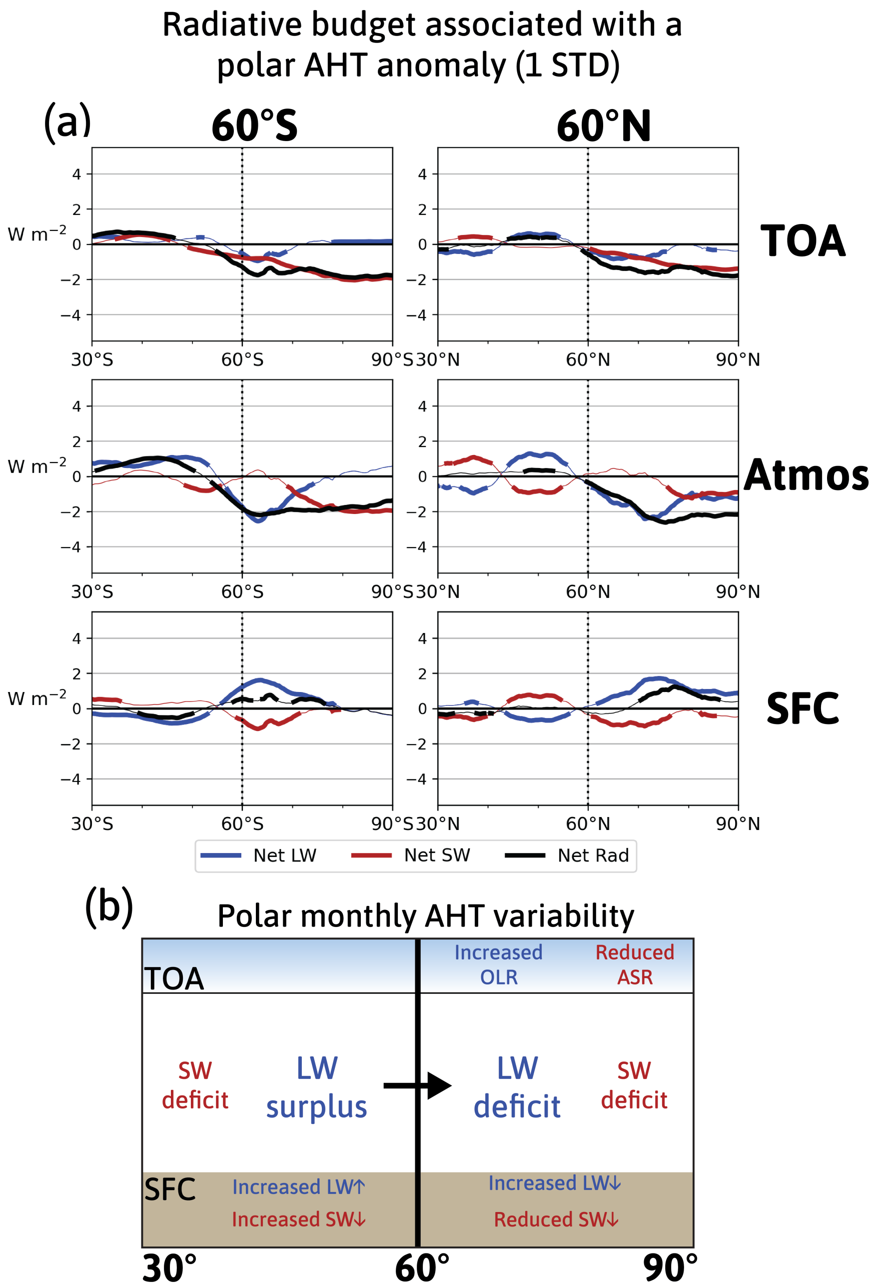

Figure 4.15: (a) Regression coefficients of the zonal mean ERA5 radiative components regressed against the standardized energetic AHT for and polar (60°N/S) AHT. Bold lines represents significance at the 5% confidence level. The x-axis has been rotated to represent poleward flow towards the right. Positive fluxes represent positive net radiative energy at each level. (b) Summary figure of the radiative response to AHT for polar AHT.

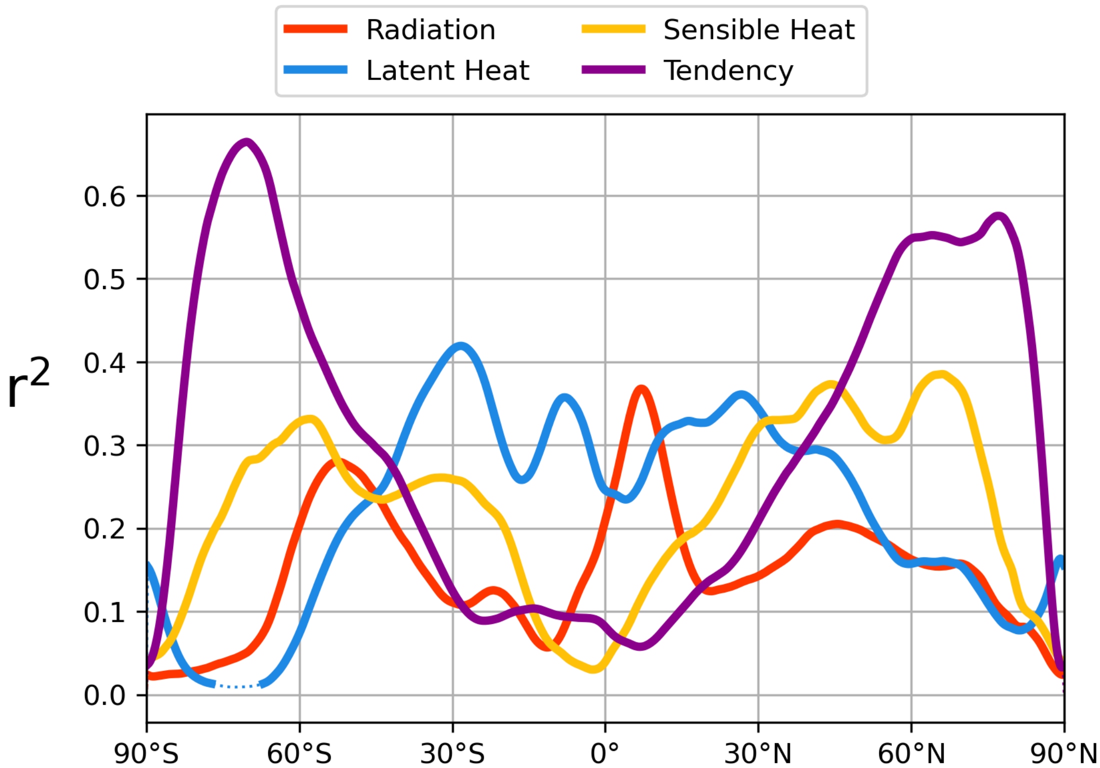

Figure 4.16: Coefficients of determination (r^2) from regressing monthly AHT onto the energetic forcing terms, the implied AHT each energy component contributes to through a given latitude band (as described by Eq. 4.2). Thin dotted lines represent where the p-value exceeds 0.01

30% and 40% of AHT variability in the Southern and Northern Hemisphere midlatitudes respectively. Perhaps the most intriguing relationship is that the atmospheric tendency describes over 50% of the AHT variance into the polar regions (through 60-70°N/S) while accounting for less than a quarter of the energy budget within the monthly polar energy budget. One interpretation could be that the polar vertically integrated air temperatures are more highly variable in time than the surface and TOA fluxes, being more consistent with the polar AHT variance. These findings demonstrate the AHT variance described by each component; however, it does not capture the different relative magnitudes of these each component. To do that, a removal correlation experiment is undertaken to demonstrate how these components combine to describe the total AHT.

Figure 4.17a demonstrates how the predictive power of the implied energy budget AHT reduces with the removal of individual terms. By construction, the implied AHT of the full energy budget is equal to the total AHT and describes 100% of the AHT variance. For AHT anomalies at 60°N, the removal of radiative fluxes only reduces the predictive power by 13%. In other words, if AHT was calculated excluding any radiative fluxes, the resultant data describes 87% of the variance of the total AHT. Clearly, the forcing from the radiative components only play a small role in defining AHT variance into the Arctic. Removing the sensible and latent heat flux implied AHT reduces the predictive power by 10% and 22% respectively. The tendency (AET) is the most important component for describing the AHT variance, accounting for 55% of the AHT variance across 60°N. Over half of the AHT flowing into the Arctic is described by the changing MSE of the atmospheric column, with the latent, radiative, and sensible fluxes combined accounting for the remaining variance. Within the tropics, at 10°N, the relative importance of radiation is increased, describing 30% of the AHT variance. Removing the sensible heat flux reduces the descriptive power by 15% while the latent heat flux reduces it by a further 49%. The AHT forcing from the tendency alone only describes 7% of the AHT variance at 10°N.

Figure 4.17b demonstrates the removal regression experiment for every latitude. When compared to $\text{ERA5}_{\text{energetic}}$, by construction, 100% of the variance is by the full energy budget at all latitudes. The importance of radiative forcing on the total AHT is apparent in the tropics, accounting for over 20% of the AHT variance between 30°S and 10°N, maximizing to 40% at 5°N with a secondary peak at 20°S. The removal of the sensible heat flux has an almost uniform impact across latitudes, reducing the regression coefficient by approximately 10%. The importance of the latent heat flux is distinct in the tropics, maximizing at the equator, reducing the variance by up to 50% with minimums in the polar regions of less than 10%. When comparing the implied forcing to the dynamic AHT calculations, these differences scale with the reduction in the total AHT regression.

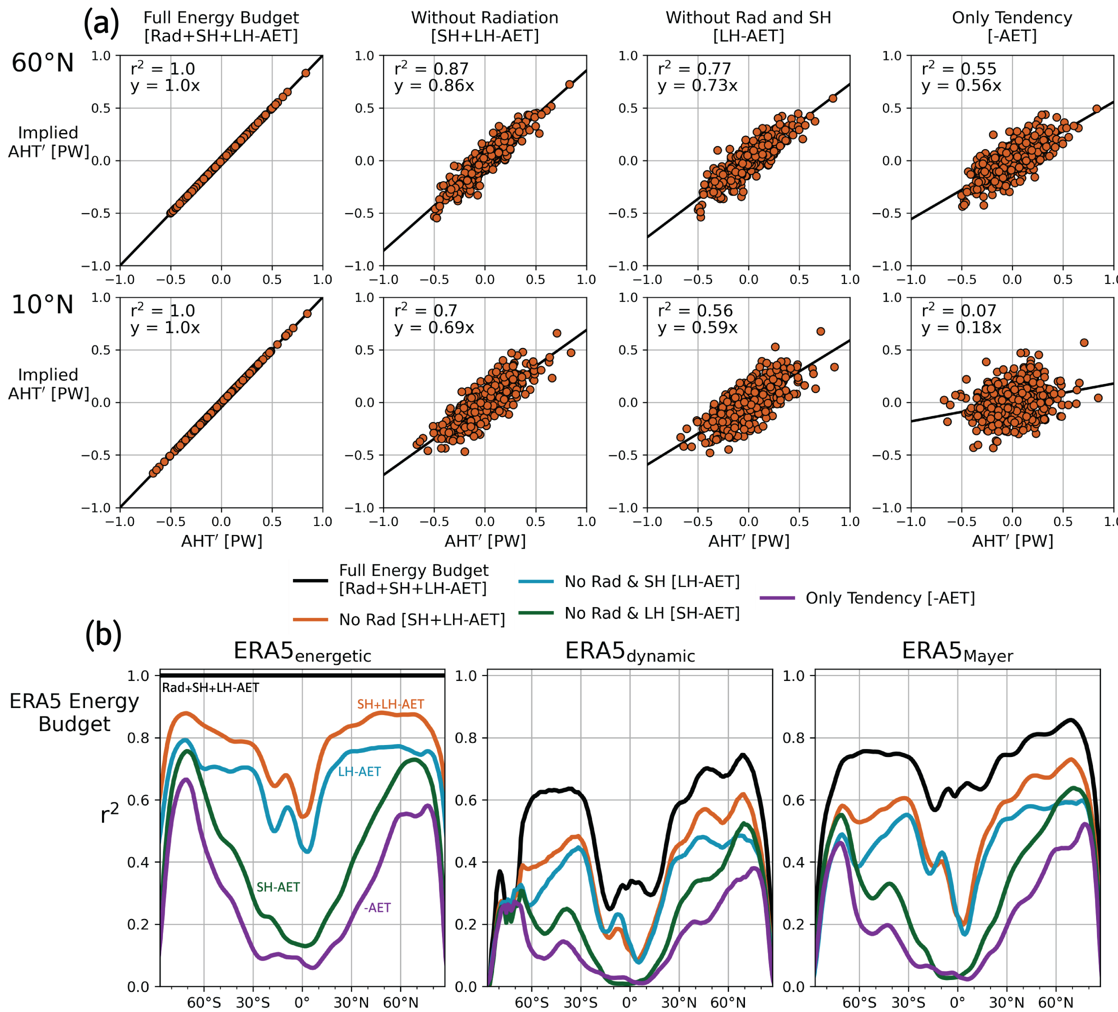

Figure 4.17: Removal regression experiment, testing the relative importance in energy budget components on describing the total AHT variance through their implied AHT at (a) 60°N and 10°N where each point represents a monthly anomaly at that latitude as calculated by both the full AHT and implied (removed) AHT. (b) The removal regression is plotted for each latitude as calculated from the ERA5 energy budget against the $\text{ERA5}_{\text{energetic}}$, $\text{ERA5}_{\text{dynamic}}$, and $\text{ERA5}_{\text{Mayer}}$ records of AHT.

4.3.4 Spatial pattern of covariance

This analysis so far has focused on the zonal mean covariance between the atmospheric energy budget components and the zonal mean AHT. A clear dipole of energy gain and loss extending 15° either side an AHT anomaly has been demonstrated in the zonal mean, however, this analysis provides no information about the locations of energy gain and loss. Figure 4.18 presents the spatial nature of the atmospheric energy budget correlations with AHT at 10°, 30°, and 60° in the Southern and Northern Hemispheres. Tropical AHT variance across 10°S is strongly associated with energy gain in the central tropical Pacific, centered on the equator, with low correlations in the Indian and Atlantic oceans. Regions of energy loss appear in the Indian Ocean northwest of Australia and in the substropical and South Pacific Ocean. Poleward heat transport across 10°N is associated with energy gain in both the Pacific and Indian oceans, with the largest gains in the east Pacific, maximizing on the equator and extending southward (out to 10°S). Atmospheric energy fluxes over the maritime continent are negatively associated with poleward AHT across 10°N.

Poleward transport across 30°S energy is associated with four distinct dipoles situated across the Southern Hemisphere midlatitudes in the southern Atlantic, Indian, and Pacific Oceans. In the Northern Hemisphere, AHT across 30°N has a less regular pattern, with a strong dipole of energy exchange in the Atlantic and Pacific Oceans and weak energy gains in the Indian Ocean. A large region of energy loss in the Barents Sea in the Arctic is also significantly correlated with AHT across 30°N. For poleward AHT across 60°S (towards Antarctica), three regions of preferential atmospheric heating are present in the south Atlantic, Indian, and southwest Pacific Oceans. The loss of energy from the budget occurs over the entirety of Antarctica, with large regression coefficients in the Ross and Amundsen Seas. For the Arctic, poleward AHT across 60°N, energy gain occurs in small regions over the north Pacific with statistically significant energy loss over the entire Arctic region. However, energy loss is concentrated in a small region (similar to Antarctica) over the North Atlantic, Norwegian Sea, and Barents Sea.

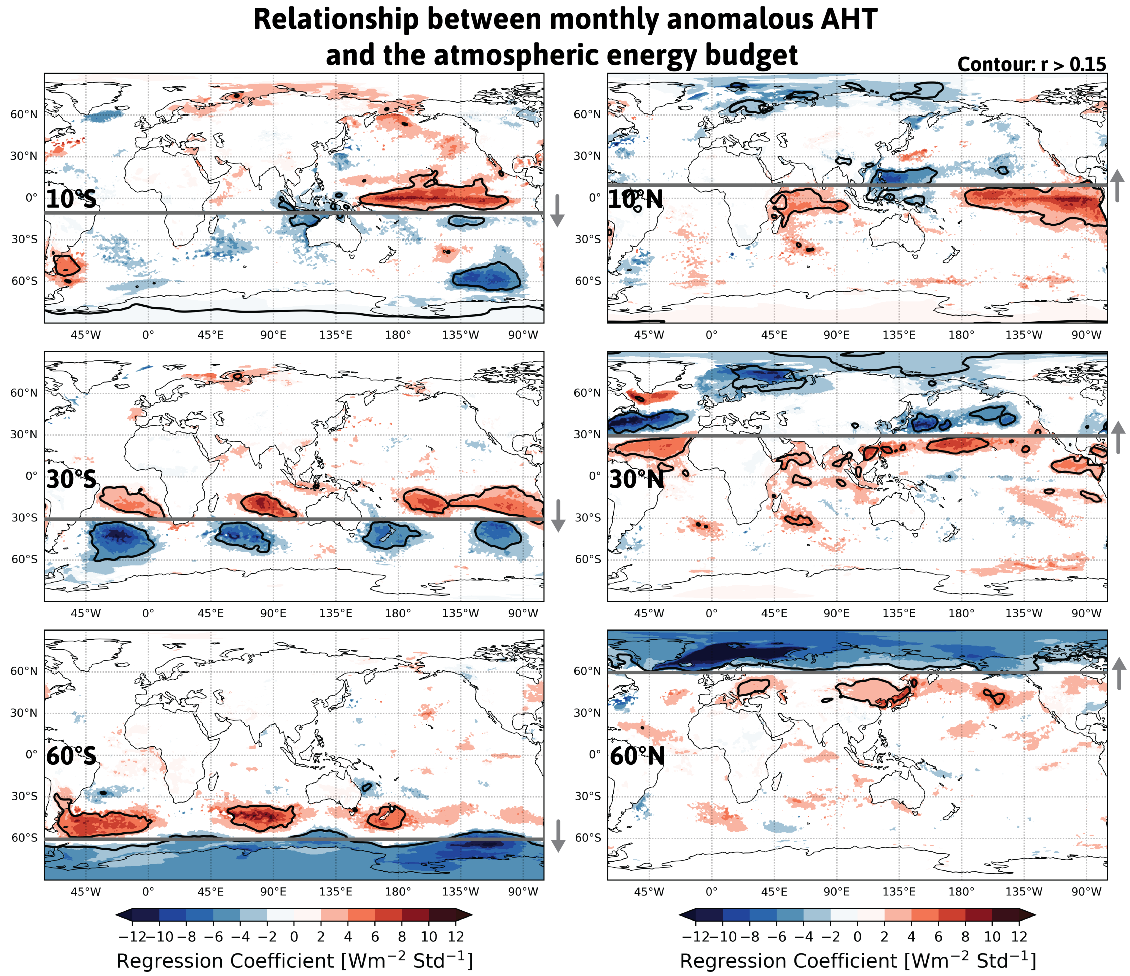

Figure 4.18: Correlation between zonal mean poleward AHT and the total atmospheric energy budget for 10°, 30°, and 60° in the Southern (left) and Northern (right) Hemispheres as calculated from 42-years of ERA5 reanalysis. Positive values (red) represent a gain of energy to the monthly mean atmospheric energy budget and negative (blue) represents a loss of energy. Data is only shown that is statistically significance at the 5% level and contours represent where the correlation coefficient exceeds 0.15.

It is important to consider that the atmospheric energy tendency is considered as part of the atmospheric energy budget here, so a loss of energy available for AHT through an increase in the local MSE (a convergence of AHT). This balance between energy flux terms and the tendency are explored in the following section. To provide additional context to these presented spatial relationships with poleward AHT, these correlations are separated into the energy budget components at 10°N, 30°S and 60°N, providing tropical, midlatitude, and polar case studies.

Figure 4.19 presents the standardized regression between each energy budget component and monthly AHT across 10°N. The largest gains of energy are from radiative absorption (up to 5 W m^{-2} std^{-1}) and surface latent heat fluxes (exceeding 6 W m^{-2} std^{-1}). The positive radiative anomaly is situated on and just above the equator while the increased latent heating is occurring either side the equator, at 10°N and down to 20°S. Both of these anomalies are in the central and eastern tropical Pacific Ocean. Negative radiative anomalies are occurring across the entire Pacific Ocean to the north of the AHT anomaly, however, at a small magnitude (less than 3 W m^{-2} std^{-1}). The negative latent heating anomaly in the western Pacific Ocean (paired with negative radiative anomalies) produce the net loss of energy to close the energy budget, situated over the maritime continent in Figure 4.18. While sensible heating does have regions with statistically significant relationships to AHT, the magnitude is small, less than 1 W m^{-2} std^{-1}. There is a broad region of energy loss to the atmospheric tendency over the Arctic, specifically the Barents Sea on the order of 3 W m^{-2} std^{-1}, representing an increase in the local MSE over the Arctic during anomalous AHT across 10°N. There is no strong relationship immediately either side 10°N demonstrating that local divergence or convergence of MSE is not associated with AHT across 10°N.

Southern Hemisphere midlatitude AHT (across 30°S) is associated with four distinct dipoles of energy gain and loss (Figure 4.18). In examination of the energy budget components response, the vast majority of this response comes from latent heating - increased latent heating to the north and reduced latent heating to the south (on the order of $\pm$5 W m^{-2} std^{-1}), inducing an anomaly in the poleward energy budget (Figure 4.20). While sensible heating also has a small contribution to the position energy budget anomaly poleward of 30°S (<1 W m^{-2} std^{-1}), the majority of the energy gain is from latent heating. All components of the energy budget has significant responses to the south of a 30°S AHT anomaly, radiative cooling, sensible and latent heat fluxes towards the surface, and increases in the atmospheric tendency. However, the latent heat flux dominates the loss

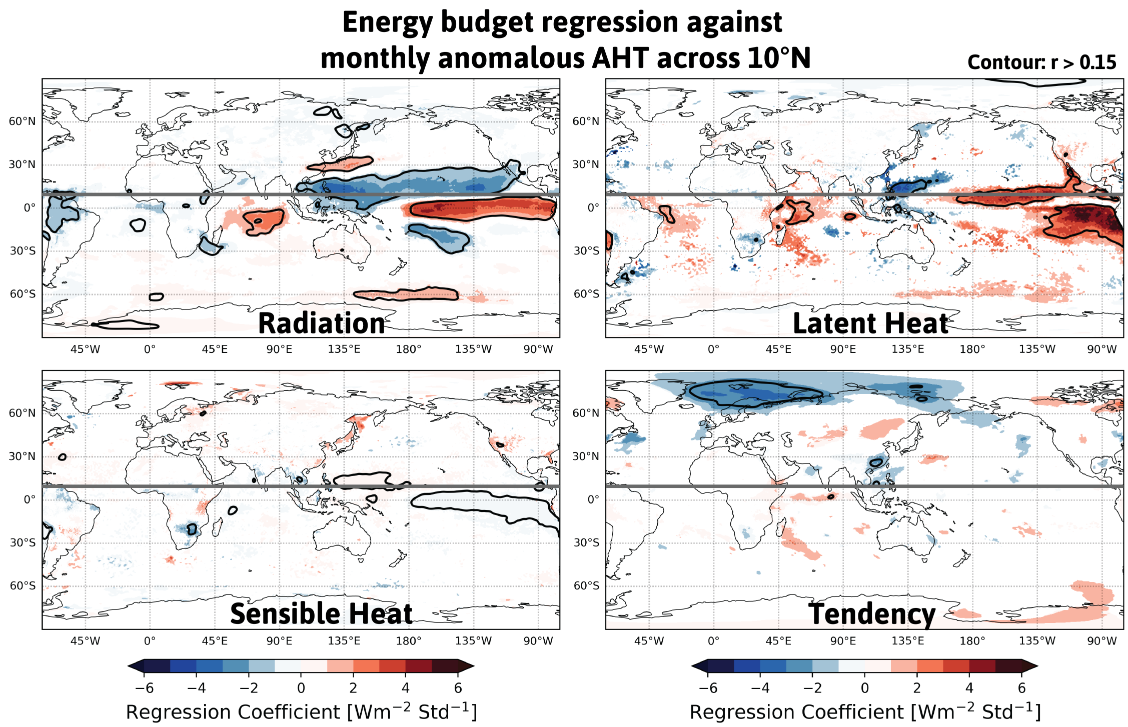

Figure 4.19: Correlation between zonal mean poleward AHT and the atmospheric energy budget components for 10°N as calculated from 42-years of ERA5 reanalysis. Positive values (red) represent a gain of energy to the monthly mean atmospheric energy budget and negative (blue) represents a loss of energy. Data is only shown that is statistically significance at the 5% level and contours represent where the correlation coefficient exceeds 0.15.

of energy, with regression coefficients approximately twice that of the other components. These results are in close agreement with those presented previously for the zonal means (Figure 4.13) demonstrating that midlatitude energy transport is dominated by energy gains from latent heating paired with atmospheric energy losses from all terms.

Anomalous AHT into the Arctic is strongly associated with the convergence of AHT, increasing the atmospheric tendency poleward of 60°N. There are regions of tendency gains (divergence of MSE) over eastern Europe, northeast Asia and across the north Pacific while the entire Arctic region experiences MSE convergence and increases in the tendency on the order of 4 W m^{-2} std^{-1}. As a rough approximation, a 1 W m^{-2} positive anomaly over the course of a month corresponds to a temperature increase of about 0.3°C. So

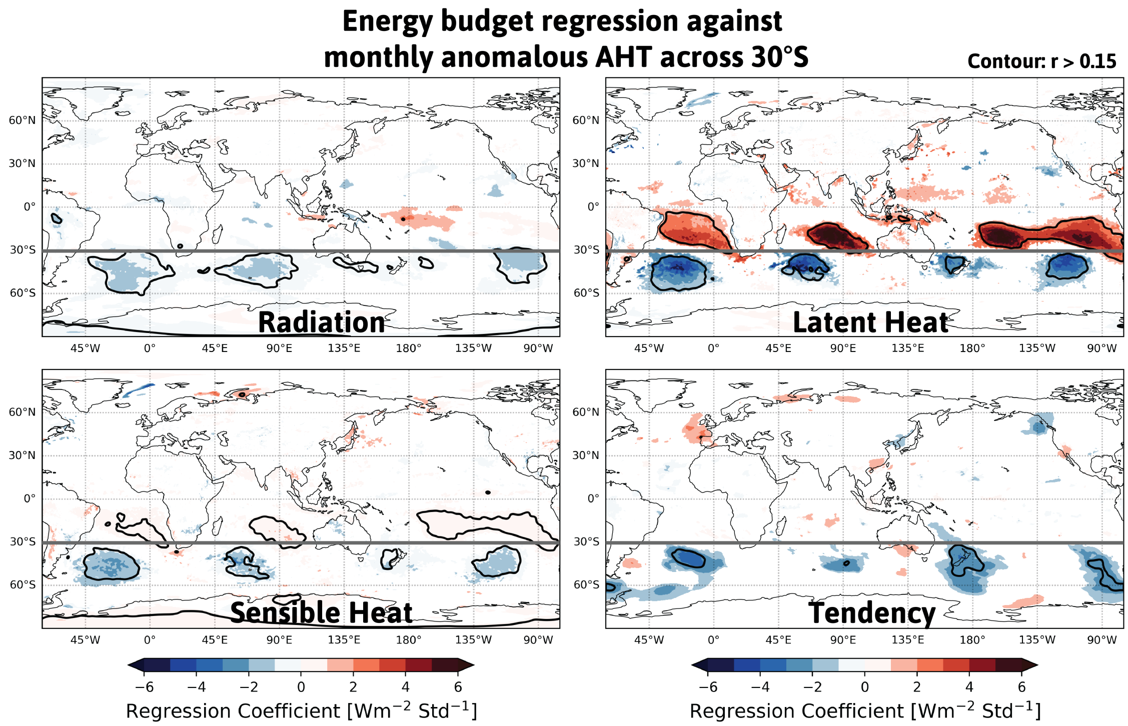

Figure 4.20: Same as Figure 4.19, but for 30°S.

this tendency regression coefficient for monthly Arctic AHT corresponds to warming of the Arctic atmosphere of approximately 1°C for a 1 standard deviation anomaly in AHT (assuming all energy is in the form of temperature and not moisture). It is also important to remember a 1 W m^{-2} std^{-1} regression at lower latitudes responds to a greater amount of energy input into the atmosphere than at higher latitudes due to the convergence of area towards the pole. So the difference in extent and magnitude for the tendency dipole either side 60°N does not necessarily mean that they are not balancing each other. There are also large negative anomalies in the sensible and latent heat fluxes over the Barents Sea, the sea ice free region of the Arctic, on the order of 6 W m^{-2} std^{-1}. Radiative cooling, on the order of 1 W m^{-2} std^{-1} across the entire Arctic completes the polar negative energy anomaly associated with 60°N AHT.

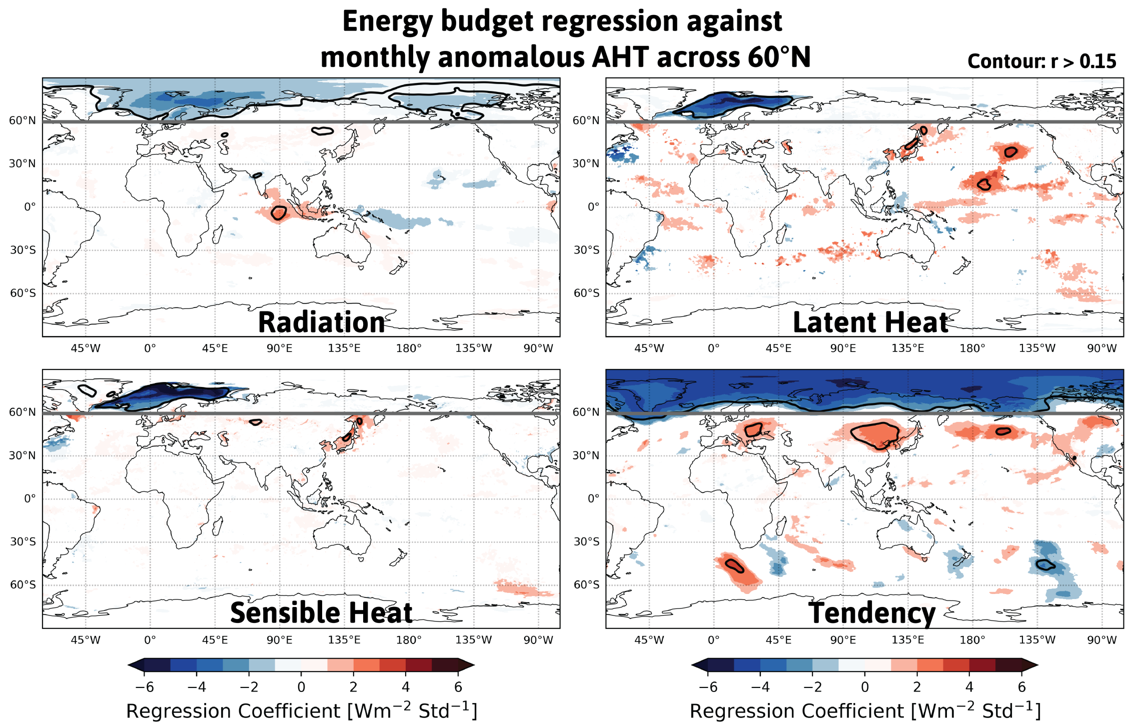

Figure 4.21: Same as Figure 4.19, but for 60°N.

4.4 Discussion and conclusions

An assessment of the atmospheric energy budget components consistent with monthly AHT variance has been presented from both reanalysis and observations. The historical AHT data underwent a Seasonal-Trend decomposition using LOESS (STL) to remove nonstationarity seasonality and differing long term trends (including low frequency variability), isolating the monthly anomalies. Monthly AHT anomalies maximize in the midlatitude winters, however, the minimum monthly variance is similar across most of the Earth, tropics and midlatitudes. The maximum wintertime AHT variance aligns with seasonal maximums in AHT, the midlatitude storm tracks, and baroclinicity (Nakamura and Shimpo, 2004; Hoskins and Hodges, 2019; Prince et al., 2025). Midlatitude AHT does not have lagged correlation from one month to the other, suggesting that the circulation-MSE relationship required to enhanced zonal mean AHT (Messori and Czaja, 2014) is highly variable and does not persist for more than a month. Tropical AHT has lagged correlations of 0.3 out to 5 months, demonstrating the more slowly evolving anomalies in AHT, which aligns with other lower frequency variability within the tropics, such as the El Niño Southern Oscillation (Barnett, 1991; Donohoe et al., 2014). The AHT across neighboring latitudes is fairly well correlated, above 0.5 within 15° latitude. In the Northern Hemisphere, midlatitude AHT has reasonable correlation (exceeding 0.25) down to the equator demonstrating consistency in AHT anomalies across the entire hemisphere - when AHT through 60°N is elevated, it will be somewhat related to elevated AHT through 10°N. In the Southern Hemisphere, this relationship is statistically significant, but much weaker (correlations less than 0.25).

When considering the energetic components associated with AHT it is important to consider the mean state first. The annual mean atmospheric energy budget is dominated by a loss of energy through radiative cooling of about 100 W m^{-2} across all latitudes paired with a gain of energy through latent heating, maximizing at 125 W m^{-2} within the tropics. Sensible heating only adds a small (20 W m^{-2}) amount of energy to the atmosphere. When considering the monthly mean contributions, the atmospheric tendency accounts for up to 20% (30 W m^{-2}) of the total atmospheric energy budget, corresponding to the seasonal increases and decreases in the zonal mean MSE. However, the tendency has a disproportionate impact on the the monthly total energy budget variance, accounting for between 25% and 50% of the variance (maximizing in the polar regions). The latent heat flux is the largest source of variance in the tropics (equatorward of 30°), with radiation and sensible heating accounting for about 30% of the variance in the atmospheric energy budget combined.

The importance of tropical latent heating in modulating energy transport into the midlatitudes is a conclusion supported by all results presented herein. When the zonal mean energy budget is regressed against AHT across 30°, the vast majority of energy on the equatorward side is from the latent heat flux. This result is consistent across reanalysis and observations. Clearly, the energy that flows into the midlatitudes from the equator is closely related to the magnitude of evaporation within the tropics. Furthermore, this suggests the unimportance of variability in the tropical radiative receipt on energy transport into the midlatitudes. While there is appreciable variability in the tropical radiative receipt, it is poorly correlated with heat transport into the midlatitudes, however, this does vary between observational products.

The role of tropical evaporation on the general circulation has been previously discussed. Trenberth and Stepaniak (2003) demonstrate that latent heating provides the bulk of the poleward energy transport through the low to midlatitudes, with this transport occurring in the form of of dry static energy. Fajber et al. (2023) provides a similar discussion, that a large component of the dry air energy transport comes from condensing water vapor, converting moisture transport into dry air heat transport. This process is implicit in the results presented here. While latent heating of the atmosphere is increasing the atmospheric energy budget on the equatorward side of an AHT anomaly, the energy release on the poleward side is through all components (including sensible and radiative cooling). On the poleward side of an AHT anomaly, the atmosphere has increased turbulent heat fluxes towards the surface (warming the surface) paired with increased radiative cooling. These results demonstrate that the variability of tropical evaporation (and subsequent condensation of moisture) is the largest control on the magnitude of energy flowing into the midlatitudes. Here, we demonstrate this relationship from state-of-the-art observations and reanalysis from an energy transport perspective.

While the atmospheric dynamics associated with AHT were not examined in this analysis (for further discussion see Armour et al. 2019), the spatial distribution of energy exchange (particularly latent heating) for AHT across 30°S is distinct and deserves further discussion. The four distinct dipoles of atmospheric diabatic heating and cooling are reminiscent of the large planetary scale waves (wavenumbers$<$4) present in the Southern Hemisphere (Trenberth and Mo, 1985; Raphael, 2004; Goyal et al., 2022). Messori and Czaja (2014) demonstrated the importance of planetary scale waves and stationary eddies for zonal mean AHT, and the results presented here demonstrate a clear preferential wave for enhanced poleward AHT through the Southern Hemisphere midlatitudes. In the

Southern Hemisphere, the wavenumber 3 accounts for the largest variance in geopotential height, contributing to majority of both monthly and interannual circulation variability (Raphael, 2004) along with the distribution of blocking and persistent geopotential anomalies (Trenberth and Mo, 1985). While the energetic dipoles do not exactly resemble the Southern Hemisphere wavenumber 3, it does have multiple preferential locations in which the circulation tends to slow and persist (Trenberth and Mo, 1985), which combined may provide the spatial distributions of heating and cooling presented here. It would be worth further examining the connection between the atmospheric energy budget and circulation for AHT through a given latitude paired with an assessment of the associated observed weather, such as blocking occurrence or precipitation anomalies.

Within the polar regions the importance of latent heating becomes less important and the other energy budget components play a larger role (in agreement with Trenberth and Stepaniak 2003). For AHT across 60°, variability in the atmospheric energy tendency is the most important energy budget component, representing divergence and convergence of MSE transport. Indeed, over half of the AHT variance at 60° is described by the anomalous gradient in the atmospheric energy tendency. This role of AHT on changing the polar tendency has previously been discussed in the development of polar heat waves. Blanchard-Wrigglesworth et al. (2023) demonstrate that AHT convergence, and subsequent MSE increases is associated with the most intense heatwaves in Antarctica, with radiative and surface energy fluxes being of secondary importance. We further this discussion by demonstrating the close relationship between the tendency and AHT in both polar regions through a full breakdown of the energy budget terms.

A somewhat surprising feature of the polar regions is the relative unimportance of radiative processes consistent with anomalous AHT. Radiative cooling to space over the polar regions far exceed the solar absorption (by approximately two thirds) and so is therefore, considered a crucial component in controlling the poleward heat transport (L'Ecuyer et al., 2021). While radiative cooling is the greatest flux in the polar energy budget, we demonstrate here that on monthly timescales, the variance of polar radiative cooling and its impact on the meridional energy budget gradient is far smaller than the variance of the atmospheric energy tendency. If we were to examine energy processes in the polar regions with the goal of understanding heat transport variability on monthly scales, then the divergence and convergence of MSE is far more important than radiative cooling. It is important to reiterate that this analysis and conclusion is based on monthly variability. The importance of radiative variability for AHT on interannual and longer climate change timescales remains unexplored and an important research question.

Within the tropics is the only region where radiative forcing has a dominant contribution to AHT, with the anomalous radiative energy gradient explaining up to 50% of the variance in AHT across 10°N, with a distinct dipole of radiative energy anomalies either side this latitude (within 15°). From the spatial analysis, the positive radiative gain is centered along the equator in the central and eastern Pacific with negative radiative anomalies across the entire tropical Pacific between 10°N and 20°N, maximizing in the maritime continent. This is consistent with a southward shift of the ITCZ, as discussed by Donohoe et al. (2014). The presence of cloud cover tends to reduce the thermal emission from the atmosphere, having a larger impact than the changing albedo, producing a positive energy anomaly (L'Ecuyer et al., 2019). The absence of clouds increases the thermal emission, producing a negative radiative anomaly. These features combined are representative of an anomalously southward ITCZ. Furthermore, a southward shifting AHT has been associated with increasing northward AHT as the tropical overturning shifts with the location of deep convection, modulating the location of the greatest poleward transport.

Lastly, this enhanced tropical AHT across 10°N is also associated with higher latent heat fluxes (out of the ocean) both in the eastern tropical Pacific and along 10°N. This represents a loss of heat from the ocean to the atmosphere, cooling the ocean surface through evaporation. This also implies increased precipitation. Back and Bretherton (2005) demonstrate the positive relationship between evaporation and ITCZ activity, describing the close relationship between surface evaporation anomalies, increased moisture convergence, larger convective updrafts, and greater MSE exports to close the energy budget. This sequence of processes is consistent with the results presented here, with elevated tropical latent heat fluxes (especially in the East Pacific) being associated with enhanced poleward AHT (zonal mean MSE exports).

The goal of this research is to examine the meridional variability in the energetic budget associated with atmospheric energy transport and the agreement between reanalysis and observations. We have demonstrated clear agreement between observations and reanalysis while describing the differing importance of energy budget components in modulating the monthly atmospheric energy transport. The latent heat flux and the atmospheric tendency are identified as the key components of midlatitude and polar AHT, while radiative gradients in atmospheric heating are only dominant in the tropics. This work contributes to the growing body of research attempting to close the atmospheric energy budget from observations and we demonstrate that monthly variability in observations and the relative importance of components are in agreement. This analysis examined the monthly mean fluxes into and out of the atmosphere consistent with energy transport across a latitude, however, the mechanisms that moved the energy across each latitude remain unexamined. Identifying the circulation anomalies that take energy from regions of excess to deficit is a crucial outstanding research question to complete this understanding.

Chapter 5

Synthesis

Three distinct research questions have been presented in this dissertation, each examining differing aspects of Earth's energy budget and our ability to accurately record trends and variability. Presented below is a summary of the key conclusions and perspectives that have been discussed in answering each research question.

1. How are the polar, top-of-atmosphere radiative budgets changing in the observed satellite record?

- Over the last two decades, solar absorption in the Arctic has increased at a rate of approximately 1 W m^{-2} dec^{-1}. Antarctic solar absorption has increased at a rate of 0.6 W m^{-2} dec^{-1}, however, this trend is not significant but emergence into a statistically significant trend is expected within a yew years.
- Arctic thermal emission is also increasing at approximately 1 W m^{-2} dec^{-1}, seemingly compensating the increased solar absorption. In Antarctica, thermal emission is remaining unchanged with no trend in the TOA emission.
- The annual variability in Arctic solar absorption describes over two thirds of the variability in TOA thermal emission. In Antarctica, less than a third of the thermal emission variance is described by solar absorption.

- Clouds mask the underlying trends in the Arctic, reducing the trends in both solar absorption and thermal emission. However, the impact of cloud masking on the surface reflective properties in the Arctic far exceed their modulation of the TOA thermal emission. Despite this difference, the resultant all-sky trends with the presence of clouds are remarkably similar.

- Solar absorption trends are restricted to regions of sea ice loss in both the Arctic and Antarctica. In regions of increasing sea ice coverage, solar absorption is reducing. Thermal emission trends in the Arctic are occurring across the entire domain and not restricted to regions of ice loss.

- The Arctic appears to be behaving like a *shallow bathtub*, where increasing solar absorption is warming the ocean surface which is then being emitted back to space. Antarctica however, is acting like an *energy sink*, where increasing energy from solar absorption is being sequestered into the Southern Ocean, increasing the ocean heat content while leaving the sea surface and atmospheric temperatures relatively unchanged. In other words, the albedo feedback is not occurring as expected in Antarctica - the reducing sea ice is lowering the albedo and increasing solar absorption, but this is not increasing surface temperatures.

- These observations are from records over the last 20 years, during a transient period in Earth's climate. To what extent these states and trends remain in the future is unknown. Furthermore, this analysis only assessed the TOA radiative receipts due to the precision of these observations. Additional analysis of the changing sources and sinks of energy requires closure of the energy budget, which observations are currently unable to do.

- This analysis demonstrates the rapid and increased uptake of energy by the Southern Ocean, which results in a differing response to sea ice loss in Antarctica than in the Arctic. The balance between absorbed solar radiation and emitted longwave radiation defines the climate of our planet and provides a robust record of how these are changing is crucial for validating climate models and their projections.

2. Can the global atmospheric heat transport be constrained with observations of Earth's energy budget?

- State-of-the-art data sets were used to calculate Earth's atmospheric energy budget and subsequently, the poleward energy transport. All observational estimates of the atmospheric energy budget underestimate the energetic input into the atmosphere in the tropics compared to reanalysis, attributed to underestimated latent heat fluxes. Observations are substantially underestimating the amount of evaporation occurring in the tropics compared to reanalysis.

- This minimum in the tropical atmospheric energy budget, paired with positive biases in observed Northern Hemisphere sensible heat fluxes results in smaller meridional gradients in the observed atmospheric energy budget.

- The lower gradient in the Northern Hemisphere observed atmospheric energy budget results in a substantially lower (over 1 PW) annual mean AHT compared to reanalysis. In the Southern Hemisphere, the observed AHT also underestimates the annual mean reanlsysis AHT, however by less than 1 PW. All reanalysis AHT derivations are within 0.5 PW of each other.

- Through analysis of the seasonal cycle, this underestimation of the AHT maximizes in the summer time for each hemisphere. This is especially prevalent in the Northern Hemisphere summer, between May and July, where the monthly mean observed AHT can be over 3 PW lower than reanalysis.

- Despite these differences in the mean state, the monthly variability has good agreement between reanalysis and observations. In the midlatitudes, observed AHT has correlations of up to 0.8 with reanalysis. The reanalysis products have monthly correlations of 0.95 with each other. In the tropics, the correlations between reanalysis and with observations reduce significantly to 0.5.

- In the decade-long time series of AHT, the observed AHT appears to have non-stationarity in the magnitude and direction of the anomalies while the reanalysis monthly anomalies are much more homogeneous, exhibiting stationarity.

- There remains substantial disagreement between observations and reanalysis global turbulent heat fluxes, inhibiting the calculation of an accurate surface energy budget and consequently, the mean atmospheric energy budget. There is evidence that reanalysis surface heat fluxes may be representative of the true flux and that observations remain erroneous. Improving our ability to accurately observe Earth's surface energy budget should remain a priority.

- There are limited records of the global vertically integrated moist static energy, prohibiting independent calculations of the atmospheric energy tendency. Further efforts to observe the vertically resolved MSE, such as through geostationary sounders, should also remain a priority for providing closure in Earth energy budget observations.

3. What is the energetic expression of monthly atmospheric heat transport variability?

- Through STL decomposition, long term records of monthly atmospheric heat transport anomalies were developed with agreement between observations and reanalysis. This time series decomposition was required to remove low frequency variability along with nonstationarity of the seasonal cycle that differs between data products.

- Anomalous monthly AHT is confined to a meridional extent of approximately $\pm 15°$ - heat transport through 60°S is only loosely related to heat transport across 30°S. The energetic sources and sinks associated with heat transport are therefore confined to a relatively close dipole either side a heat transport anomaly.

- While the net radiative budget is the largest component of the atmospheric energy budget, it has low interannual variability compared to the latent heat flux and the atmospheric energy tendency. The amount of energy gained and lost through radiation is highly stable for one year to the next and so does not contribute substantially to anomalies in the atmospheric energy budget.

- Within the midlatitudes (30-40°), the vast majority of energy that flows poleward comes from enhanced tropical latent heat fluxes. On the poleward side of the anomalous transport, energy is lost through all components (sensible, latent, radiative, and the tendency) approximately equally.

- With the exception of the deep tropics, radiative anomalies are only associated with atmospheric heat transport on the poleward side. This demonstrates that positive energy gains through radiation (such as reduced albedo) do not have a significant relationship with monthly poleward heat transport variability. Either side 10°N, radiative anomalies do contribute to positive and negative energetic anomalies leading it to having a dominant role in heat transport variability.

- Within the polar regions, variance in the atmospheric energy tendency alone describes over 50% of the heat transport variability, with the latent heat and tendency combined accounting for over 75% of the variance. The convergence of heat transport into the polar regions results in direct changes to the energy storage within the atmosphere. Only in regions of open ocean do the turbulent heat fluxes play a role in modulating the poleward heat transport.

- Distinct regions of atmospheric energy exchange are identified for heat transport across different latitudes. To ensure energetic closure, energy must be flowing from regions of net gain to regions of net loss. It would be worth for future analysis to examine the physical mechanisms that undertake this energy exchange and how these may vary between hemispheres and across latitudes.

The three research questions presented herein demonstrate how Earth's radiative budget is being modulated in our changing climate, assess our ability to accurately observe the atmospheric energy budget through the perspective of meridional heat transport, and characterize the energy budget components responsible for monthly atmospheric heat transport variability. State-of-the-art observational products are critically assessed along with identifying limitations to our observing systems. This work together provides a new benchmark for our current understanding of Earth's atmospheric energy budget.

Appendix A

Supplementary Material for Chapter 2

Region		All Sky Trend Wm^{-2} dec^{-1}	All Sky Std Wm^{-2}	Clear Sky Trend Wm^{-2} dec^{-1}	Clear Sky Std Wm^{-2}
All Arctic	ASR	0.98±0.69	1.07	2.02±0.88	1.69
	OLR	0.94±0.55	0.92	1.26±0.57	1.07
	Net	0.04±0.47	0.61	0.77±0.61	0.93
Arctic Ocean	ASR	1.53±0.98	1.58	3.14±1.18	2.48
	OLR	1.23±0.62	1.11	1.67±0.67	1.35
	Net	0.30±0.74	0.97	1.47±0.83	1.41
Arctic Land	ASR	0.59±0.63	0.90	1.22±0.76	1.24
	OLR	0.73±0.56	0.85	0.96±0.61	0.99
	Net	-0.14±0.43	0.56	0.26±0.57	0.76
All Antarctic	ASR	0.59±0.64	0.91	0.90±1.02	1.43
	OLR	-0.07±0.52	0.67	-0.29±0.39	0.54
	Net	0.66±0.53	0.80	1.18±0.87	1.34
Antarctic Ocean	ASR	0.64±0.92	1.25	1.15±1.49	2.06
	OLR	-0.07±0.50	0.65	-0.27±0.34	0.47
	Net	0.70±0.73	1.04	1.42±1.24	1.83
Antarctic Land	ASR	0.51±0.38	0.59	0.43±0.48	0.67
	OLR	-0.09±0.62	0.81	-0.32±0.67	0.88
	Net	0.60±0.50	0.74	0.76±0.83	1.17

Table A.1: Trends and standard deviation of ASR, OLR, and net energy in Wm^{-2} for the Arctic and Antarctic for both all sky and clear sky with associated 95% confidence interval using Student's-t distribution.

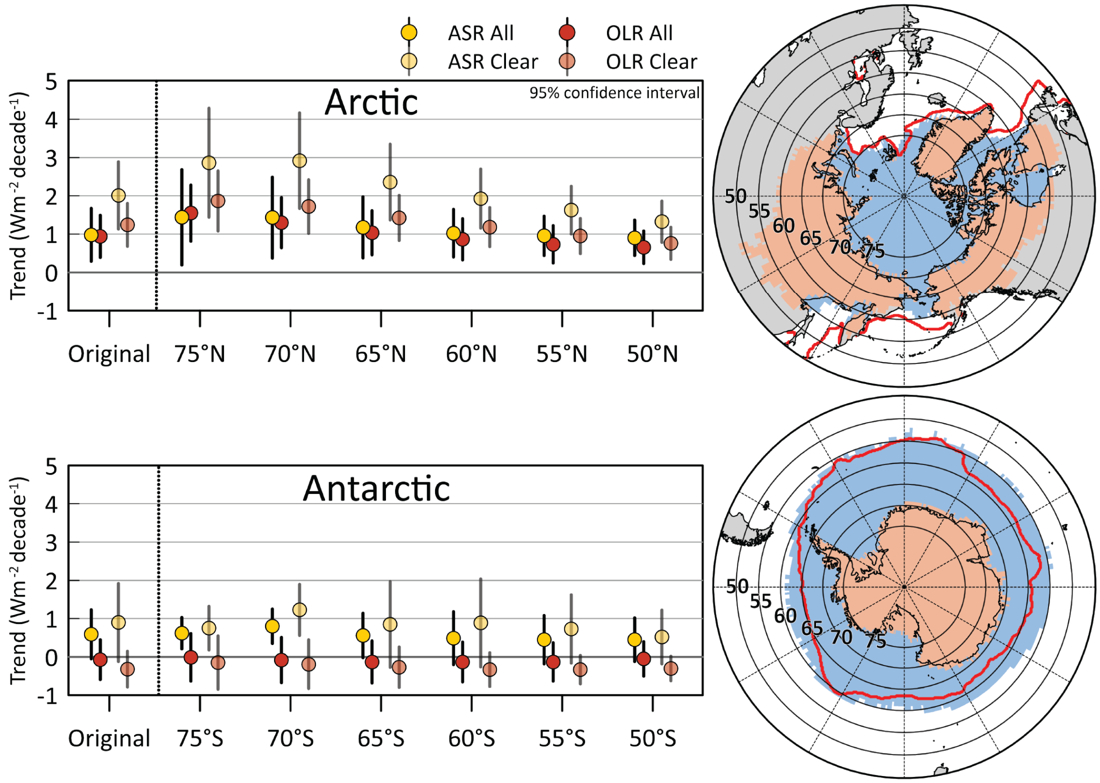

Figure A.1: Sensitivity test of the geographic region used in this study on ASR and OLR trends (for all- and clear-sky). The colored (orange and blue) region in the maps represent the 'original' region that is used in this study, defined as where the climatological mean annual 2-m air temperature is below freezing (as defined in Figure 2). The original trends are compared to trends calculated from polar regions bounded by differing zonal extents starting from 75°N/S and extending out to 50°N/S at 5° intervals. The vertical bar represents the 95% confidence interval of the trend and when this line crosses zero, the trend is not statically significant. For both the Arctic and Antarctic, the trends increase when the most confined region is considered (poleward of 75°N/S), emphasizing the effects of local isolated trends. It is apparent that by 65°N/S the trends stabilize and including more area equatorward of 65°N/S does not influence the trend, demonstrating that the most impactful changes to these radiative trends are occurring within the polar regions.

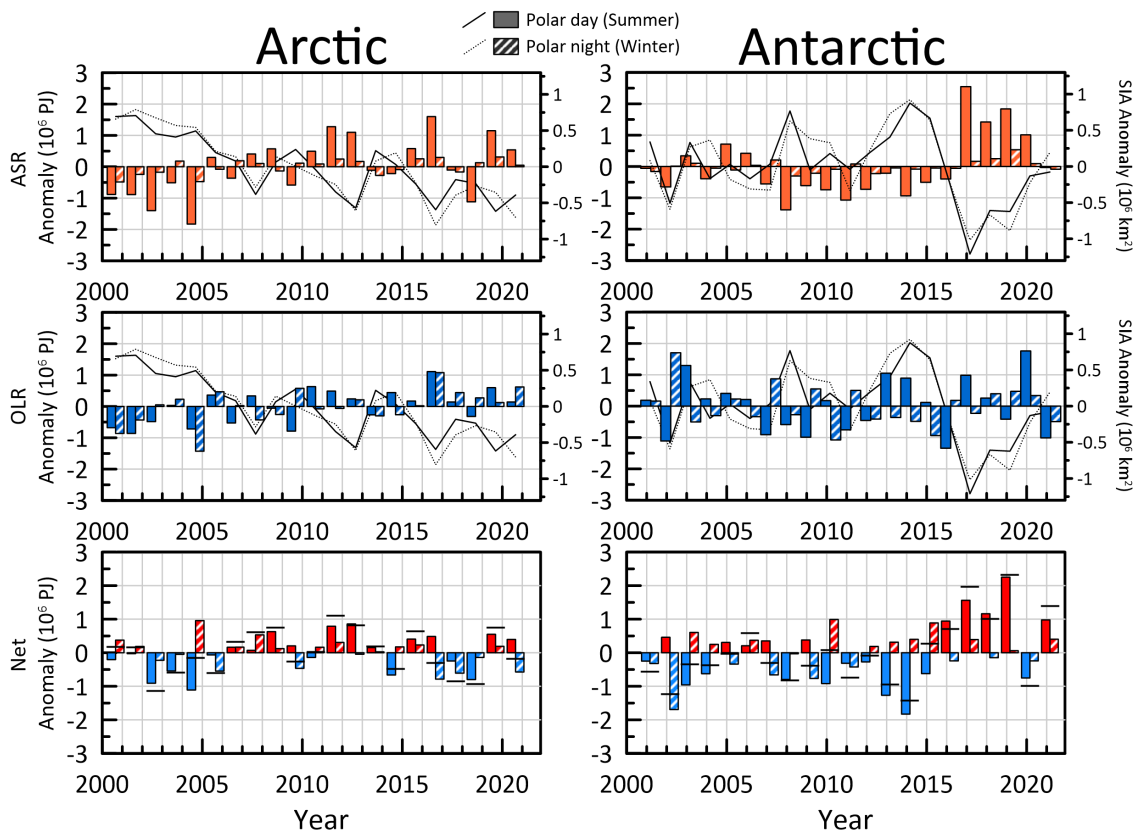

Figure A.2: Timeseries of the TOA anomalies of absorbed shortwave radiation (ASR), outgoing longwave radiation (OLR) and the net radiative energy (Net) for all-sky conditions in both the Arctic and Antarctic. Timeseries shown at half-yearly intervals for summer (solid color) and winter (striped). The half-yearly mean sea ice area is shown with solid line (summer) and dotted line (winter) on the secondary y-axis. The horizontal lines on the net anomaly show the annual sum of the summer and winter anomalies.

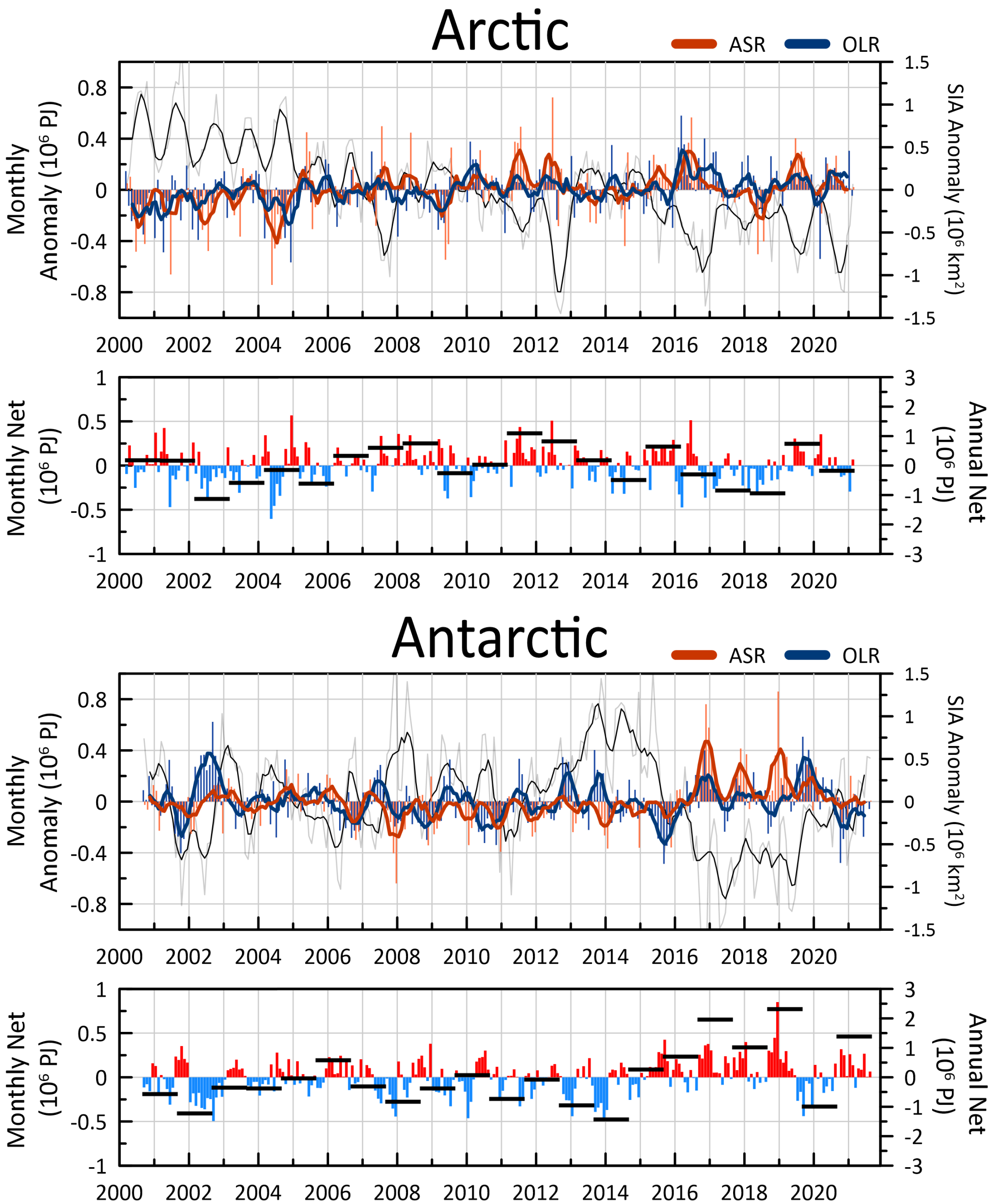

Figure A.3: Timeseries of the TOA anomalies of absorbed shortwave radiation (ASR), outgoing longwave radiation (OLR) and the net radiative energy (Net) for all-sky conditions in both the Arctic and Antarctic at monthly time scales. The monthly mean sea-ice cover is shown with the gray line with a 6-month moving average plotted in black. The horizontal lines on the net anomaly show the annual sum of the monthly anomalies.

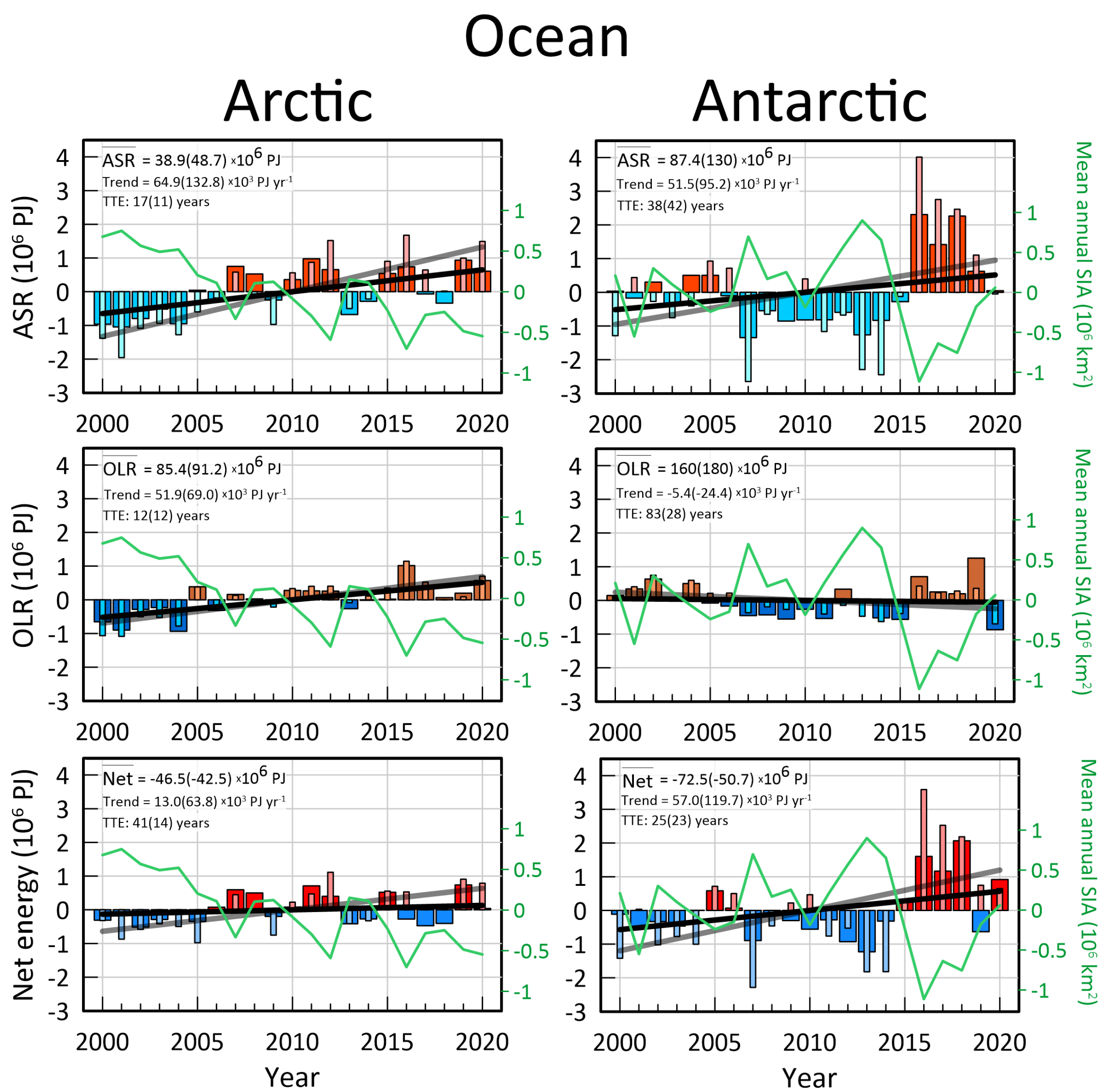

Figure A.4: Timeseries of the TOA anomalies of absorbed shortwave radiation (ASR), outgoing longwave radiation (OLR) and the net radiative energy (Net) for all-sky (thick bars) and clear-sky (thin bars) conditions situated over ocean. Linear regression shown with the black and gray lines for all- and clear-sky respectively. The annual mean sea-ice cover is shown with green line on the secondary y-axis. The mean and trend in shown in the upper left with the time-to-emergence in the lower right (clear-sky in parentheses).

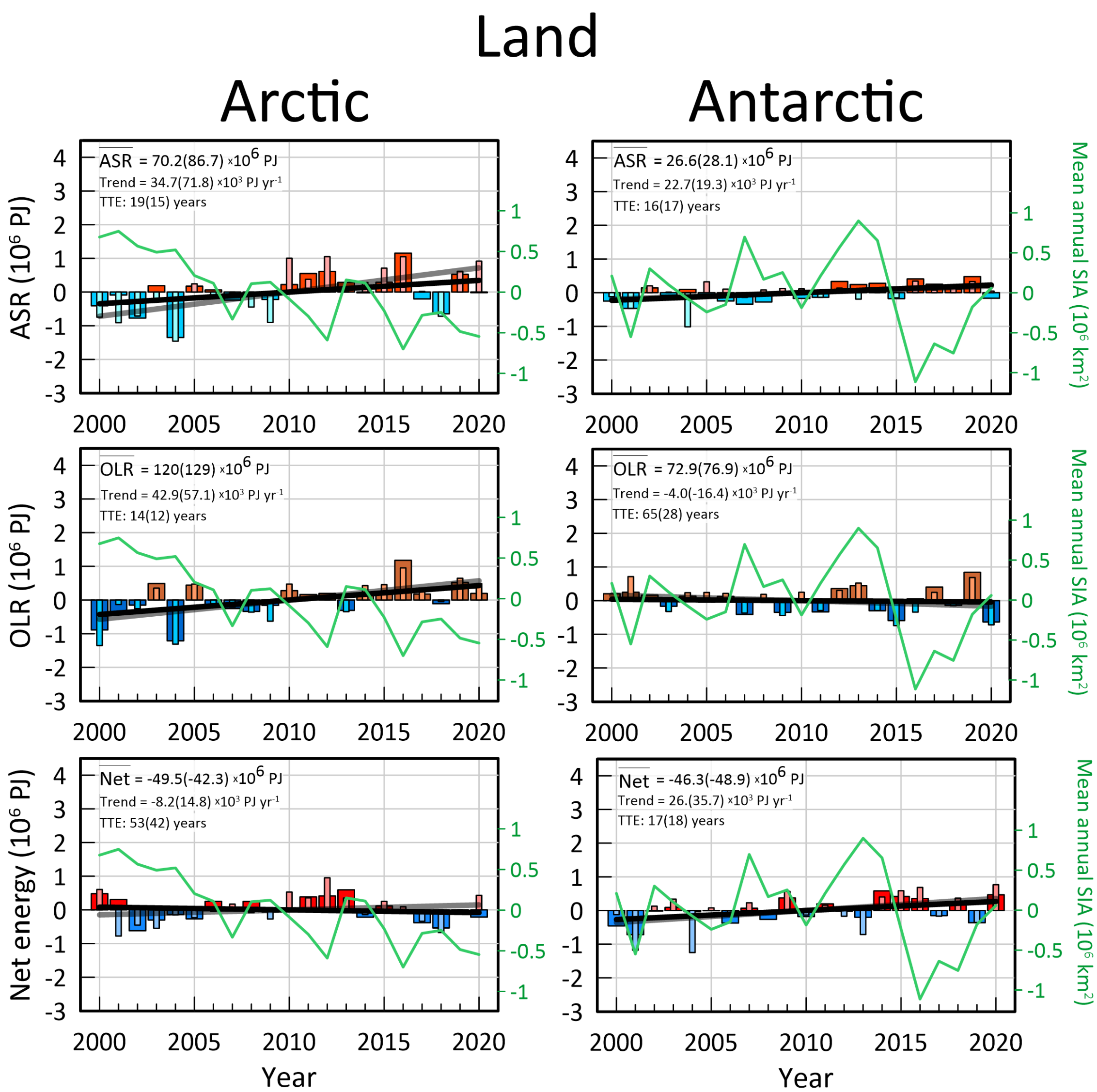

Figure A.5: Timeseries of the TOA anomalies of absorbed shortwave radiation (ASR), outgoing longwave radiation (OLR) and the net radiative energy (Net) for all-sky (thick bars) and clear-sky (thin bars) conditions situated over land. Linear regression shown with the black and gray lines for all- and clear-sky respectively. The annual mean snow cover is shown with green line on the secondary y-axis in the Arctic for available years. The mean and trend in shown in the upper left with the time-to-emergence in the lower right (clear-sky in parentheses).

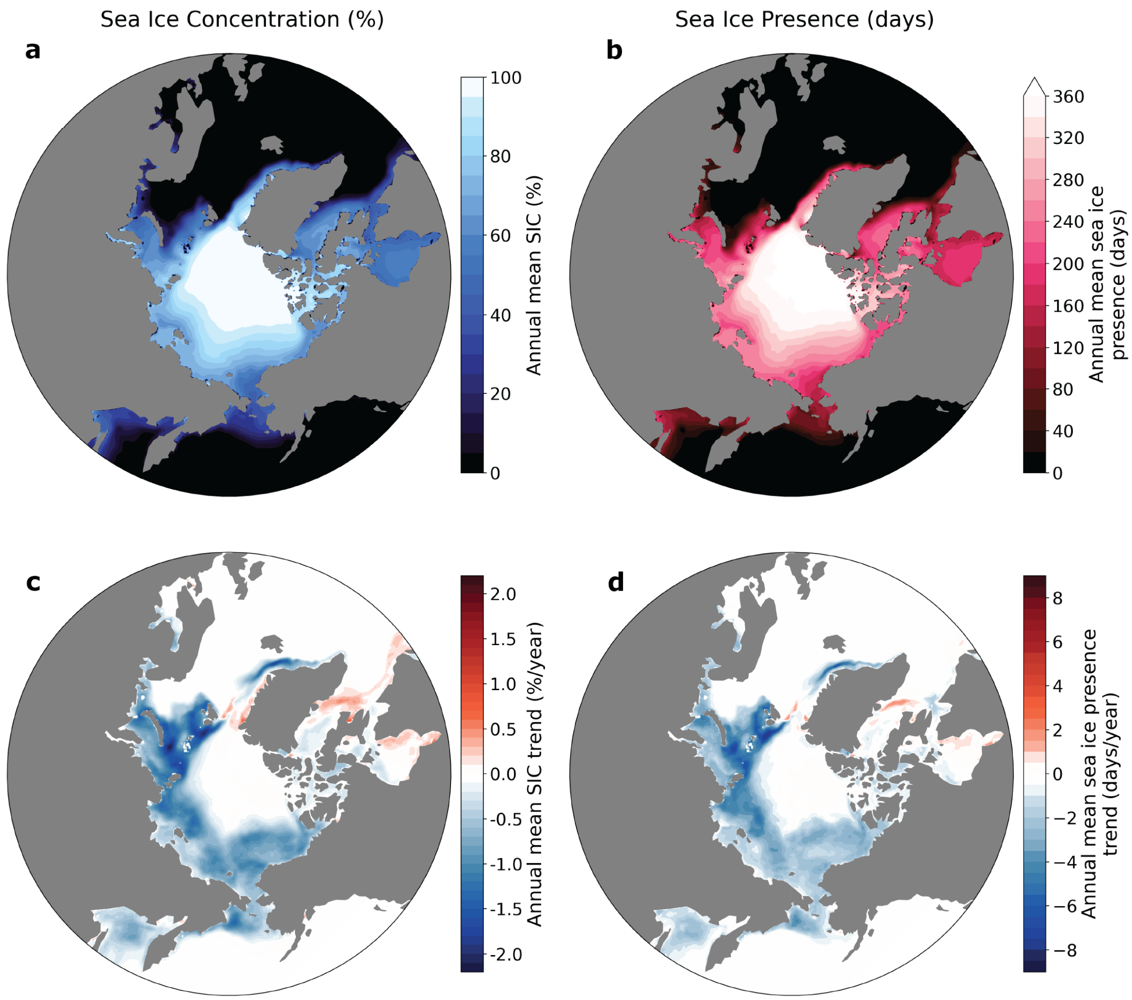

Figure A.6: Annual mean and trends of Arctic sea ice concentration (SIC; a and c) and presence (b and d). Mean annual SIC is calculated as the annual mean of daily mean SIC where individual cells less than 15% SIC set to zero due to uncertainties in the satellite record. Sea ice presence is calculated as the number of days more than 15% SIC occurs, considered as a measurable amount of sea ice present from the satellite record. Trends are calculated from linear regression for each grid cell.

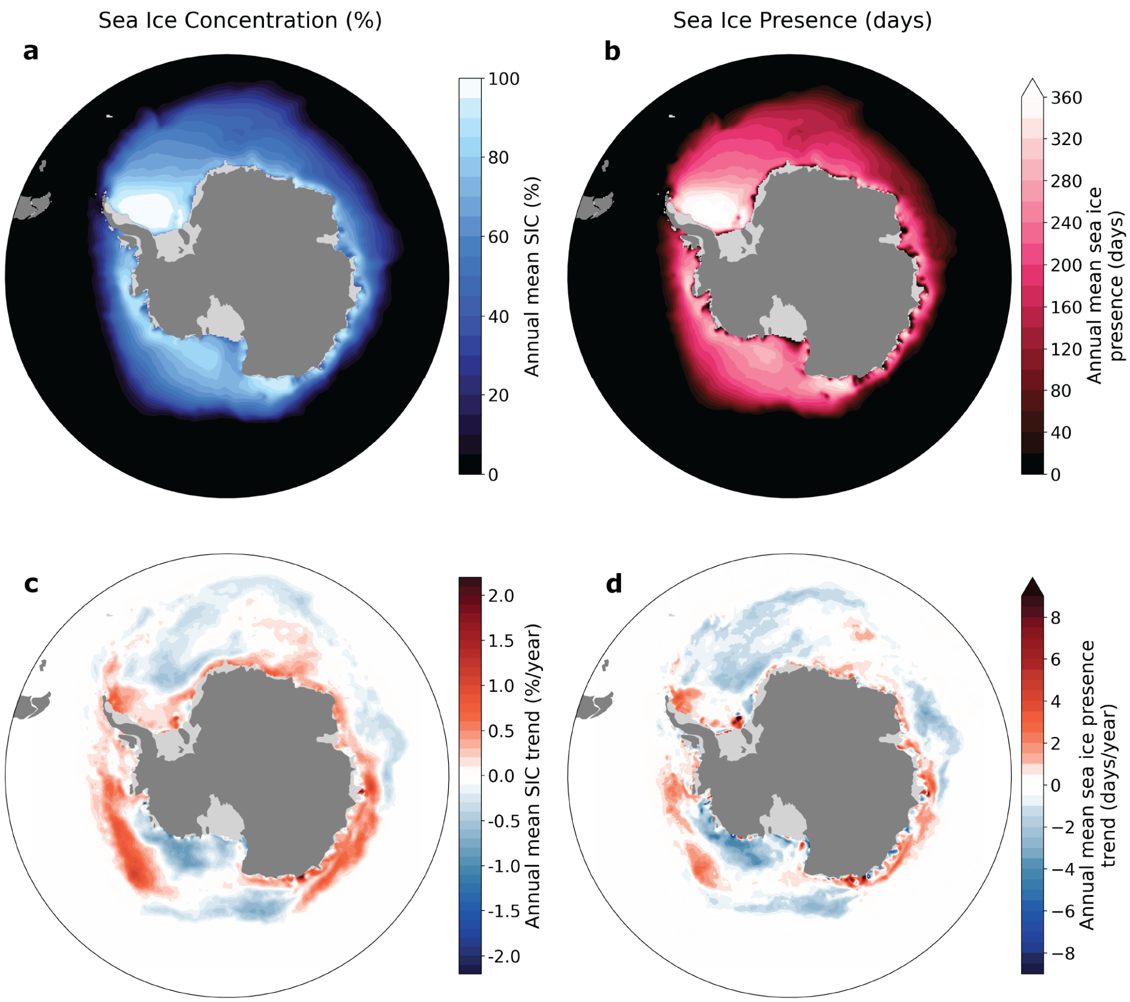

Figure A.7: Annual mean and trends of Antarctic sea ice concentration (SIC; a and c) and presence (b and d). Mean annual SIC is calculated as the annual mean of daily mean SIC where individual cells less than 15% SIC set to zero due to uncertainties in the satellite record. Sea ice presence is calculated as the number of days more than 15% SIC occurs, considered as a measurable amount of sea ice present from the satellite record. Trends are calculated from linear regression for each grid cell.

Appendix B

Supplementary Material for Chapter 3

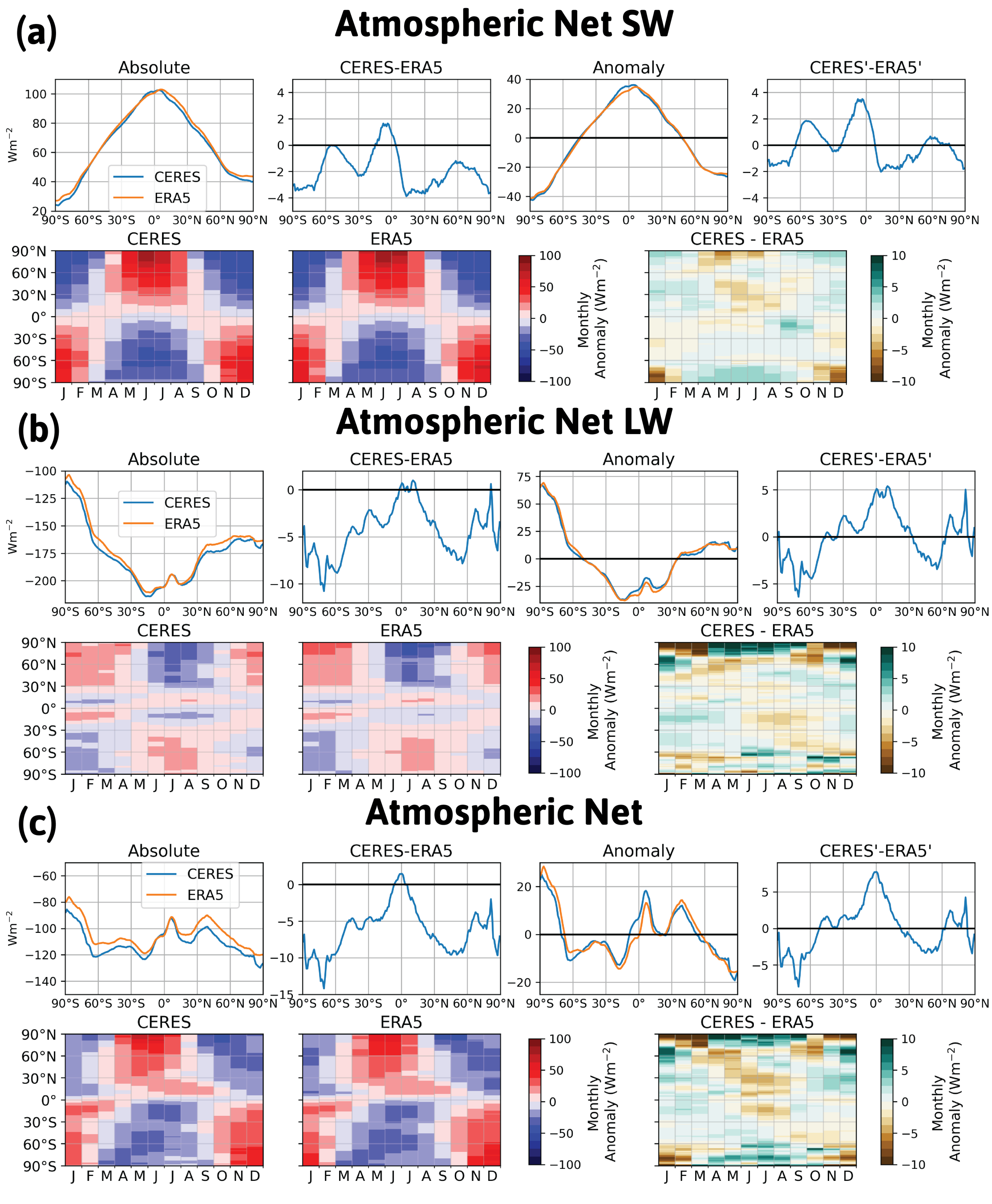

Figure B.1: Comparison of atmospheric radiative budgets between CERES EBAF 4.2 and ERA5, shown for the net (a) shortwave, (b) longwave, and (c) total radiation. Absolute difference and bias-corrected (anomaly) differences are plotted along with the seasonal cycle.

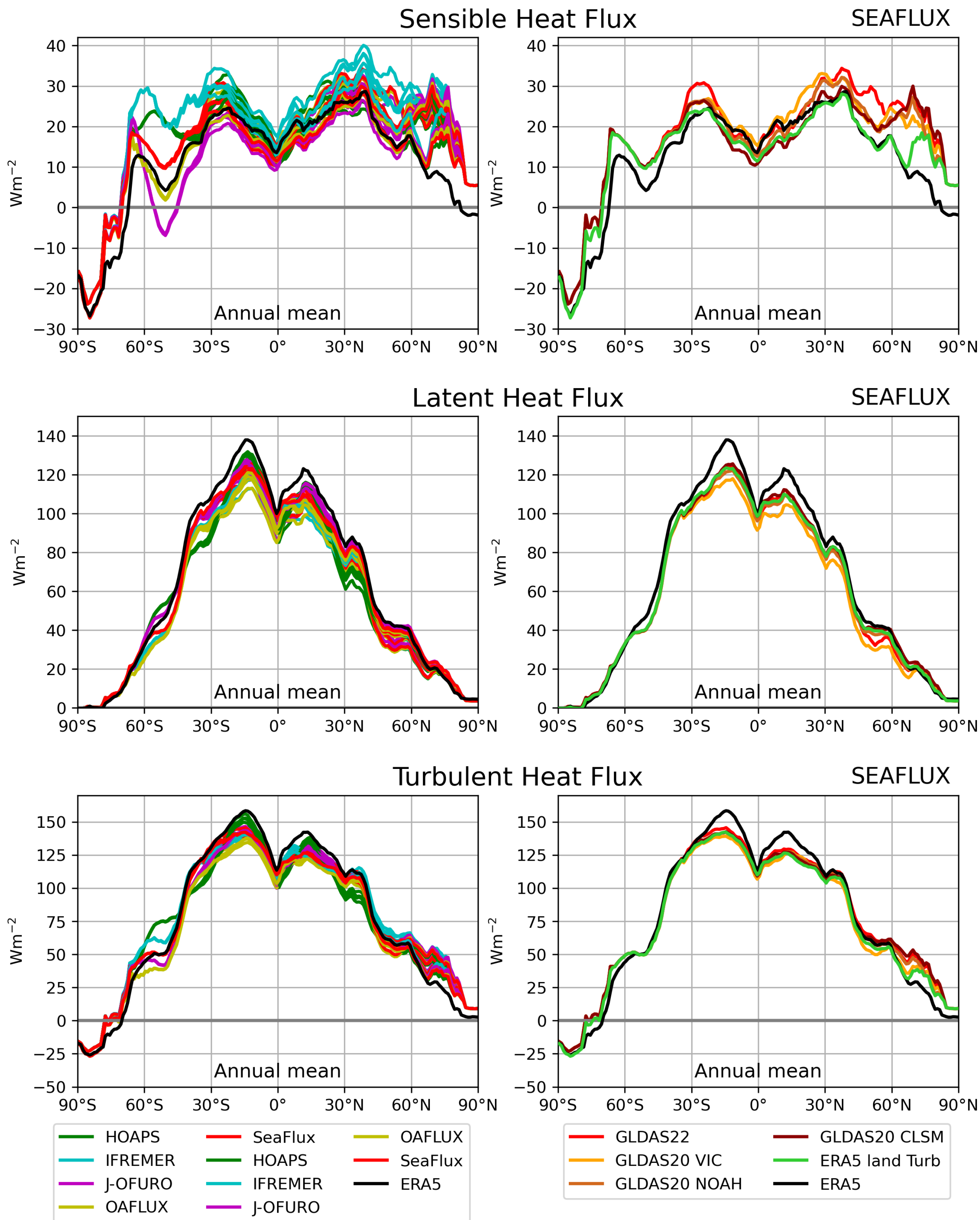

Figure B.2: Testing the dependence of the zonal mean turbulent heat fluxes on the choice of GLDAS land surface model version. (left) Every observation product is plotted four time for the four GLDAS versions and ERA5 land surface turbulent heat flux. (right) Only SeaFlux is shown with the four GLDAS versions along with the ERA5 land surface turbulent heat flux identified with color.

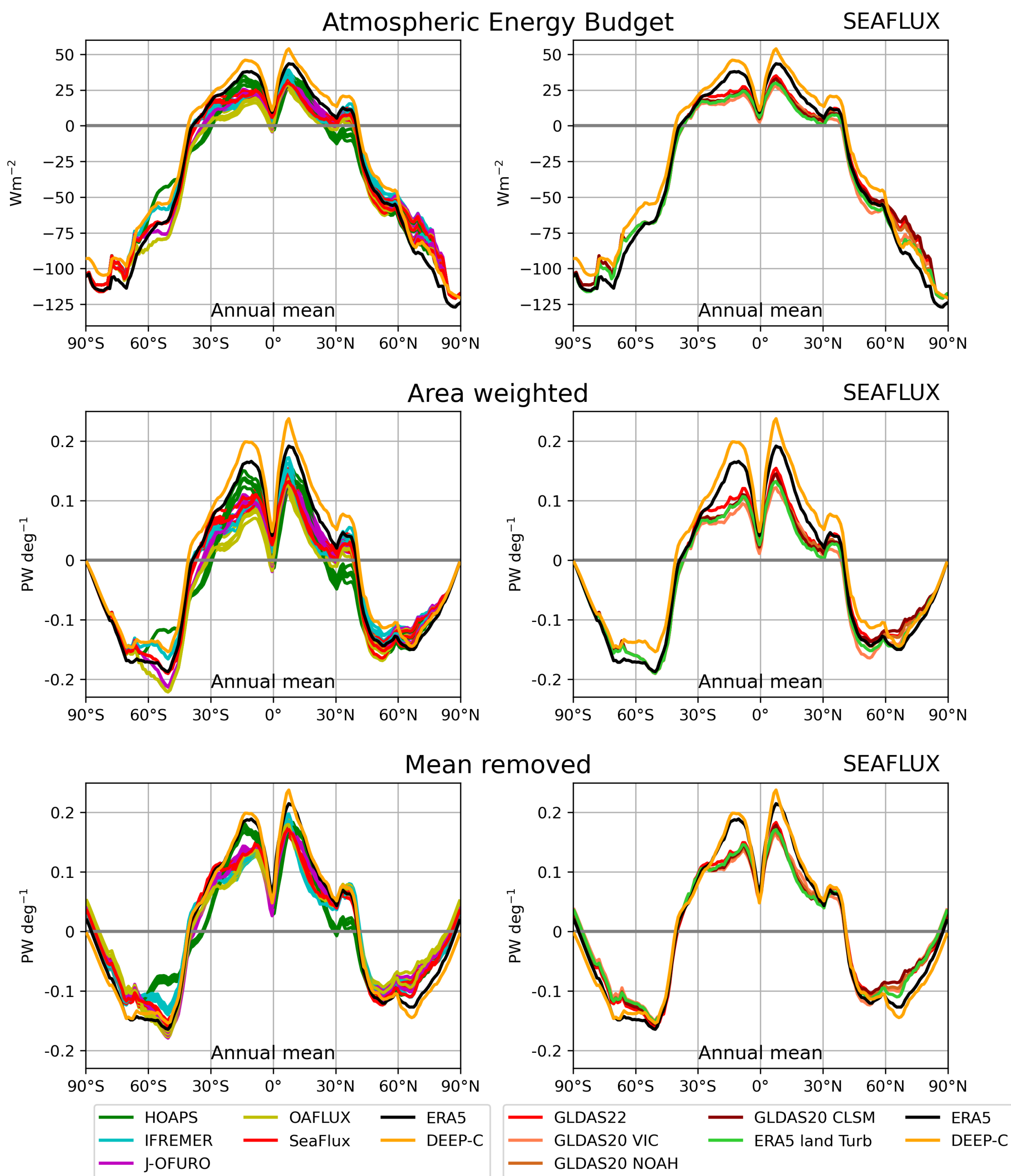

Figure B.3: Same as Supp. Figure B.2, but for the net atmospheric energy budget.

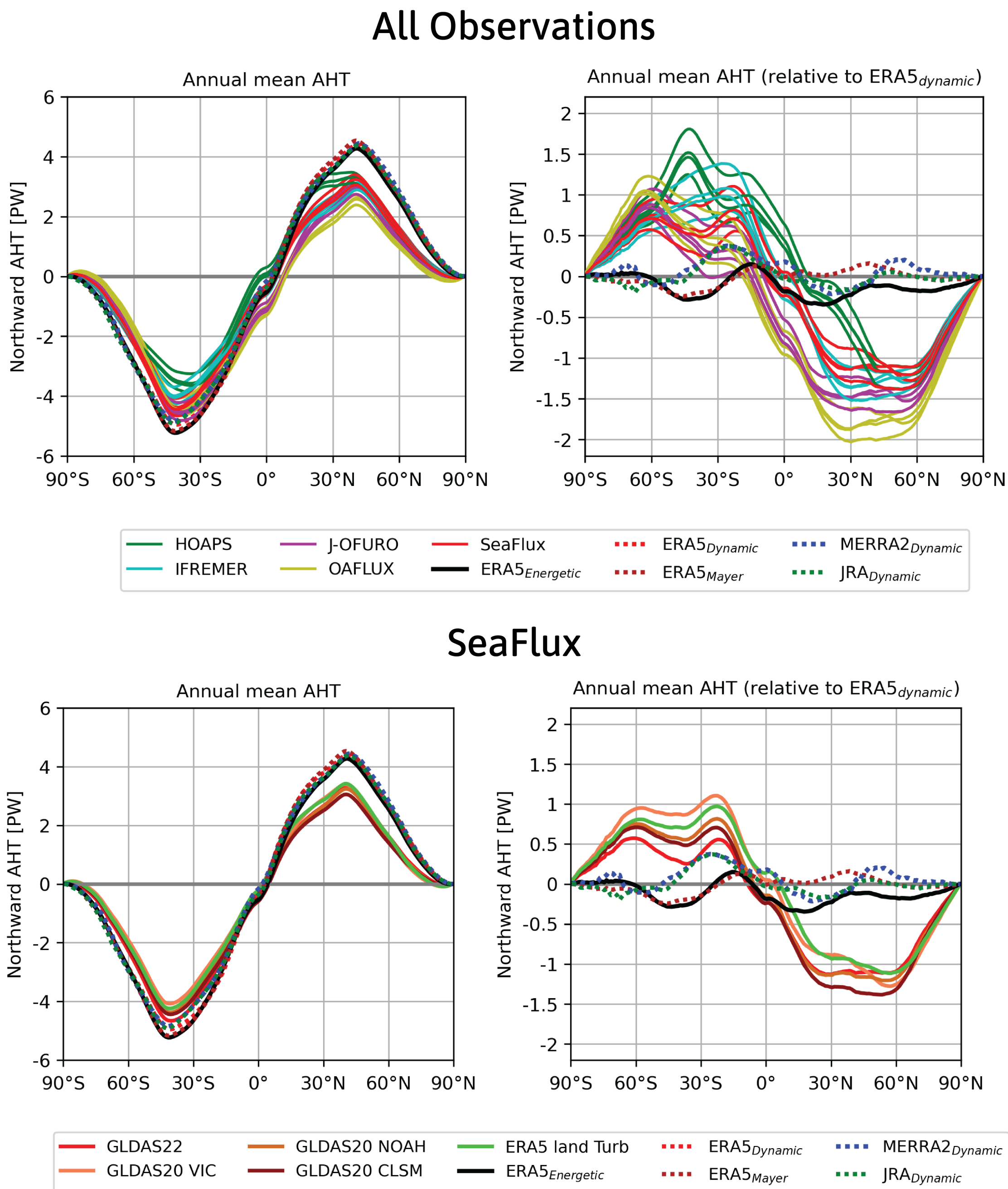

Figure B.4: Same as Supp. Figures B.2 and B.3, but for the annual mean AHT.

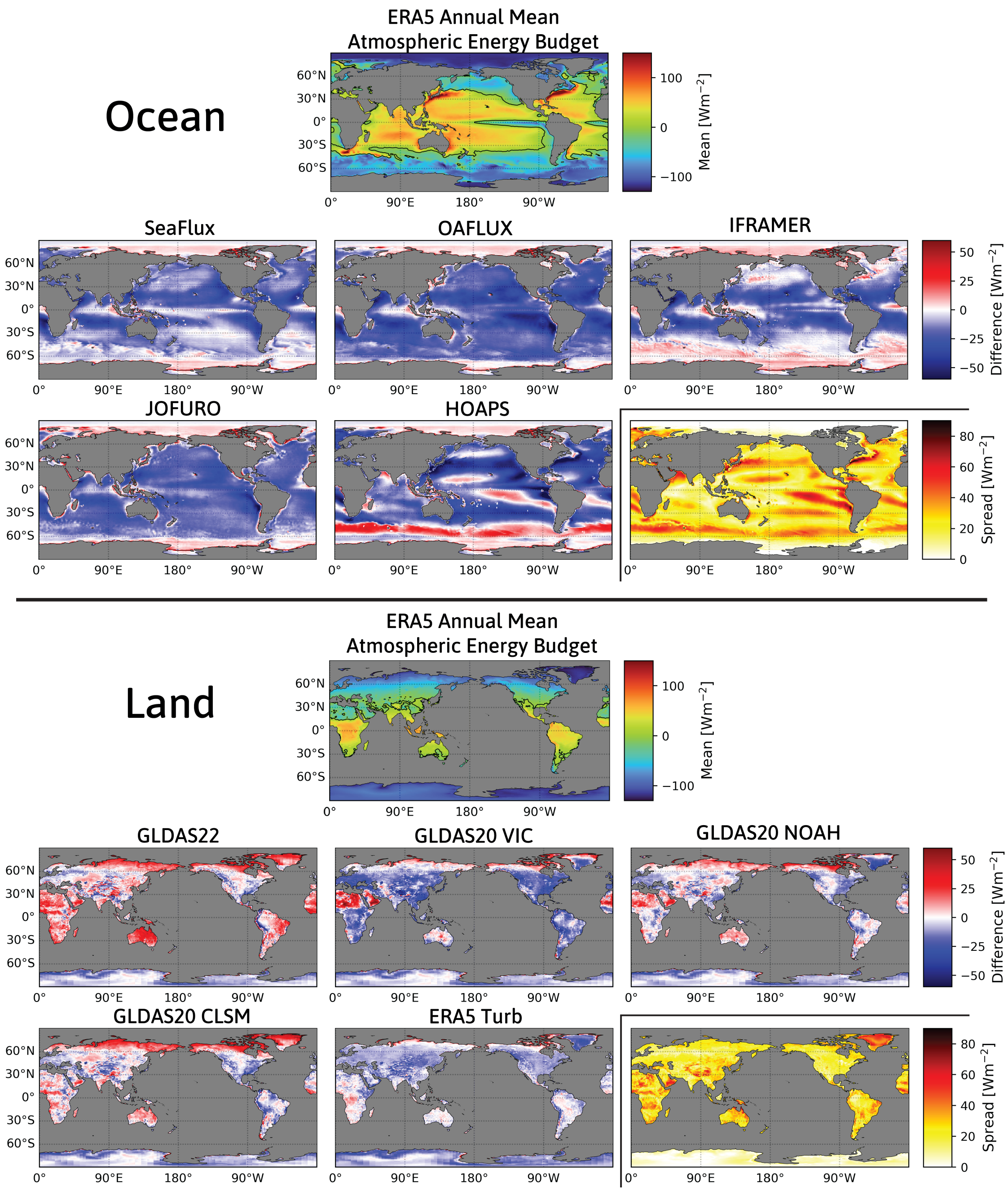

Figure B.5: The sensitivity of the annual mean atmospheric energy budget to data products over the ocean (upper) and over land (lower). The energy budget is closed with the addition of CERES-EBAF radiative fluxes.

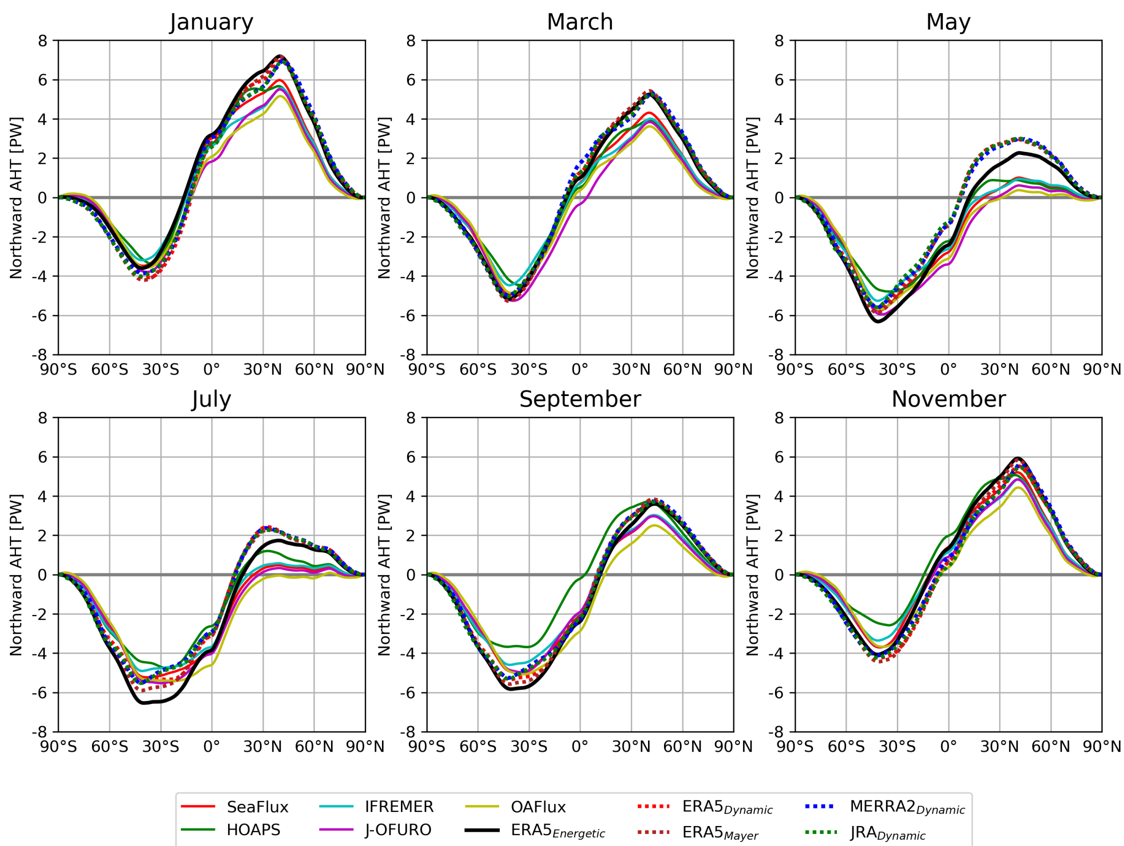

Figure B.6: Monthly AHT as calculated from reanalysis and the observations products through the dynamic (dotted lines) and energetic (solid lines) formulation. Monthly means shown for every second month.

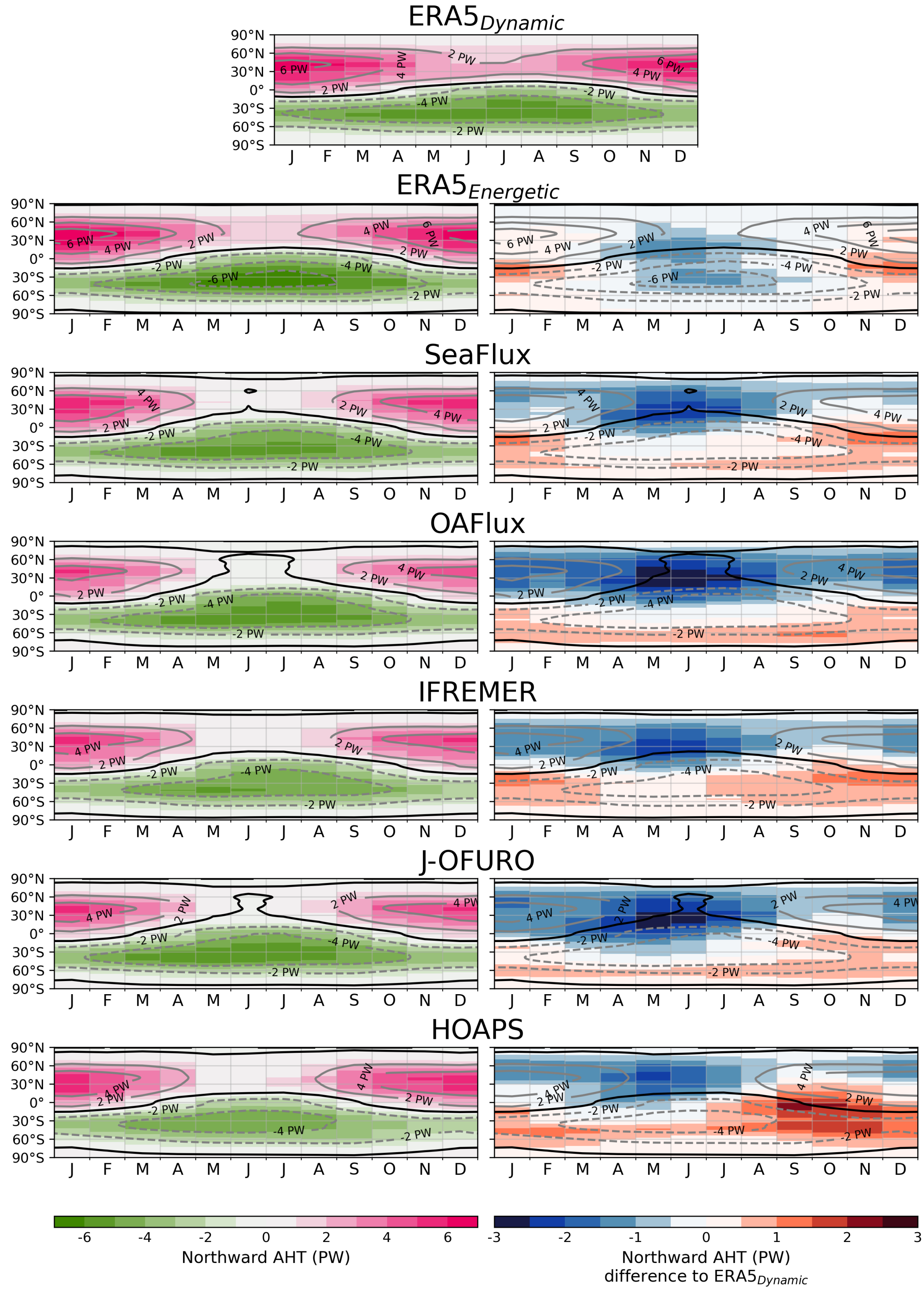

Figure B.7: Seasonality of northward AHT in all energetic AHT calculations and their difference to ERA5$_{\mathrm{dynamic}}$.

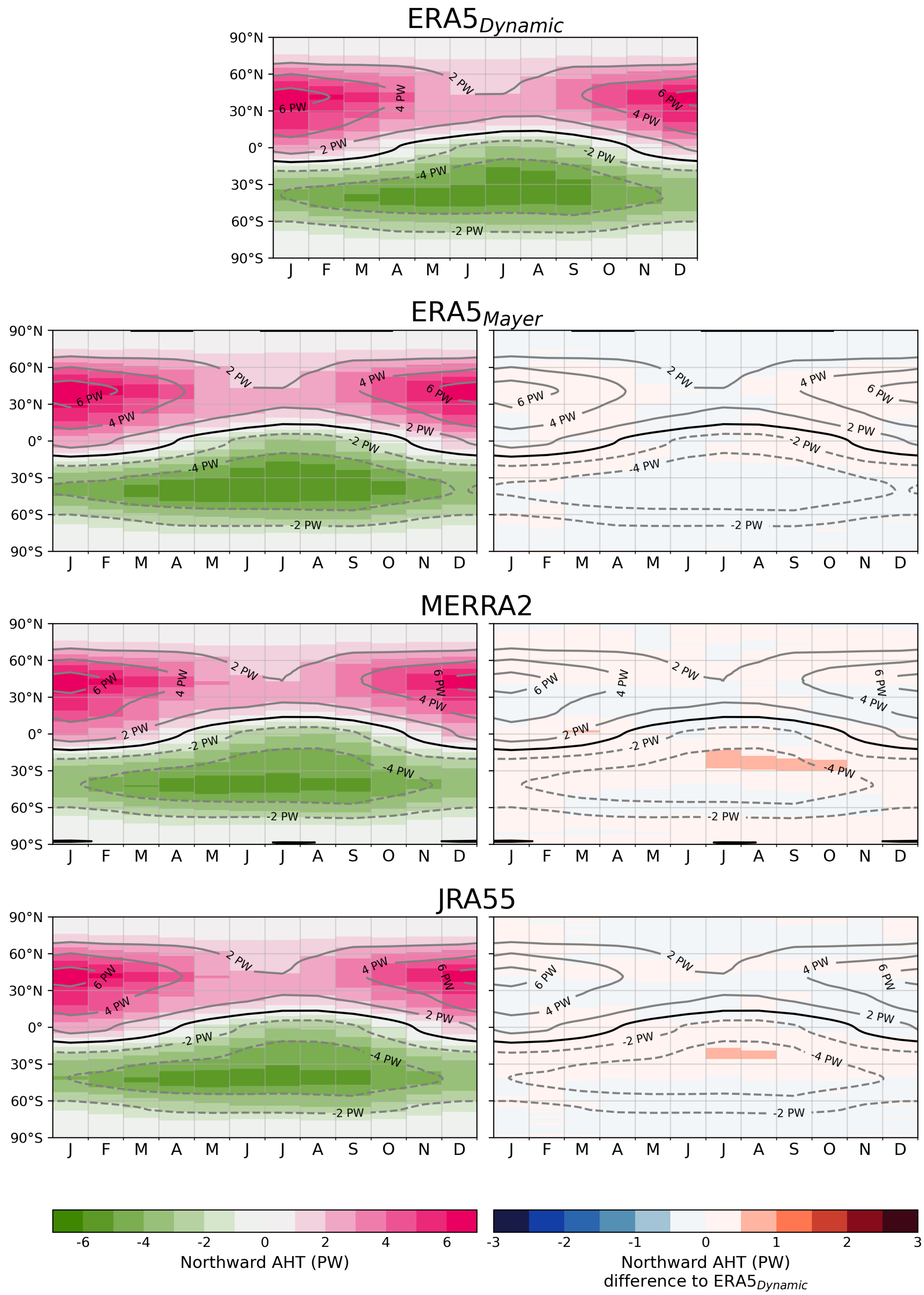

Figure B.8: Seasonality of northward AHT in all dynamic AHT calculations and their difference to ERA5$_{\mathrm{dynamic}}$.

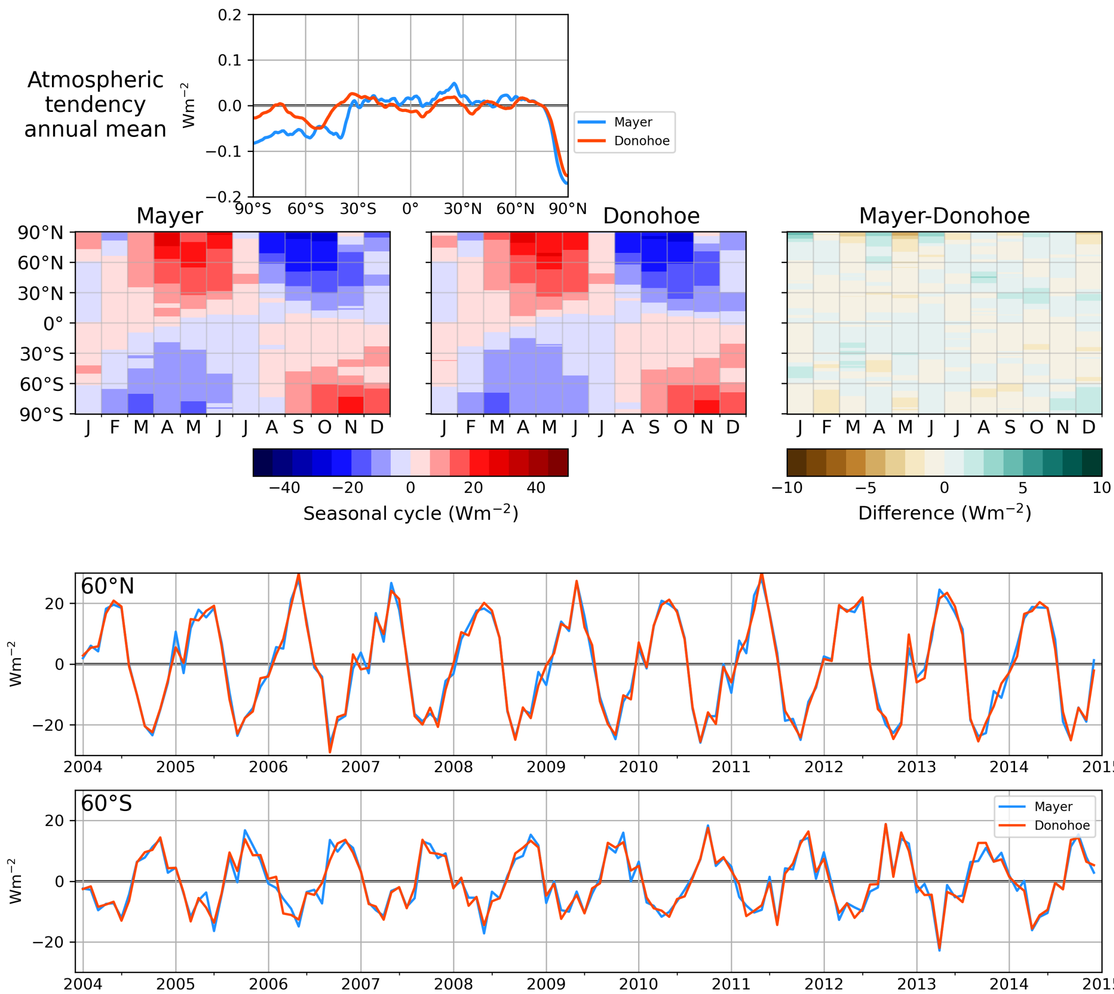

Figure B.9: The difference between the Mayer et al. (2017) and Donohoe et al. (2020) atmospheric tendency terms. The annual mean, seasonality and example time series at 60°N/S are shown.

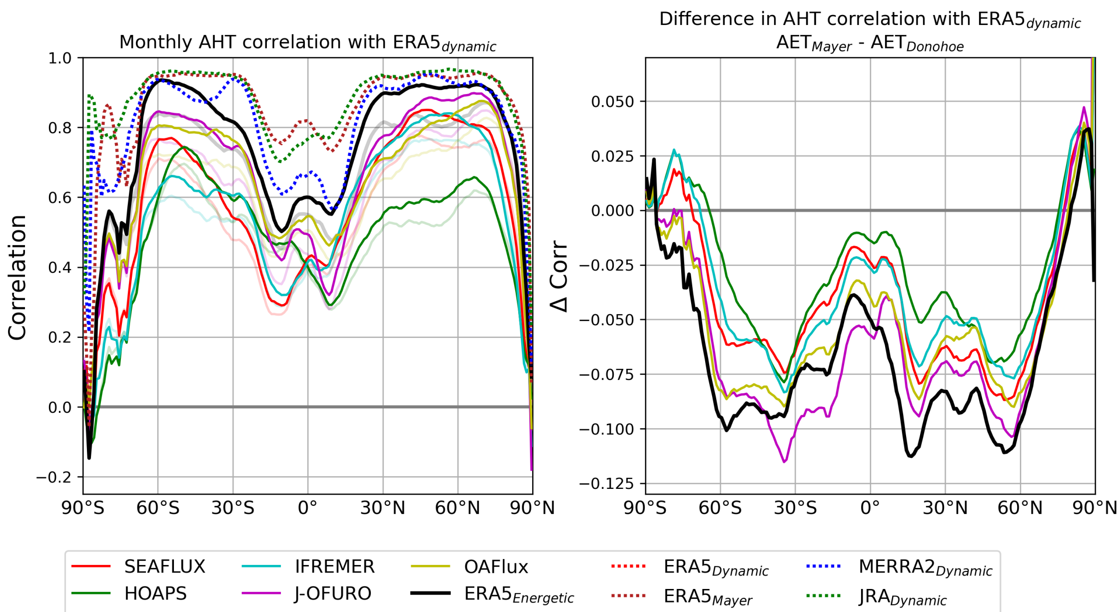

Figure B.10: (left) Correlation of monthly AHT anomaly for each latitude band utilizing the Donohoe et al. (2020) tendency in bold with the Mayer et al. (2017) shown with transparency. (right) The difference in correlation when using the Mayer et al. (2017) and Donohoe et al. (2020) tendency to derive energetic AHT.

Bibliography

AIRS, 2019: Aqua/AIRS L3 Monthly Standard Physical Retrieval (AIRS+AMSU) 1 degree x 1 degree V7.0. Greenbelt, MD, USA, Goddard Earth Sciences Data and Information Services Center (GES DISC), 10.5067/KUC55JEVO1SR.

Andersson, A., K. Fennig, C. Klepp, S. Bakan, H. Graßl, and J. Schulz, 2010: The Hamburg Ocean Atmosphere Parameters and Fluxes from Satellite Data – HOAPS-3. *Earth Syst. Sci. Data*, **2**, 215–234, https://doi.org/10.5194/essd-2-215-2010.

Armour, K. C., J. Marshall, J. R. Scott, A. Donohoe, and E. R. Newsom, 2016: Southern Ocean warming delayed by circumpolar upwelling and equatorward transport. *Nature Geoscience*, **9**, 549–555, https://doi.org/10.1038/NGEO2731.

Armour, K. C., N. Siler, A. Donohoe, and G. H. Roe, 2019: Meridional atmospheric heat transport constrained by energetics and mediated by large-scale diffusion. *Journal of Climate*, **32**, 3655–3680, https://doi.org/10.1175/JCLI-D-18-0563.1.

Back, L. E., and C. S. Bretherton, 2005: The relationship between wind speed and precipitation in the pacific itcz. *Journal of Climate*, **18 (20)**, 4317–4328, https://doi.org/10.1175/JCLI3519.1.

Backstrom, B. R., 1984: The Earth Radiation Budget Experiment (ERBE). *Bulletin of the American Meteorological Society*, **65 (11)**, 1170–1185, https://doi.org/10.1175/1520-0477(1984)065⟨1170:TERBE⟩2.0.CO;2.

Barnett, T. P., 1991: The interaction of multiple time scales in the tropical climate system. *Journal of Climate*, **4 (3)**, 269–285, https://doi.org/10.1175/1520-0442(1991)004⟨0269:TIOMTS⟩2.0.CO;2.

Beaudoing, H., and M. Rodell, 2020: GLDAS noah land surface model L4 3 hourly 0.25 x 0.25 degree V2.1. Tech. rep., Goddard Earth Sciences Data and Information Services Center (GES DISC), Greenbelt, Maryland, USA. https://doi.org/10.5067/E7TYRXPJKWOQ.

Bentamy, A., S. A. Grodsky, K. Katsaros, A. M. Mestas-Nuñez, B. Blanke, and F. Desbiolles, 2013: Improvement in air–sea flux estimates derived from satellite observations. *International Journal of Remote Sensing*, **34 (14)**, 5243–5261, https://doi.org/10.1080/01431161.2013.787502.

Bjerknes, J., 1964: Atlantic air-sea interaction. *Advances in Geophysics*, **10**, 1–82, https://doi.org/10.1016/S0065-2687(08)60005-9.

Bjerknes, V., 1914: Meteorology and an exact science. *Monthly Weather Review*, **42 (1)**, 11–14, https://doi.org/10.1175/1520-0493(1914)42⟨11:MAAES⟩2.0.CO;2.

Blanchard-Wrigglesworth, E., C. M. Bitz, and M. M. Holland, 2011: Influence of initial conditions and climate forcing on predicting Arctic sea ice. *Geophysical Research Letters*, **38 (18)**, L18503, https://doi.org/10.1029/2011GL048807.

Blanchard-Wrigglesworth, E., T. Cox, Z. I. Espinose, and A. Donohoe, 2023: The largest ever recorded heatwave—characteristics and attribution of the antarctic heatwave of march 2022. *Geophysical Research Letters*, **50 (5)**, e2023GL104 910, https://doi.org/10.1029/2023GL104910.

Boeke, R. C., and P. C. Taylor, 2018: Seasonal energy exchange in sea ice retreat regions contributes to differences in projected Arctic warming. *Nature Communications*, **9**, 5017, https://doi.org/10.1038/s41467-018-07061-9.

Bollmeyer, C., and A. Hense, 2014: Inverse modeling of energy transports and budgets of the atmosphere. *Climate Dynamics*, **43**, 829–844, https://doi.org/10.1007/s00382-014-2090-z.

Budyko, M. I., 1969: The effect of solar radiation variations on the climate of the earth. *Tellus*, **21**, 611–619.

Chepfer, H., V. Noel, M. Chiriaco, B. Wielicki, D. Winker, N. Loeb, and R. Wood, 2018: The potential of a multidecade spaceborne lidar record to constrain cloud feedback. *Journal of Geophysical Research: Atmospheres*, **123 (10)**, 5433–5454, https://doi.org/10.1002/2017jd027742.

Cleveland, R. B., W. S. Cleveland, J. E. McRae, and I. Terpenning, 1990: STL: A Seasonal-Trend Decomposition Procedure Based on Loess. *Journal of Official Statistics*, **6**, 3–33.

Cox, T., A. Donohoe, K. C. Armour, D. M. W. Frierson, and G. H. Roe, 2024a: Trends in atmospheric heat transport since 1980. *Journal of Climate*, **37 (5)**, 1539–1550, https://doi.org/10.1175/JCLI-D-23-0385.1.

Cox, T., A. Donohoe, K. C. Armour, G. H. Roe, and D. M. W. Frierson, 2024b: A new method for calculating instantaneous atmospheric heat transport. *Journal of Climate*, **37 (17)**, 4337–4346, https://doi.org/10.1175/JCLI-D-23-0521.1.

Cox, T., A. Donohoe, G. H. Roe, K. C. Armour, and D. M. W. Frierson, 2022: Near invariance of poleward atmospheric heat transport in response to midlatitude orography. *Journal of Climate*, **35 (13)**, 4099–4113, https://doi.org/10.1175/JCLI-D-21-0888.1.

Curry, J. A., and Coauthors, 2004: SEAFLUX. *BAMS*, **83 (3)**, https://doi.org/10.1175/BAMS-85-3-409.

Donohoe, A., K. C. Armour, G. H. Roe, D. S. Battisti, and L. Hahn, 2020: The partitioning of meridional heat transport from the last glacial maximum to CO_2 quadrupling in coupled climate models. *Journal of Climate*, **33**, 4141–4165, https://doi.org/10.1175/JCLI-D-19-0797.1.

Donohoe, A., J. Marshall, D. Ferreira, K. Armour, and D. McGee, 2014: The interannual variability of tropical precipitation and interhemispheric energy transport. *Journal of Climate*, **27**, 3377–3392, https://doi.org/10.1175/JCLI-D-13-00499.1.

Donohoe, A., J. Marshall, D. Ferreira, and D. McGee, 2013: The relationship between itcz location and atmospheric heat transport across the equator: From the seasonal cycle to the last glacial maximum. *Journal of Climate*, **26**, 3597–3618, https://doi.org/10.1175/JCLI-D-12-00467.1.

Duncan, B. N., and Coauthors, 2020: Space-based observations for understanding changes in the Arctic-Boreal Zone. *Reviews of Geophysics*, **58 (1)**, e2019RG000652, https://doi.org/10.1029/2019RG000652.

Eayrs, C., X. Li, M. N. Raphael, and D. M. Holland, 2021: Rapid decline in Antarctic sea ice in recent years hints at future change. *Nature Geoscience*, **14**, 460–464, https://doi.org/10.1038/s41561-021-00768-3.

Edson, J. B., and Coauthors, 2013: On the exchange of momentum over the open ocean. *Journal of Physical Oceanography*, **43 (8)**, 1589–1610, https://doi.org/10.1175/JPO-D-12-0173.1.

Eyring, V., and Coauthors, 2021: Reflections and projections on a decade of climate science. *Nature Climate Change*, **11**, 279–285, https://doi.org/10.1038/s41558-021-01020-x.

Fairall, C. W., E. F. Bradley, J. S. Godfrey, G. A. Wick, J. B. Edson, and G. S. Young, 1996: Bulk parameterization of air-sea fluxes for tropical ocean-global atmosphere coupled-ocean atmosphere response experiment. *Journal of Geophysical Research*, **101 (C2)**, 3747–3764, https://doi.org/10.1029/95JC03205.

Fairall, C. W., E. F. Bradley, J. E. Hare, A. A. Grachev, and J. B. Edson, 2003: Bulk parameterization of air–sea fluxes: Updates and verification for the coare algorithm. *Journal of Climate*, **16 (4)**, 571–591, https://doi.org/10.1175/1520-0442(2003)016⟨0571:BPOASF⟩2.0.CO;2.

Fajber, R., A. Donohoe, S. Ragen, K. C. Armour, and P. J. Kushner, 2023: Atmospheric heat transport is governed by meridional gradients in surface evaporation in modern-day earth-like climates. *Proceedings of the National Academy of Sciences of the United States of America*, **120 (25)**, e2217202 120, https://doi.org/10.1073/pnas.2217202120.

Fasullo, J. T., and K. E. Trenberth, 2008: The annual cycle of the energy budget: Part 2. Meridional structures and poleward transports. *Journal of Climate*, **21**, 2313–2325, https://doi.org/10.1175/2007JCLI1936.1.

Frierson, D. M. W., and Y. T. Hwang, 2012: Extratropicalinfluence on ITCZ shifts in slab ocean simulations of global warming. *Journal of Climate*, **25**, 720–733, https://doi.org/10.1175/JCLI-D-11-00116.1.

Gelaro, R., and Coauthors, 2017: The Modern-Era Retrospective Analysis for Research and Applications, Version 2 (MERRA-2). *Journal of Climate*, **30 (14)**, 5419–5454, https://doi.org/10.1175/JCLI-D-16-0758.1.

Goosse, H., and Coauthors, 2018: Quantifying climate feedbacks in polar regions. *Nature Communications*, **9 (14)**, 1919, https://doi.org/10.1038/s41467-018-04173-0.

Goyal, R., M. Jucker, A. S. Gupta, and M. H. England, 2022: A New Zonal Wave-3 Index for the Southern Hemisphere. *Journal of Climate*, **35 (15)**, 5137–5149, https://doi.org/10.1175/JCLI-D-21-0927.1.

Guemas, V., and Coauthors, 2016: A review on Arctic sea-ice predictability and prediction on seasonal to decadal time-scales. *Quarterly Journal of the Royal Meteorological Society*, **142**, 546–561, https://doi.org/10.1002/qj.2401.

Gupta, K., A. Mukhopadhyay, D. G. Babb, D. G. Barber, and J. K. Ehn, 2022: Landfast sea ice in Hudson Bay and James Bay: Annual cycle, variability and trends, 2000-2019. *Elementa: Science of the Antropocene*, **10 (1)**, 00073, https://doi.org/10.1525/elementa.2021.00073.

Hahn, L. C., K. C. Armour, M. D. Zelinka, C. M. Bitz, and A. Donohoe, 2021: Contributions to polar amplification in CMIP5 and CMIP6 models. *Frontiers in Earth Science*, **9**, 710036, https://doi.org/10.3389/feart.2021.710036.

Handcock, M. S., and M. N. Raphael, 2020: Modeling the annual cycle of daily Antarctic sea ice extent. *The Crysophere*, **14**, 2159–2171, https://doi.org/10.5194/tc-14-2159-2020.

Held, I., and B. Soden, 2006: Robust responses of the hydrological cycle to global warming. *Journal of Climate*, **19 (21)**, 5686–5699, https://doi.org/10.1175/JCLI3990.1.

Hersbach, H., and Coauthors, 2018: Operational global reanalysis: progress, future directions and synergies with NWP. *ERA Rep. 27*, 63, https://doi.org/10.21957/tkic6g3wm.

Hoskins, B. J., and K. I. Hodges, 2019: The Annual Cycle of Northern Hemisphere Storm Tracks. Part I: Seasons. *Journal of Climate*, **32 (6)**, 1743–1760, https://doi.org/10.1175/JCLI-D-17-0870.1.

Huguenin, M. F., R. M. Holmes, and M. H. England, 2022: Drivers and distribution of global ocean heat uptake over the last half century. *Nature Communications*, **13**, 4921, https://doi.org/10.1038/s41467-022-32540-5.

Hwang, Y., D. Frierson, , and J. Kay, 2011: Coupling between arctic feedbacks and changes in poleward energy transport. *Geophysical Research Letters*, **38**, L17 704, https://doi.org/10.1029/2011GL048546.

IARPC, 2021: Arctic Research Plan 2022-2026. Tech. rep., Interagency Arctic Research Policy Committee of the National Science and Technology Council, Washington, D.C.

Johnson, D. S., 1962: Meteorological measurements from satellites. *Bulletin of the American Meteorological Society*, **43 (9)**, 481–484.

Johnson, G. C., F. W. Fanderer, N. G. Loeb, J. M. Lyman, M. Mayer, A. L. S. Swann, and J. Zhang, 2023: Closure of Earth's global seasonal cycle of energy storage. *Surveys in Geophysics*, https://doi.org/10.1007/s10712-023-09797-6.

Kang, S. M., D. M. W. Frierson, and I. M. Held, 2009: The Tropical Response to Extratropical Thermal Forcing in an Idealized GCM: The Importance of Radiative Feedbacks and Convective Parameterization. *Journal of Atmospheric Sciences*, **66 (9)**, 2812–2827, https://doi.org/10.1175/2009JAS2924.1.

Kang, S. M., I. M. Held, D. M. W. Frierson, and M. Zhao, 2008: The Response of the ITCZ to Extratropical Thermal Forcing: Idealized Slab-Ocean Experiments with a GCM. *Journal of Climate*, **21 (14)**, 3521–3532, https://doi.org/10.1175/2007JCLI2146.1.

Kato, S., and Coauthors, 2018: Surface irradiances of edition 4.0 clouds and the earth's radiant energy system (CERES) energy balanced and filled (EBAF) data product. *Journal of Climate*, **31 (11)**, 4501–4527, https://doi.org/10.1175/JCLI-D-17-0523.1.

Kay, J. E., and A. Gettelman, 2009: Cloud influence on and response to seasonal Arctic sea ice loss. *Journal of Geophysical Research Atmospheres*, **144 (D18)**, https://doi.org/10.1029/2009JD011773.

Kobayashi, S., and Coauthors, 2015: The JRA-55 Reanalysis: General specifications and basic characteristics. *Journal of the Meteorological Society of Japan*, **93**, 5–48, https://doi.org/10.2151/jmsj.2015-001.

Landy, J. C., and Coauthors, 2022: A year-round satellite sea-ice record from CryosSat-2. *Nature*, **609**, 517–522, https://doi.org/10.1038/s41586-022-05058-5.

Lenssen, N. J. L., G. A. Schmidt, J. E. Hansen, M. J. Menne, A. Persin, R. Ruedy, and D. Zyss, 2019: Improvements in the GISTEMP uncertainty model. *Journal of Geophysical Research Atmospheres*, **124 (12)**, 6307–6326, https://doi.org/10.1029/2018JD029522.

Liu, C., and R. Allan, 2022: Reconstructions of the radiation fluxes at the top of atmosphere and net surface energy flux: DEEP-C Version 5.0. Tech. rep., University of Reading - Dataset. https://doi.org/10.17864/1947.000347.

Liu, C., and Coauthors, 2015: Combining satellite observations and reanalysis energy transport to estimate global net surface energy fluxes. *Journal of Gephysical Research: Atmospheres*, **120**, 9374–9389, https://doi.org/10.1002/2015JD023264.

Liu, C., and Coauthors, 2017: Evaluation of satellite and reanalysis based global net surface energy flux and uncertainty estimates. *J. Geophys. Res. Atmos.*, **122**, 6250–6272, https://doi.org/10.1002/2017JD026616.

Liu, C., and Coauthors, 2020: Variability in the global energy budget and transports 1985–2017. *Climate Dynamics*, **55**, 3381–3396, https://doi.org/10.1007/s00382-020-05451-8.

Loeb, N. G., G. C. Johnson, T. J. Thornsen, J. M. Lyman, F. G. Rose, and S. Kato, 2021: Satellite and ocean data reveal marked increase in Earth's heating rate. *Geophysical Research Letters*, **48**, e2021GL093047, https://doi.org/10.1029/2021GL093047.

Loeb, N. G., B. A. Wielicki, D. R. Doelling, G. L. Smith, D. F. Keyes, S. Kato, N. Manalo-Smith, and T. Wong, 2009: Toward optimal closure of the Earth's top-of-atmosphere radiation budget. *Journal of Climate*, **22 (3)**, 748–766, https://doi.org/10.1175/2008JCLI2637.1.

Loeb, N. G., and Coauthors, 2018: Clouds and the Earth's Radiant Energy System (CERES) Energy Balanced and Filled (EBAF) Top-of-Atmosphere (TOA) Edition-4.0 Data Product. *Journal of Climate*, **31 (2)**, https://doi.org/10.1175/JCLI-D-17-0208.1.

Loeb, N. G., and Coauthors, 2022: Evaluating twenty-year trends in Earth's energy flows from observations and reanalyses. *Journal of Geophysical Research: Atmospheres*, **127**, e2022JD036686, https://doi.org/10.1029/2022JD036686.

Lorenz, D. J., and D. L. Hartmann, 2003: Eddy–zonal flow feedback in the northern hemisphere winter. *Journal of Climate*, **16 (8)**, 1212–1227, https://doi.org/10.1175/1520-0442(2003)16⟨1212:EFFITN⟩2.0.CO;2.

Lorenz, E. N., 1955: Available potential energy and the maintenance of the general circulation. *Tellus*, **7**, 157–167, https://doi.org/10.3402/tellusa.v7i2.8796.

L'Ecuyer, T. S., Y. Hang, A. V. Watus, and Z. Wang, 2019: Reassessing the effect of cloud type on earth's energy balance in the age of active spaceborne observations. part i: Top of atmosphere and surface. *Journal of Climate*, **32 (19)**, 6197–6217, https://doi.org/10.1175/JCLI-D-18-0753.1.

L'Ecuyer, T. S., and Coauthors, 2015: The observed state of the energy budget in the early twenty-first century. *Journal of Climate*, **28 (21)**, 8319–8346, https://doi.org/10.1175/JCLI-D-14-00556.1.

L'Ecuyer, T. S., and Coauthors, 2021: The polar radiant energy in the far infrared experiment. *Bulletin of the American Meteorological Society*, **102 (7)**, 1431–1449, https://doi.org/10.1175/BAMS-D-20-0155.1.

Markus, T., J. C. Stroeve, and J. Miller, 2009: Recent changes in Arctic sea ice melt onset, freezeup, and melt season length. *Journals of Geophysical Research Oceans*, **114**, C12024, https://doi.org/10.1029/2009JC005436.

Maslanik, J., J. Stroeve, C. Fowler, and W. Emery, 2011: Distribution and trends in Arctic sea ice age through spring 2011. *Geophysical Research Letters*, **38 (13)**, L13502, https://doi.org/10.1029/2011GL047735.

Mayer, J., M. Mayer, and L. Haimberger, 2021: Consistency and homogeneity of atmospheric energy, moisture, and mass budgets in era5. *Journal of Climate*, **34 (10)**, 3955–3974, https://doi.org/10.1175/JCLI-D-20-0676.1.

Mayer, J., M. Mayer, and L. Haimberger, 2022a: Mass-consistent atmospheric energy and moisture budget data from 1979 to present derived from era5 reanalysis, v1.0. Copernicus Climate Change Service (C3S) Climate Data Store (CDS). (Accessed on 31-05-2022), https://doi.org/10.24381/cds.c2451f6b.

Mayer, J., M. Mayer, L. Haimberger, and C. Liu, 2022b: Comparison of surface energy fluxes from global to local scale. *Journal of Climate*, **35 (14)**, 4551–4569, https://doi.org/10.1175/JCLI-D-21-0598.1.

Mayer, M., L. Haimberger, J. M. Edwards, and P. Hyder, 2017: Toward consistent diagnostics of the coupled atmosphere and ocean energy budgets. *Journal of Climate*, **30 (22)**, 9225–9246, https://doi.org/10.1175/JCLI-D-17-0137.1.

Mayer, M., S. Tietsche, L. Haimberger, T. Tsubouchi, J. Mayer, and H. Zou, 2019: An improved estimate of the coupled Arctic energy balance. *Journal of Climate*, **32 (22)**, 7915–7934, https://doi.org/10.1175/JCLI-D-19-0233.1.

Mayer, M., and Coauthors, 2024: Assessment of atmospheric and surface energy budgets using observation-based data products. *Surverys in Geophysics*, https://doi.org/10.1007/s10712-024-09827-x.

Meier, W. N., F. Fetterer, A. K. Windnagel, and S. Stewart, 2021: NOAA/NSIDC Climate Data Record of Passive Microwave Sea Ice Concentration, Version 4. Boulder, Colorado USA. NSIDC: National Snow and Ice Data Center, https://doi.org/10.7265/efmz-2t65.

Meredith, M., and Coauthors, 2019: Polar Regions. *IPCC Special Report on the Ocean and Cryosphere in a Changing Climate*, H.-O. Pörtner, D. Roberts, V. Masson-Delmotte, P. Zhai, M. Tignor, E. Poloczanska, K. Mintenbeck, A. Alegría, M. Nicolai, A. Okem, J. Petzold, B. Rama, and N. Weyer, Eds., Cambridge University Press, Cambridge, UK and New York, NY, USA, 203–320, https://doi.org/10.1017/9781009157964.005.

Merlis, T. M., N. Feldl, and R. Caballero, 2022: Changes in poleward atmospheric energy transport over a wide range of climates: Energetic and diffusive perspectives and A Priori theories. *Journal of Climate*, **35 (20)**, 6533–6548, https://doi.org/10.1175/JCLI-D-21-0682.1.

Merlis, T. M., and M. Henry, 2018: Simple estimates of polar amplification in moist diffusive energy balance models. *Journal of Climate*, **31**, 5811–5824, https://doi.org/10.1175/JCLI-D-17-0578.1.

Messori, G., and A. Czaja, 2011: On the sporadic nature of meridional heat transport by transient eddies. *Quarterly Journal of the Royal Meteorological Society*, **137**, 1027–1037, https://doi.org/10.1002/qj.2011.

Messori, G., and A. Czaja, 2014: Some considerations on the spectral features of meridional heat transport by transient eddies. *Quarterly Journal of the Royal Meteorological Society*, **140 (681)**, 1377–1386, https://doi.org/10.1002/qj.2224.

Messori, G., and A. Czaja, 2015: On local and zonal pulses of atmospheric heat transport in reanalysis data. *Quarterly Journal of the Royal Meteorological Society*, **141 (691)**, 2376–2389, https://doi.org/10.1002/qj.2529.

Morrison, A. K., S. M. Griffies, M. Winton, W. G. Anderson, and J. L. Sarmiento, 2016: Mechanisms of Southern Ocean heat uptake and transport in a global eddying climate model. *Journal of Climate*, **29 (6)**, 2059–2075, https://doi.org/10.1175/JCLI-D-15-0579.1.

Myers-Smith, I. H., and Coauthors, 2020: Complexity revealed in the greening Arctic. *Nature Climate Change*, **10**, 106–117, https://doi.org/10.1038/s41558-019-0688-1.

Nakamura, H., and A. Shimpo, 2004: Seasonal Variations in the Southern Hemisphere Storm Tracks and Jet Streams as Revealed in a Reanalysis Dataset. *Journal of Climate*, **17 (9)**, 1828–1844, https://doi.org/10.1175/1520-0442(2004)017⟨1828:SVITSH⟩2.0.CO;2.

Nicolas, J. P., and D. H. Bromwich, 2014: New reconstruction of Antarctic near-surface temperatures: Multidecadal trends and reliability of global reanalyses. *Journal of Climate*, **27 (21)**, 8070–8093, https://doi.org/10.1175/JCLI-D-13-00733.1.

North, G. R., R. F. Cahalan, and J. A. Coakley, 1981: Energy balance climate models. *Reviews of Geophysics*, **19 (1)**, 91–121, https://doi.org/10.1029/RG019i001p00091.

NSIDC, 2023: Antarctic sea ice settles at record low in 2023. National Snow and Ice Data Center. 27 February 2023, https://nsidc.org/news-analyses/news-stories/antarctic-sea-ice-settles-record-low-2023.

Oort, A., 1971: The observed annual cycle in the meridional transport of atmospheric energy. *Journal of Atmospheric Science*, **28**, 325–339, https://doi.org/10.1175/1520-0469(1971)028,0325:TOACIT.2.0.CO;2.

Oort, A., and T. Vonder Haar, 1976: On the observed annual cycle in the ocean–atmosphere heat balance over the Northern Hemisphere. *Journal of Physical Oceanography*, **6**, 781–800, https://doi.org/10.1175/1520-0485(1976)006,0781:OTOACI.2.0.CO;2.

Pan, Y., and Coauthors, 2023: Annual cycle in upper-ocean heat content and the global energy budget. *Journal of Climate*, **36 (15)**, 5003–5026, https://doi.org/10.1175/JCLI-D-22-0776.1.

Parkinson, C. L., 2019: A 40-y record reveals gradual Antarctic sea ice increases followed by decreases at rates far exceeding the rates seen in the Arctic. *Proceedings of the National Academy of Sciences*, **116 (29)**, 14 414–14 423, https://doi.org/10.1073/pnas.1906556116.

Pastorello, G., and Coauthors, 2020: The FLUXNET2015 dataset and the ONEFlux processing pipeline for eddy covariance data,. *Scientific Data*, **7 (255)**, https://doi.org/10.1038/s41597-020-0534-3.

Peterson, C. A., X. Chen, Q. Yue, and X. Huang, 2019: The spectral dimension of Arctic outgoing longwave radiation and greenhouse efficiency trends from 2003 to 2016. *Journal of Geophysical Research: Atmospheres*, **124**, 8467–8480, https://doi.org/10.1029/2019JD030428.

Pilewskie, P., and M. Z. Hakuba, 2020: Libera and the Continuity of the ERB climate data record, Houston, TX, USA. American Geophysical Union, aGU Fall Meeting: 2020AGUFMGC133..01P.

Pistone, K., I. Eisenman, and V. Ramanathan, 2014: Observational determination of albedo decrease caused by vanishing Arctic sea ice. *Proceedings of the National Academy of Sciences*, **111 (9)**, 3322–3326, https://doi.org/10.1073/pnas.1318201111.

Prince, H. D., A. Donohoe, and T. S. L'Ecuyer, 2025: Constraining atmospheric heat transport from earth energy budget observations. *Journal of Climate*, under review.

Raghuraman, S. P., D. Paynter, and V. Ramaswamy, 2021: Anthropogenic forcing and response yield observed positive trend in Earth's energy imbalance. *Nature Communications*, **12**, 4577, https://doi.org/10.1038/s41467-021-24544-4.

Raphael, M. N., 2004: A zonal wave 3 index for the Southern Hemisphere. *Geophysical Research Letters*, **31 (23)**, https://doi.org/10.1029/2004GL020365.

Raschke, E., and W. R. Bandeen, 1970: The Radiation Balance of the Planet Earth from Radiation Measurements of the Satellite Nimbus II. *Journal of Applied Meteorology and Climatology*, **9 (2)**, 215–238, https://doi.org/10.1175/1520-0450(1970)009⟨0215:TRBOTP⟩2.0.CO;2.

Riehl, H., and J. S. Malkus, 1958: On the heat balance in the equatorial trough zone. *Geophysica*, **6**, 503–538.

Rienecker, M., and Coauthors, 2011: MERRA: NASA's Modern-Era Retrospective Analysis for Research and Applications. *Journal of Climate*, **24 (14)**, https://doi.org/10.1175/JCLI-D-11-00015.1.

Riihelä, A., T. Manninen, and V. Laine, 2013: Observed changes in the albedo of the Arctic sea-ice zone for the period 1982-2009. *Nature Climate Change*, **3**, 895–898, https://doi.org/10.1038/nclimate1963.

Roberts, J. C., C. A. Clayson, and F. R. Robertson, 2020: SeaFlux Data Products. Tech. rep., NASA Global Hydrology Resource Center DAAC, Huntsville, Alabama, U.S.A. https://doi.org/10.5067/SEAFLUX/DATA101.

Robertson, F. R., and Coauthors, 2020: Uncertainties in ocean latent heat flux variations over recent decades in satellite-based estimates and reduced observation reanalyses. *Journal of Climate*, **33 (19)**, 8415–8437, https://doi.org/10.1175/JCLI-D-19-0954.1.

Rodell, M., and Coauthors, 2004: The Global Land Data Assimilation System. *BAMS*, **85 (3)**, 381–394, https://doi.org/10.1175/BAMS-85-3-381.

Rodell, M., and Coauthors, 2015: The observed state of the water cycle in the early Twenty-First Century. *Journal of Climate*, **28 (21)**, 8289–8318, https://doi.org/10.1175/JCLI-D-14-00555.1.

Salzmann, M., 2017: The polar amplification asymmetry: role of Antarctic surface height. *Earth System Dynamics*, **8**, 323–336, https://doi.org/10.5194/esd-8-323-2017.

Screen, J. A., and I. Simmonds, 2010: Increasing fall-winter energy loss from the Arctic ocean and its role in Arctic temperature amplification. *Geophysical Research Letters*, **37**, L16707, https://doi.org/10.1029/2010GL044136.

Seo, J., S. M. Kang, and D. M. W. Frierson, 2014: Sensitivity of intertropical convergence zone movement to the latitudinal position of thermal forcing. *Journal of Climate*, **27 (8)**, https://doi.org/10.1175/JCLI-D-13-00691.1.

Seo, M., H.-C. Kim, M. Huh, J.-M. Yeom, and C. S. Lee, 2016: Long-term variability of surface albedo and its correlation with climatic variables over Antarctica. *Remote Sensing*, **8**, 981, https://doi.org/10.3390/rs8120981.

Serreze, M. C., and R. G. Barry, 2011: Processes and impacts of Arctic amplification: A research synthesis. *Global and Planetary Change*, **77**, 85–96, https://doi.org/10.1016/j.gloplacha.2011.03.004.

Sévellec, F., A. V. Fedorov, and W. Liu, 2017: Arctic sea-ice decline weakens the Atlantic Meridional Overturning Circulation. *Nature Climate Change*, **7**, 604–610, https://doi.org/10.1038/nclimate3353.

Shaffrey, L., and R. Sutton, 2006: Bjerknes compensation and the decadal variability of the energy transports in a coupled climate model. *Journal of Climate*, **19 (7)**, 1167–1181, https://doi.org/10.1175/JCLI3652.1.

Shaw, T. A., P. Barpanda, and A. Donohoe, 2018: A moist static energy framework for zonal-mean storm-track intensity. *Journal of the Atmospheric Sciences*, **75 (6)**, 1979–1994, https://doi.org/10.1175/JAS-D-17-0183.1.

Sledd, A., and T. S. L'Ecuyer, 2019: How much do clouds mask the impacts of Arctic sea ice and snow cover variations? Different perspectives from observations and reanalyses. *Atmosphere*, **10 (1)**, 12, https://doi.org/10.3390/atmos10010012.

Sledd, A., and T. S. L'Ecuyer, 2021: Emerging trends in Arctic solar absorption. *Geophysical Research Letters*, **48**, e2021GL095813, https://doi.org/10.1029/2021GL095813.

Sledd, A., T. S. L'Ecuyer, J. E. Kay, and M. Steele, 2023: Clouds increasingly influence Arctic sea surface temperatures as CO_2 rises. *Geophysical Research Letters*, **50**, e2023GL102850, https://doi.org/10.1029/2023GL102850.

Smith, D. M., and Coauthors, 2019: The Polar Amplification Model Intercomparison Project (PAMIP) Contribution to CMIP6: Investigating the Causes and Consequences of Polar Amplification. *Geoscience Model Development*, **12**, 1139–1164, https://doi.org/10.5194/gmd-12-1139-2019.

Smith, L. C., and S. R. Stephenson, 2012: New trans-Arctic shipping routes navigable by midcentury. *Proceedings of the National Academy of Sciences*, **110 (13)**, E1191–E1195, https://doi.org/10.1073/pnas.1214212110.

Soumi, V. E., 1961: Earth's thermal radiation balance - Preliminary results from Explorer VII. *Transactions of the American Geophysical Union*, **42**, 467–474.

Steele, M., and S. Dickinson, 2016: The phenology of Arctic Ocean surface warming. *Journal of Geophysical Research: Oceans*, **121 (11)**, 6847–6861, https://doi.org/10.1002/2016JC012089.

Steele, M., J. Zhang, and W. Ermold, 2010: Mechanisms of summertime upper Arctic Ocean warming and the effect of sea ice melt. *Journal of Geophysical Research: Oceans*, **115**, C11004, https://doi.org/10.1029/2009JC005849.

Stephen, K., 2018: Societal impacts of a rapidly changing Arctic. *Current Climate Change Reports*, **4**, 223–237, https://doi.org/10.1007/s40641-018-0106-1.

Stephens, G. L., A. S. Kathleen, M. Z. Hakuba, H. Takahashi, J. A. Pilewskie, T. Andrews, C. J. Stubenrauch, and L. Wu, 2024: Tropical deep convection, cloud feedbacks and climate sensitivity. *Surveys of Geophysics*, **45**, 1903–1931, https://doi.org/10.1007/s10712-024-09831-1.

Stephens, G. L., and Coauthors, 2022: The changing nature of Earth's reflected sunlight. *Proceedings of the Royal Society*, **478 (2263)**, https://doi.org/10.1098/rspa.2022.0053.

Stone, P. H., 1978: Constraints on dynamical transports of energy on a spherical planet. *Dynamic of Atmospheres and Oceans*, **2 (2)**, 123–139, https://doi.org/10.1016/0377-0265(78)90006-4.

Stroeve, J. C., and D. Notz, 2018: Changing state of Arctic sea ice across all seasons. *Environmental Research Letters*, **13 (10)**, 103001, https://doi.org/10.1088/1748-9326/aade56.

Stroeve, J. C., M. C. Serreze, M. M. Holland, J. E. Kay, J. Malanik, and A. P. Barrett, 2012: The Arctic's rapidly shrinking sea ice cover: A research synthesis. *Climate Change*, **110**, 1005–1027, https://doi.org/10.1007/s10584-011-0101-1.

Stuecker, M. F., and Coauthors, 2018: Polar amplification dominated by local forcing and feedbacks. *Nature Climate Change*, **8**, 1076–1081, https://doi.org/10.1038/s41558-018-0339-y.

Tang, R., Y. Wang, Y. Jiang, M. Liu, Y. Hu, L. Huang, and Z. L. Li, 2024: A review of global products of air-sea turbulent heat flux: accuracy, mean, variability, and trend. *Earth-Science Reviews*, **249**, 104 662, https://doi.org/10.1016/j.earscirev.2023.104662.

Taylor, P. C., S. Kato, K.-M. Xu, and M. Cai, 2015: Covariance between Arctic sea ice and clouds within atmospheric state regimes at the satellite footprint level. *Journal of Geophysical Research Atmospheres*, **120**, https://doi.org/10.1002/2015JD023520.

Taylor, P. C., and Coauthors, 2022: Process drivers, inter-model spread, and the path forward: A review of amplified Arctic warming. *Frontiers in Earth Science*, **9**, 758361, https://doi.org/10.3389/feart.2021.758361.

Thompson, D. W. J., S. Solomon, P. J. Kushner, M. H. England, K. M. Grise, and D. J. Karoly, 2011: Signatures of the Antarctic ozone hole in Southern Hemisphere surface climate change. *Nature Geoscience*, **4**, 741–749, https://doi.org/10.1038/ngeo1296.

Timmermans, M.-L., and J. Marshall, 2020: Understanding Arctic ocean circulation: A review of ocean dynamics in a changing climate. *Journal of Geophysical Research: Oceans*, **125**, e2018JC014378, https://doi.org/10.1029/2018JC014378.

Tomita, H., T. Hihara, S. Kako, M. Kubota, and K. Kutsuwada, 2019: An introduction to J-OFURO3, a third-generation Japanese ocean flux data set using remote-sensing observations. *Journal of Oceanography*, **75**, 171–194, https://doi.org/10.1007/s10872-018-0493-x.

Trenberth, K. E., 1997: Using atmospheric budgets as a constraint on surface fluxes. *Journal of Climate*, **10**, 2796–2809, https://doi.org/10.1175/1520-0442(1997)010,2796:UABAAC.2.0.CO;2.

Trenberth, K. E., J. M. Caron, and D. P. Stepaniak, 2001: The atmospheric energy budget and implications for surface fluxes and ocean heat transports. *Climate Dynamics*, **17**, 259–276, https://doi.org/https://doi.org/10.1007/PL00007927.

Trenberth, K. E., and J. T. Fasullo, 2012: Tracking Earth's energy: from El Niño to global warming. *Survey of Geophysics*, **33**, 413–426, https://doi.org/10.1007/s10712-011-9150-2.

Trenberth, K. E., and J. T. Fasullo, 2018: Applications of an updated atmospheric energetics formulation. *Journal of Climate*, **31 (16)**, 6263–6279, https://doi.org/10.1175/JCLI-D-17-0838.1.

Trenberth, K. E., J. T. Fasullo, K. von Schuckmann, and L. Cheng, 2016: Insights into earth's energy imbalance from multiple sources. *Journal of Climate*, **29 (20)**, 7495–7505, https://doi.org/10.1175/JCLI-D-16-0339.1.

Trenberth, K. E., and A. Solomon, 1994: The global heat balance: heat transports in the atmosphere and ocean. *Climate Dynamics*, **10**, 107–134, https://doi.org/10.1007/BF00210625.

Trenberth, K. E., and D. P. Stepaniak, 2003: Seamless poleward atmospheric energy transports and implications for the hadley circulation. *Journal of Climate*, **16 (22)**, 3706–3722, https://doi.org/10.1175/1520-0442(2003)016⟨3706:SPAETA⟩2.0.CO;2.

Trenberth, K. E., Y. Zhang, J. T. Fasullo, and L. Cheng, 2019: Observation-based estimates of global and basin ocean meridional heat transport time series. *Journal of Climate*, **32 (14)**, 4567–4583, https://doi.org/10.1175/JCLI-D-18-0872.1.

Trenberth, K. F., and K. C. Mo, 1985: Blocking in the southern hemisphere. *Monthly Weather Review*, **113 (1)**, 3–21, https://doi.org/10.1175/1520-0493(1985)113⟨0003:BITSH⟩2.0.CO;2.

von Schuckmann, K., and Coauthors, 2023: Heat stored in the Earth system 1960–2020: where does the energy go? *Earth System Science Data*, **15 (3)**, 1675–1695, https://doi.org/10.5194/essd-15-1675-2023.

Weatherhead, E. C., and Coauthors, 1998: Factors affecting the detection of trends: Statistical considerations and applications to environmental data. *Journal of Geophysical Research*, **103 (D14)**, 17 149–17 161, https://doi.org/10.1029/98jd00995.

Woods, C., and R. Caballero, 2016: The role of moist intrusions in winter arctic warming and sea ice decline. *Journal of Climate*, **29 (12)**, 4473–4485, https://doi.org/10.1175/JCLI-D-15-0773.1.

Wu, F., W. Li, P. Zhang, and W. Li, 2020: Relative contributions of internal atmospheric variability and surface processes to the interannual variations in wintertime Arctic surface air temperatures. *Journal of Climate*, **34 (17)**, 7131–7148, https://doi.org/10.1175/JCLI-D-20-0779.1.

Yu, L., 2019: Global air-sea fluxes of heat, fresh water, and momentum: Energy budget closure and unanswered questions. *Annual Review of Marine Science*, **11**, 227–248, https://doi.org/10.1146/annurev-marine-010816-060704.

Yu, L., X. Jin, and R. A. Weller, 2008: Multidecade global flux datasets from the objectively analyzed air-sea fluxes (OAFlux) project: Latent and sensible heat fluxes, ocean evaporation, and related surface meteorological variables. Tech. rep., Woods Hole Oceanographic Institution, OAFlux Project Technical Report.

Zuo, H., M. A. Balmaseda, S. Tietsche, K. Mogensen, and M. Mayer, 2019: The ECMWF operational ensemble reanalysis-analysis system for ocean and sea-ice: A description of the system and assessment. *Ocean Science*, **14**, 779–808, https://doi.org/10.5194/os-15-779-2019.